UNIVERSITY OF TURKU

ELECTROENCAPSULATION AND ELECTROSPRAYING OF PHARMACEUTICAL MATERIALS IN PREPARATION FOR ORAL DRUG DELIVERY APPLICATIONS

Jorma Roine

TURUN YLIOPISTON JULKAISUJA – ANNALES UNIVERSITATIS TURKUENSIS
SARJA - SER. AI OSA - TOM. 599 | ASTRONOMICA - CHEMICA - PHYSICA - MATHEMATICA | TURKU 2019

UNIVERSITY OF TURKU

ELECTROENCAPSULATION AND ELECTROSPRAYING OF PHARMACEUTICAL MATERIALS IN PREPARATION FOR ORAL DRUG DELIVERY APPLICATIONS

Jorma Roine

TURUN YLIOPISTON JULKAISUJA – ANNALES UNIVERSITATIS TURKUENSIS
SARJA - SER. AI OSA - TOM. 599 | ASTRONOMICA - CHEMICA - PHYSICA - MATHEMATICA | TURKU 2019

Affiliation

Laboratory of Industrial Physics
Department of Physics and Astronomy
Faculty of Science and Engineering
University of Turku
FI-20014 Turku, Finland

Supervised by

Matti Murtomaa
Adjunct Professor
Department of Physics and Astronomy
University of Turku
Finland

Jarno Salonen
Professor
Department of Physics and Astronomy
University of Turku
Finland

Reviewed by

Wamadeva Balachandran
Professor
Center for Electronic Systems Research
Brunel University
London, UK

Leena Peltonen
Adjunct Professor
Division of Pharmaceutical Chemistry and Technology
University of Helsinki
Finland

Opponent

Lucian Dascalescu
Professor
Pprime Institute: Mechanical, Materials and Energy Engineering and Research
University of Poitiers
France

The originality of this thesis has been checked in accordance with the University of Turku quality assurance system using the Turnitin Originality Check service.

ISBN 978-951-29-7546-4 (PRINT)
ISBN 978-951-29-7547-1 (PDF)
ISSN 0082-7002 (Print)
ISSN 2343-3175 (Online)
Grano Oy - Turku, Finland 2019

Preface

In February 2005, during my M.Sc. studies at the University of Turku, I was asked out of the blue by Dr. Matti Murtomaa to work in the Laboratory of Industrial Physics as a part-time research assistant. I was thrilled and honored to get introduced to the inspiring crew and environment of our laboratory.

More of my dreams would soon after continue to be fulfilled. I spent the academic year 2005–2006 in Japan to study the language, after to return to Turku to finish my Master's degree in physics. Little did I know that on the day of my return in August 2006, I would have the pleasure to meet the love of my life in the laboratory: Dr. Maija Nyström, who at the time was a fellow undergraduate student. By June 2007, we were officially dating, and I had joined her band. We would both go on working in the laboratory, to later dissertate in the interdisciplinary fields of electrostatics and pharmaceutical physics. On September 1st, 2008, I finally embarked on my Ph.D. journey.

Let us briefly dwell on the significance of science. Humanity has always found a way to adapt or turn its course in times of crisis, to live another day. That being said, the true will to change our ways often only emerges when but a few choices remain. Currently, we are faced with unprecedented global challenges – overpopulation, extinction of wildlife, and climate change, which threaten loss of the Earth's biodiversity, and an ecological collapse. It is paramount for the future of our descendants and our planet that we deal with these problems resolutely today. I am hopeful that this can be realized. Science provides us with peaceful solutions to help us live our lives, and we have been invested with the power to influence our fate by making rational decisions. We can choose to partake in the effort by contributing to the advancement of science, whether or not we get to witness the outcome.

So if you ask me, scientific research and access to established knowledge hold more value now than ever before, and should not to be taken for granted. In the recent times, we have had the opportunity to witness plenty of incidents where the general public has been alienated from the meticulously established scientific views, or blatantly disconnected from scientific efforts to improve human lives – often for short-sighted personal gain of few. Of course, this is not a new phenomenon. At times throughout the known history, irresponsible misrepresentation or even demonization of science due to selfish reasons has dangerously threatened to undermine scientific progress by fueling public

tension over it. Human as such acts may be, regrettably they often are far from humane. Our advanced society exists owing to our natural eagerness and unrelenting efforts to explore and understand the world around us. Let us continue to engage in critical thinking, to question, and to follow our innate curiosity. Our collective discoveries – the fruits of science – belong to everyone.

In the form of this Ph.D. thesis, I am happy to contribute to the ocean of humanity's knowledge, if only a small vial – with a droplet of something new. I sincerely hope my present and future work may serve for the incremental betterment of humankind. I would like to take this opportunity to express my gratitude to the people who have made the completion of this work possible.

I humbly thank my opponent, Prof. Lucian Dascalescu. Prof. Wamadeva Balachandran and Dr. Leena Peltonen are acknowledged for reviewing the thesis.

Dr. Matti Murtomaa and Prof. Jarno Salonen, you had faith in me, shared your expertise, and provided me the freedom to pursue research in an excellent environment – thank you. Matti, your whole-hearted pioneering spirit and enthusiasm for electrostatics never fail to inspire those around you. Jarno, your dedication in porous silicon research is likewise exceptional. I appreciate your efforts as laboratory head to gather funding and to offer part-time work projects in difficult times to support this Ph.D. project, as well as others. Prof. Vesa-Pekka Lehto, as the head of the laboratory when I started out, you believed in me, and I'm grateful. Thank you for sharing your insights, and for providing funding to the project during the crucial first months.

The Graduate School of Materials Research (GSMR) is acknowledged for three-year funding of the Ph.D. project throughout 2009-2011. The Finnish Cultural Foundation, Varsinais-Suomi Regional Fund, funded the work for one year. A minor grant received from Turun Yliopistosäätiö is also acknowledged.

I sincerely thank all of my past and present colleagues, in particular the graduate students, who were always willing to help one another, and essential in defining the pleasant tone and solidary mood of our laboratory. Special thanks to Dr. Maija Nyström for the shared laughs, our fruitful discussions, and the co-authoring which was crucial for the completion of this thesis; Dr. Martti Kaasalainen, for the friendly support, long discussions, and collaboration; Ermei Mäkilä, for selflessly sharing your time on countless occasions; Outi Alanen and Janne Peltonen, for your uplifting resonance. For the work on the electroencapsulation apparatus, thank you to Mika Aarnio, and our workshop staff including Pasi Saarenmaa. The contributions from co-writers outside the

department are heartily acknowledged: Prof. Hélder Santos and his group; Prof. R. Mohan Sankaran; Dr. Markus Peurla; and Dr. Markko Myllys.

To all of my friends – I have been most grateful for your company during this work, you have given me your acceptance, and strength. I will never forget you. Special thanks to all my bandmates in Korpikuusen Kyynel during these years. The true veterans and staples in the band – Maija, Ville, and Antti – you deserve my utmost megathanks. Our bond is strong and special... just like heavy metal! Whenever we tell our stories in melody, or blow off our steam in harmony, I am bound by the laws of physics no more.

Thanks to my relatives, and my wonderful in-laws for the welcoming atmosphere and cheers. I feel at home with you.

To my family, thank you all for your support. Jyrki, as my big brother you have always had my back, and you have always listened. I am glad to have followed you to pursue my university studies in Turku. My sister Jaana, you were the one to introduce me to mathematics early on. Maija & Lauri, I am proud to call you my parents. I appreciate your love, your teachings, and the freedom to choose my own ambitions. I am thankful that we were able to raise a toast together to celebrate the completion of this Ph.D. thesis. My grandfather Arvi Sevola has also been a great influence for me, and we often discussed my early studies.

Finally, to my beloved fiancée Maija: For me, your beautiful smile is a fundamental force. Your love, warm encouragement, and radiant positivity have elevated me over the obstacles I have faced. From the bottom of my heart, I thank you for patiently standing at my side throughout this undertaking – sharing the countless moments of joy and hardship I've had, all the good times and the bad. I cherish every drop of the invaluable wisdom and morale, and the priceless humor you have sprinkled on me. For the pure joy of each day spent with you, I am in bliss. For the privilege of having worked alongside you, I am deeply honored. *Yhes myö taistellaa*.

Turku, December 2018

Jorma Roine

Abstract

In bi-polar parallel nozzle electroencapsulation, two oppositely charged droplet jets are produced by electrospraying (electrostatic atomization), a method of extracting micro- or nanodroplets from a body of liquid using electrical forces. The two species of droplets are attracted to each other due to Coulombic forces. Upon contact, droplets of similar size can merge into a single-phase, or form a core-shell capsule structure, depending on the mutual miscibility of the liquids.

In this work, an electroencapsulation setup was designed and experimented for the single-step production of two types of drug carrier particles of 10–50 μm in size: wrinkled, solid Eudragit L 100 enteric polymer micromatrix particles; and spherical microcapsules consisting of a solid Eudragit E 100 polymer shell and a liquid glycerol core. The carrier particle payload consisted of a model drug (griseofulvin); or griseofulvin loaded, mesoporous silicon (PSi) nano- and microparticles, which themselves are functional drug carriers. The goal was to obtain the carrier particle payloads as either stable drug dispersions in a disordered solid state, or non-agglomerated PSi nanoparticle dispersions, to enhance the drug dissolution properties at release. The carrier formulations would effectively render the payload in the form of an inert micropowder for purposes of handling and dosing. In oral administration, the formulations were to shield the payload from intestinal metabolism, and to restrain its release until arrival to target pH-conditions.

The carrier particles were characterized to evaluate these properties. The micromatrix particles were proven stable and gastro-resistant *in vitro*. Griseofulvin dissolution and absorption properties improved significantly, the latter especially for the drug loaded PSi payloads. Finally, the efficiency of the asymmetric core-shell microcapsule production was optimized using Taguchi techniques. In conclusion, electroencapsulation was found to be a potentially feasible method to improve the oral bioavailability of poorly soluble drugs.

Furthermore, partially crystalline piroxicam microparticles were produced by electrospraying, and characterized. The crystalline phase was shown to consist of a previously unknown, stable polymorphic form of piroxicam. The result suggests the method could provide a unique way to produce novel drug polymorphs. Thus, it is possible that the dissolution properties of certain drug materials could be improved sufficiently to facilitate oral administration, without the necessity to use more complex formulations.

Tiivistelmä

Vastakkaismerkkisin rinnakkaissuuttimin tehtävässä sähkökapseloinnissa tuotetaan kaksi vastakkaisesti varautunutta pisarasuihkua sähköstaattisen atomisaation avulla. Erimerkkisesti varautuneiden nesteiden pisarat vetävät toisiaan puoleensa. Saman kokoluokan pisarat voivat siten yhdistyessään sekoittua yhtenäiseksi faasiksi tai muodostaa kapselirakenteen kerrostumalla toistensa päälle, riippuen nesteiden keskinäisestä sekoittuvuudesta.

Tässä väitöstutkimuksessa suunniteltiin sähkökapselointilaitteisto, jonka avulla tuotettiin kahdenlaisia suun kautta annettavaksi tarkoitettuja lääkekuljetinpartikkeleita 10–50 µm:n kokoluokassa: poimuisia Eudragit L 100 -polymeerimikromatriisipartikkeleita sekä pallomaisia mikrokapseleita, joissa oli kiinteä Eudragit E 100 -polymeerikuori ja nestemäinen glyseroliydin. Kuljetinpartikkelien hyötykuormana käytettiin griseofulviinia joko sellaisenaan tai ladattuna mesohuokoisesta piistä (PSi) koostuvien mikro- tai nanopartikkelien huokosiin. Yksivaiheisen tuotantoprosessin tarkoitus oli parantaa lääkeaineen liukenevuutta sen vapautuessa kuljetinpartikkeleista. Siksi puhtaan lääkeaineen haluttiin kapseloituvan kuljettimiin järjestäytymättömänä, kiinteänä dispersiona. Lääkeainein ladatut PSi-partikkelit dispergoitiin kuljetinväliaineeseen agglomeroitumattomina. Kuljetinpartikkelien tehtävinä oli vakauttaa hyötykuorma ja helpottaa sen käsittelemistä, suojata kuormaa ruoansulatuksen metabolialta ja lopuksi vapauttaa se tietyissä pH-olosuhteissa.

Lääkekuljetinpartikkelien ominaisuuksia arvioitiin eri menetelmin. Mikromatriisipartikkelit osoittautuivat stabiileiksi ja gastroresistenteiksi *in vitro*. Vapautuneen griseofulviinin liukenevuus parani merkittävästi, kuten myös sen imeytyminen – erityisesti PSi:hin ladattaessa. Epäsymmetrisen mikrokapselituotantoprosessin tehokkuus optimoitiin Taguchi-menetelmin. Sähkökapselointi todettiin lupaavaksi menetelmäksi suun kautta annettavien niukkaliukoisten lääkeaineiden biologisen hyötyosuuden parantamiseksi.

Tutkimuksessa tuotettiin lisäksi sähköstaattisen atomisaation avulla osittain kiteisiä piroksikaamimikropartikkeleita, joiden kiteisen faasin todettiin koostuvan entuudestaan tuntemattomasta stabiilista polymorfista. Löydös viittaa mahdollisuuteen, että uusia kiderakenteita voitaisiin tuottaa menetelmän avulla muistakin lääkeaineista. Näin tälläkin menetelmällä olisi kenties mahdollista parantaa joidenkin lääkeaineiden liukenevuutta riittävästi niiden antamiseksi suun kautta, turvautumatta monimutkaisempaan formulointiin.

List of Original Publications

This Ph.D. thesis is based on the following original publications, hereafter referred to as papers I–IV:

I J. Roine, M. Murtomaa, M. Myllys, J. Salonen, *Dual-capillary electroencapsulation of mesoporous silicon drug carrier particles for controlled oral drug delivery*, J. Electrost. **70**, 428-437 (2012).

II M. Nyström, J. Roine, M. Murtomaa, R. M. Sankaran, H. A. Santos, J. Salonen, *Solid state transformations in consequence of electrospraying – a novel polymorphic form of piroxicam*, Eur. J. Pharm. Biopharm. **89**, 182-189 (2015).

III J. Roine, M. Kaasalainen, M. Peurla, A. Correia, F. Araújo, H. A. Santos, M. Murtomaa, J. Salonen, *Controlled dissolution of griseofulvin solid dispersions from electrosprayed enteric polymer micromatrix particles: physicochemical characterization and in vivo evaluation*, Mol. Pharmaceutics **12**, 2254-2264 (2015).

IV J. Roine, M. Murtomaa, J. Salonen, *Influence of parallel nozzle electroencapsulation parameters on microcapsule properties – a case study using the Taguchi robust design method*, J. Electrost. **90**, 91-105 (2017).

Constants, Quantities and Abbreviations

$e = 1.6021773 \times 10^{-19}$ C	Elementary charge
$g = 9.80665$ m/s^2	Acceleration due to gravity (standard)
$G = 6.67259 \times 10^{-11}$ Nm^2/kg^2	Gravitational constant
$\varepsilon_0 = 8.85419 \times 10^{-12}$ F/m	Vacuum permittivity

a	Distance between guard and extractor electrodes
c	Thickness of extractor electrode
d	Droplet diameter (size)
$\bar{d}$	Volume mean droplet diameter
d_0	Characteristic jet diameter
d_i	Nozzle inner diameter
d_j	Jet diameter
d_med	Volume median droplet diameter
d_o	Nozzle outer diameter
h	Perpendicular distance between extractor electrode and nozzle tip
l	Droplet trajectory length
m	Mass
n_c	Number of core liquid electrosprays
n_s	Number of shell liquid electrosprays
p	Pressure
q	Electric charge
$\bar{q}$	Volume mean droplet charge
q_caps	Capsule electric charge
q_s	Sphere electric charge
q_R	Rayleigh limit electric charge
r	Distance
r	Droplet radius
s	True solubility
s_app	Apparent solubility
t	Time
v	Droplet velocity
v_s	Surface velocity of liquid
v_t	Droplet terminal velocity
w	Weight

A	Surface area, projection area
C	Concentration
C_{pol}	Polymer concentration
C_x	Concentration of substance x
C_D	Drag coefficient
D	Capsule diameter
E	Electric field strength
E_{s}	Surface electric field strength
F	Force
G	Gibbs free energy
H	Enthalpy
I	Atomization electric current
I_0	Characteristic current
I_{c}	Core liquid atomization electric current
I_{s}	Shell liquid atomization electric current
L_0	Characteristic jet length
Q	Liquid flow rate
Q_0	Characteristic liquid flow rate
Q_{c}	Core liquid flow rate
Q_{min}	Minimum liquid flow rate
Q_{s}	Shell liquid flow rate
R	Resistance
R_0	Characteristic jet radius
S	Entropy
T	Temperature
U	(Atomization) voltage
U_{c}	Core liquid atomization voltage
U_{s}	Shell liquid atomization voltage
V	Electric potential
V	Volume
W	Evaporation rate
$Ø$	Extractor electrode hole diameter
α	Dimensionless permittivity constant
β	Scaling law exponent
δ_η	EHD Reynolds number (viscous dimensionless parameter)
γ	Surface tension
γ_{c}	Core liquid surface tension

γ_s	Shell liquid surface tension
ε	Permittivity
ε_r	Relative permittivity (dielectric constant)
η	Viscosity
2θ	Diffraction angle
λ	Wavelength
ν	Scaling law exponent
ξ	Scaling law exponent
ρ	Density
σ	Surface charge density
χ	Scaling law exponent
K	Electric conductivity

ANOVA	Analysis of variation
BCS	Biopharmaceutics Classification System
CJM	Cone-jet mode
DAG	Delft aerosol generator
DCM	Dichloromethane
DSC	Differential scanning calorimetry
EHD	Electrohydrodynamic
FFE	Fractional factorial experiment
FTIR	Fourier transform infrared
GE	Griseofulvin-Eudragit L 100 (micromatrix particle)
GI	Gastrointestinal
GPE	Griseofulvin-PSi-Eudragit L 100 (micromatrix particle)
HBSS	Hank's balanced salt solution
HPLC	High performance liquid chromatography
nanoCT	X-ray nano-computed tomography
OA	Orthogonal array
PBS	Phosphate-buffered saline
PdI	Polydispersity index
PEG	Polyethylene glycol
POM	Polyoxymethylene
PSi	Porous silicon
PTFE	Polytetrafluoroethylene
PVP	Polyvinylpyrrolidone
RH	Relative humidity

S/N	Signal to noise ratio
SEM	Scanning Electron Microscopy
TCPSi	Thermally carbonized porous silicon
TEER	Transepithelial electrical resistance
TEM	Transmission Electron Microscopy
THCPSi	Thermally hydrocarbonized porous silicon
TOPSi	Thermally oxidized porous silicon
TGA	Thermogravimetric analysis
UV/Vis	Ultraviolet/visible
XRD	X-ray diffraction
μCT	X-ray micro-computed tomography

Contents

Preface ..... **iii**
Abstract ..... **vi**
Tiivistelmä ..... **vii**
List of Original Publications ..... **viii**
Constants, Quantities and Abbreviations ..... **ix**
Contents ..... **xiii**
1. Introduction **1**
2. Background and Theory **5**
2.1. Electrostatics 5
2.1.1. Electric charge 5
2.1.2. Electrostatic Force 5
2.1.3. Electric Potential 7
2.1.4. Charge Transfer 7
2.1.4.1. Contact and Frictional Charging 8
2.1.4.2. Induction Charging 10
2.1.4.3. Corona Discharging 11
2.1.4.4. Other Mechanisms of Charging and Discharging 12
2.2. Electrostatic Atomization 13
2.2.1. Principles of Electrospraying Apparatus 13
2.2.2. Electrospraying Mode Characteristics 16
2.2.2.1. Dripping and Microdripping Modes 17
2.2.2.2. Cone-Jet Mode 18
2.2.2.3. Other Modes 20
2.2.3. Droplet Charge 21
2.2.4. Properties of Electrospraying in Cone-jet Mode 22
2.2.4.1. Liquid prerequisites 25
2.2.4.2. Droplet Size and Atomization Current 27
2.2.5. Droplet Evaporation and Coulomb Fission 31
2.2.6. Droplet Neutralization 33
2.3. Electroencapsulation 34
2.3.1. Material prerequisites 35
2.3.2. Electroencapsulation methods 36
2.3.2.1. Single Nozzle 38
2.3.2.2. Bi-Polar Parallel Nozzles 38

2.3.2.3. Co-Axial Nozzles 42
2.3.2.4. Other Methods 42
2.4. Oral administration of Solid Drug Materials 43
2.4.1. Solid State of Pharmaceutical Materials 43
2.4.1.1. Drug Structural Stability 45
2.4.1.2. Drug Solubility 46
2.4.2. Oral Bioavailability of Drugs 47
2.4.2.1. Drug Dissolution 47
2.4.2.2. Intestinal Drug Permeation 48
2.4.2.3. First-Pass Metabolism 49
2.4.3. Drug Carrier Formulations to Improve Oral Bioavailability 49
2.4.3.1. Drug Solid Dispersions and Solid Solutions 50
2.4.3.2. Drug Loading to Porous Silicon Particles 51
3. Experimental 53
3.1. Materials 53
3.1.1. Model Drugs 53
3.1.2. Polymers 54
3.1.3. Solvents and Additives 54
3.1.4. Mesoporous Silicon Particles 54
3.1.5. Phosphate-Buffered Saline 55
3.2. Methods 55
3.2.1. Electrospraying Methods 55
3.2.1.1. Bi-Polar Parallel Nozzle Electroencapsulation 55
3.2.1.2. Electrospraying of Drug Particles 58
3.2.2. Atomization Current Measurement 59
3.2.3. Weighing 60
3.2.4. Optical Microscopy 60
3.2.5. Scanning Electron Microscopy 60
3.2.6. Transmission Electron Microscopy 61
3.2.7. X-Ray Computed Tomography 61
3.2.8. X-Ray Diffraction 61
3.2.9. Thermogravimetric Analysis 62
3.2.10. Differential Scanning Calorimetry 62
3.2.11. High Performance Liquid Chromatography 62
3.2.12. Raman Spectroscopy 63
3.2.13. Fourier Transform Infrared Spectroscopy 63
3.2.14. UV/Vis Spectroscopy 63

3.2.15. *In Vitro* Drug Dissolution Modelling 64
3.2.16. *In Vitro* Drug Permeation Modelling 64
3.2.17. Taguchi Experiment Design 64
4. Results and Discussion on Papers 67
4.1. Paper I 67
4.2. Paper II 69
4.3. Paper III 71
4.4. Paper IV 73
5. Conclusions 77
References 79
Original Publications 111

1. Introduction

Drug materials are usually administered via the oral route, if possible. The method is relatively comfortable for the patient, cost effective, and provides good dosing control. However, oral drug administration is not always feasible. It has been estimated that most new promising drug candidates suffer from poor physicochemical or pharmacokinetic properties such as low solubility, slow dissolution rate in the intestinal lumen, poor permeation of the gastrointestinal (GI) tract wall, and high first-pass metabolism [1–4]. As a result, an adequate bioavailability of the drug may not be obtainable when the drug is administered orally.

Strategies exist to address drug oral bioavailability issues, and the relevant drug properties can be enhanced. For instance, the drug dissolution can be improved by increasing the specific surface area of the drug in the formulation. While simple milling or spray drying of the drug will often suffice, more advanced methods are sometimes necessary [5]. Another method to improve dissolution is by formulating the drug in a more energetic (disordered) solid state, such as an amorphous state – though it is generally susceptible to stability issues [6]. However, in solid dispersion formulations, a disordered solid state of the drug can be stabilized while simultaneously increasing the drug surface area [7]. The drug bioavailability requirements and concerns specific to the medication scenario are determined by *e.g.* the relevant drug material or combination of drug materials, the diagnosis, as well as both inter- and intra-patient physiological variations [2,8]. With other factors to consider, such as the targeted shelf life and cost of the formulation, it is obvious that a versatile methodological palette to enhance oral bioavailability is necessary.

In this thesis, novel approaches are taken to improve the oral bioavailability of poorly soluble drugs by means of electrospraying and bi-polar parallel nozzle electroencapsulation techniques.

Electrospraying is a method of dispersing a suitable bulk liquid into micro- or nanodroplets by electrical forces [9]. The method can be used for the production of crystalline or amorphous micro- or nanoparticles of a compound dissolved to the electrosprayed liquid [10]. For electrosprayed particles of a poorly water-soluble drug, dissolution is improved due to the large surface area. Often more importantly, the dissolution properties can be significantly affected by the drug solid state, *i.e.* its crystallinity and polymorphic form [5,11]. The amorphous form often exhibits far better dissolution properties, as compared to the known crystalline polymorphs [12,13]. But, the gains to the dissolution properties can be nullified by the instability of the amorphous state [6]. In the present work, a novel stable polymorphic form of piroxicam was produced by electrospraying microparticles of the drug. The discovery presented electrospraying as a potential crystal engineering approach to improve the dissolution rate of a drug to a degree, while retaining a high stability [14,15].

The main focus of the present work was in investigating and optimizing bipolar parallel nozzle electroencapsulation as a single-step method to produce formulations of solid, functional drug carrier microparticles that would be chemically inert, physically stable, as well as mechanically durable, handleable, and dosable. The purpose was to potentially enhance the oral bioavailability of poorly soluble or otherwise problematic drug materials by means of stabilizing and shielding the disordered drug dispersion, and thus retaining the improved dissolution properties until its pH-controlled release at the optimal drug absorption site.

The principle of the electroencapsulation technique was to impact oppositely charged electrosprayed droplets, which mutually attract due to Coulombic forces. From the combined droplets, two types of drug carrier particles were obtained after excess solvent evaporation: core-shell microcapsules consisting of a glycerol core and a solid Eudragit E 100 polymer shell, and solid Eudragit L 100 polymer micromatrix particles. As the micromatrix particle payload, a poorly soluble model drug was dissolved to the electrospraying liquid, and the drug was enveloped in the particles as a stable, disordered solid dispersion. Alternatively, the drug was pre-loaded into micro- or nanoparticulate mesoporous silicon (PSi), in itself a promising candidate for an orally administrable drug carrier material [16–18]. The PSi particle payload was then electroencapsulated as non-agglomerated dispersions in the micromatrix particles, or microcapsule cores. The electroencapsulated drug carrier particles were characterized. The drug dissolution and permeation

performances were evaluated *in vitro* for the micromatrix particles. Finally, optimization of the electroencapsulation process parameters was considered in particular for the asymmetric core-shell microcapsule production. In the following paragraphs, the motivation and objectives for the experimental work in each individual paper are specified and summarized briefly.

A variable geometry bi-polar parallel capillary electrospraying device was designed and constructed for the electroencapsulation experiments, and introduced in paper I. The design was based on a previously built electrospraying device, which was used in paper II.

A substantial groundwork was conducted to select the materials for the electroencapsulation experiments. Suitable electroencapsulation parameters such as geometry, liquid flow rates Q_i, and electrospraying voltages U_i, were mapped for a wide range of electrospraying liquid compositions, consisting of different combinations of various solvents, polymers, and additives. As a result, two types of promising carrier particles were produced by electroencapsulation and characterized in paper I: firstly, core-shell microcapsules, with an Eudragit E 100 polymer shell that dissolves in the stomach pH conditions, and PSi micro- or nanoparticles dispersed in a liquid glycerol core; and secondly, solid micromatrix particles with griseofulvin loaded PSi nanoparticles dispersed to an enteric polymer (Eudragit L 100) matrix.

During preliminary electrospraying experiments by Dr. Maija Nyström for a previous work [13], partially crystalline particles, of which the X-ray diffraction (XRD) patterns could not be identified, were produced by electrospraying a chloroform solution of piroxicam. The unknown crystalline phase was highly reproducible by electrospraying, but could not be produced by any attempted alternate methods, such as exposing a chloroform solution of piroxicam to a strong electrical field in an evaporation dish. The finding raised questions as to whether a novel polymorphic form of piroxicam had been discovered by electrospraying. The purpose of paper II was to answer these questions: partially crystalline particles, with the crystalline phase of the suspected new polymorphic form of piroxicam, were produced in various electrospraying conditions, characterized extensively with emphasis on XRD methods, and monitored for stability considerations.

A larger electroencapsulation chamber design was introduced in paper III. The purpose was to improve the electroencapsulation collection efficiency, and to enhance the solvent evaporation from the produced droplets, microcapsules and micromatrix particles without the necessity of additional air flow, excessive

heating, or depressurization. In paper III, further investigation was conducted on the electroencapsulation of griseofulvin and griseofulvin loaded PSi nanoparticles in Eudragit L 100 polymer micromatrix particles as solid dispersions. Controlled dissolution and permeation properties of the electroencapsulated griseofulvin were evaluated *in vitro*, and compared to the performance of free griseofulvin. The stability of the micromatrix particles was monitored in accelerated conditions over a period of six months.

The work in paper IV was focused on the optimization of the bi-polar parallel nozzle electroencapsulation process in the production of Eudragit E 100-glycerol core-shell microcapsules with a PSi nanoparticle payload. The significance of ten different electroencapsulation parameters (factors) on the measured electroencapsulation process quantities, such as capsule yield and composition, was evaluated in a coarse fractional factorial experiment (FFE). The purpose was to identify the important factors, and to draft a general strategy for optimizing the efficiency of any electroencapsulation process of a similar type. Additional examination of the electroencapsulation process efficiency was performed by sweeping the core liquid flow rate Q_c, and comparing relevant electroencapsulation process quantities with the measured electrosprayed droplet size and charge distributions.

2. Background and Theory

2.1. Electrostatics

Electrostatics is the science of *static electrical charges* – charges that are at rest relative to the observer, or closely so. A configuration of static charges constitutes an *electrostatic* system, or a system *at electrostatic conditions*. With such a system at (near) equilibrium, all electric currents, magnetic fields due to moving charges, and interactions of charges with external magnetic fields can be considered to be negligible for the observer [19]. *Electrostatic phenomena* stem from the interactions between static charges and/or charged bodies [20].

2.1.1. Electric charge

The electric charge q is a quantized fundamental property of elementary particles. Charge can be positive or negative: the charge of a proton is equal to the elementary charge e, while that of an electron is $-e$. A neutron carries zero charge, and is therefore electrically *neutral*. In a (conceptually) isolated system, net charge is conserved. In 1909, the value of e was first measured to an accuracy of 1% by Robert A. Millikan and Harvey Fletcher, using the oil-drop method which Millikan continued to refine [21].

2.1.2. Electrostatic Force

The central interaction in electrostatics is the *electrostatic force*. It is governed by *Coulomb's law*:

$$\boldsymbol{F}_{ij} = \frac{1}{4\pi\varepsilon_0}\frac{q_i q_j}{r_{ij}^2}\hat{\boldsymbol{r}}_{ij}, \qquad (1)$$

where $\boldsymbol{F}_{ij}$ is the force exerted on point charge q_i by point charge q_j, and $\hat{\boldsymbol{r}}_{ij} = (\boldsymbol{r}_i - \boldsymbol{r}_j)/|\boldsymbol{r}_i - \boldsymbol{r}_j|$ is the unit vector distance between the charges. A

manifestation of the fundamental *electromagnetic force*, the electrostatic force can be presented as an abstract field. At a given point $\boldsymbol{r}$, the net *electric field* $\boldsymbol{E}(\boldsymbol{r})$ due to a static charge distribution simplifies to

$$\boldsymbol{E}(\boldsymbol{r}) = \boldsymbol{F}(\boldsymbol{r})/q_0, \tag{2}$$

where $\boldsymbol{F}(\boldsymbol{r})$ is the net electrostatic force exerted on a stationary test charge q_0 at point $\boldsymbol{r}$ by the external charge distribution. As seen from Equation 1, the electrostatic force between two charges of different signs is *attractive*, and the force between two charges of the same sign is *repulsive*.

Analogous to the electrostatic force is the fundamental gravitational force which obeys the inverse-square law of gravity, obtainable from Equation 1 for point masses by making the following replacements: $q \to m$ (mass), and $1/4\pi\varepsilon_0 \to G$ (gravitational constant). However, negative mass has never been observed, and only attractive gravitational forces have been proven to exist outside theoretical considerations [22–24]. Magnitude comparison of these forces reveals that in general, electrostatic force utterly dominates over gravitational force in interactions between submicron ($< 10^{-6}$ m) objects, with the possible exceptions of neutral conductors or extremely condensed matter close below this size limit. Matter is bound together at the atomic level by electrostatic forces: electrons are attracted to the vicinity of atomic nuclei to complete atoms [25]; atoms can bond together by electrostatic forces to form molecules [26]; and finally atoms, ions, and molecules compose *crystalline* or *amorphous* solids (Chapter 2.4.1). Generally, the relative importance of gravitational attraction grows for more massive objects, in part because the effects of charges of different signs cancel each other out, and in part because the sustainable net charge density of a physical body is limited (*cf.* Chapters 2.1.4.3–4). At astronomical scales ($> 10^7$ m), gravitational force absolutely dominates over electrostatic force – celestial bodies and objects, such as the Earth, the Milky Way, and the Laniakea, are held together by gravity [27]. At the extreme, the squeeze of gravitational force is able to transform matter into a singularity [28].

The very existence of stable solid matter, including the human body, is perhaps the most perceptible manifestation of electrostatic force. For an inhabitant of the Earth, all tangible sensations originate from electrostatic forces, with the sole exception of the downward acceleration induced on our every bone by the constant gravitational pull of the planet's combined mass. In spite of the gravitational force, one is able to stand at rest on the planet's surface

without collapsing or falling. This is owing to a fundamentally electrostatic net normal force, pushing back from the ground on the bottoms of the recipient's feet (or equivalent). The interaction is relayed via connected hard and soft body tissues, distributing to each cell of the body to uniformly balance the gravitational force and thus counter the acceleration relative to Earth.

May the electrostatic force be with you as you read this book further, you will need it.

2.1.3. Electric Potential

The concept of a scalar *electric potential* V is a useful tool in electrostatics. At electrostatic conditions, where Equation 2 applies, the potential V at point $\boldsymbol{r}$ can be defined as

$$V(\boldsymbol{r}) = -\int_{\infty}^{\boldsymbol{r}} \boldsymbol{E} \cdot \mathrm{d}\boldsymbol{r} + V_{\infty}, \tag{3}$$

where V_{∞} is a constant. In the electrostatic case, the potential difference ΔV and *voltage* U between two points are equal [19]. For a finite charge distribution, V_{∞} corresponds to V at infinity: $\lim_{r \to \infty} V(\boldsymbol{r}) = V_{\infty}$. In this book, V_{∞} defaults to 0 for convenience.

2.1.4. Charge Transfer

As opposed to a single atom where all permitted electron energies are separate and discrete, the energy levels of interacting atoms in a solid can be treated as being split into energy *bands* of effectively continuous energy ranges [20,29]. The outer, most energetic electrons occupy the *valence* band, and excited electron states form the *conduction* band.

In a c*onductor*, the valence band is partially empty, or electrons overflow to the conduction band which is connected to or overlaps with the valence band. In such a solid, valence electrons are able to move into new energy states and electrical conductivity is high. For an applied electric field $\boldsymbol{E} \neq 0$ in a conductor, a net electron flow is generated and observed as an electric current [20,29].

In an *insulator*, the valence band is full, and in accordance to the Pauli Exclusion Principle, electrons cannot move into new energy states. Therefore, electrons in the valence band can transfer no charge. The conduction band is empty and separated from the valence band by the *forbidden* band with very few or no energy states. The conductivity of an insulator is low, and greatly

depends on the density and mobility of ions; density of impurities, structural defects, and molecular-ion traps that can generate localized energy states in the forbidden band; as well as the *band gap* energy [20,29,30]. S*emiconductor* materials have the insulator band structure but the band gap is relatively small, so thermal or optical excitation of electrons is feasible [29].

An isolated charge distribution rearranges spontaneously until an thermodynamic equilibrium configuration of the system is reached, equating to a local potential energy minimum. Charge is redistributed within objects and transferred between them by the realignment, relocation, and exchange of charged particles, namely electrons or ions. For a conductor, where electron movement is relatively unrestricted, any net charge accumulates to the surfaces in electrostatic conditions, and surface charge density σ increases with positive surface curvature [31]. The charge distribution is uniform for a spherical conductor surface far from other charge.

Mechanisms of charge transfer between objects are determined by the physical state, conduction properties, and charge density of both the interacting objects and the medium, contacts between the objects, adsorbed layers on object surfaces, and available charge carrier species. As an example, nearly all objects in atmospheric conditions are covered by at least a monolayer of water, an excellent solvent capable of containing an electric double layer [32]. A moisture layer thus generally acts as a potential barrier for electrons to some degree [33]. Consequently, various ions that dissolve to the water film from the object surface can be significant surface charge carriers, especially for insulators [20,32].

2.1.4.1. Contact and Frictional Charging

Contact charging (*contact electrification*), or charge transfer between objects that are brought to a *non-sliding* contact and subsequently separated, is a surface phenomenon that is satisfactorily explained by the electron energy band model (Chapter 2.1.4.) only for two conductors with ideal, uncontaminated surfaces. When brought to contact, a difference between the work functions of the conductors drive a transfer of electrons that results in a repeatable contact potential difference between the conductors [34]. At conductor separation, a charge backflow occurs by electron tunneling, and cuts off when the distance between closest points of separation exceeds about 1 nm [35,36]. Assuming that the total charge remains constant, the backflow nearly equalizes the conductor potentials. Thus, between two initially equipotential conductors, the full

contact charging cycle results in a most often negligible net charge transfer. However, accumulated contact charge can be significant in a large number of small conductors, such as metal powders [37,38].

Contact charging is vastly more complicated when one or both of the contacting objects are insulators, particularly so for *dielectrics* [39,40]. With an insulator involved, contact charging generally results in a significant amount of charge being transferred between the contacting objects [34,39,41]. For insulators, the probability of electron transfer varies greatly with local surface energy state density. The process could be quite energy selective, as determined by the contacting material [30]. The amount of electron energy states involved in the contact charging is further limited by the actual contact area, influenced by surface roughness, macroscopic contact area and contact pressure [39]. Bulk states close to the surface may contribute to electron transfer to a limited degree [42]. Importantly, surface contaminations may give rise to an electric double layer or mobile surface ions (Chapter 2.1.4.), potentially hindering electron transfer and diminishing its significance in the charging, in favor of ion transfer [20,32]. Charge can also be transferred by exchange of nano-sized bits of material [41].

True contact charge is principally a material property in ideal conditions – measured in a vacuum for a single contact of repeatable force and duration, between uncontaminated surfaces of consistent shape and morphology. Different materials can be arranged in *triboelectric series* according to the tendencies to charge either positively or negatively when contact charged with another, particular material [38,43]. As an extreme example, PTFE (Teflon) charges negatively when rubbed against virtually any other material [38,44,45]. However in general, triboelectric series are not unambiguous [20,38]. Lately, nanogenerators based on triboelectricity have been researched [46].

In real contacts, sliding occurs; surfaces are imperfect; and external variables such as temperature T, moisture, pressure p, and atmospheric composition cannot be ignored. To describe more realistic contacts, the term *frictional charging* is used of charge transfer between two objects that rub against each other. In frictional charging, the contact area is larger in at least one of the objects as compared to contact charging, and generally more charge is transferred [41,44]. Friction charging is less dependent on the materials, and is sensitive to the size and shape of the rubbed objects and contact areas, rubbing velocity, contact pressure, and contact temperature [20,47,48].

2.1.4.2. Induction Charging

As explained by Michael Faraday after performing his famous ice pail experiment in 1843, conductive materials can gain charge by *induction* [49]. Two processes of *induction charging* is demonstrated schematically in Figure 1 for an initially neutral sphere. Following the upper row of images in the figure from left to right, the proximity of a charged object, in this case a positively charged rod electrode, causes an *induced charge separation* within the sphere due to electrostatic forces. Grounding the sphere at this configuration allows for negatively charged electrons to enter the sphere from the ground to fill vacant electron states. Equivalently, the vacancies can be considered as positive charges which flow to the ground. This charge transfer, or induction charging of the sphere, ceases at net force equilibrium. At that point the net charge of the sphere has become negative, and remains so once the sphere is disconnected from the ground.

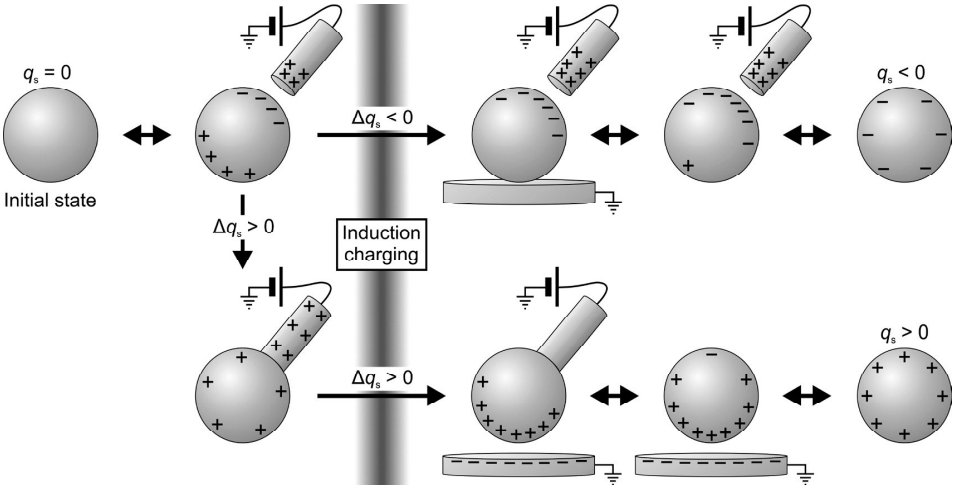

Figure 1. Two processes of induction charging a sphere with an initial net charge $q_s = 0$. The illustrated states show charge distributions at equilibrium. The intermediate arrows indicate the reversibility of the transitions, with the signs of any changes in q_s indicated. The two transitions that involve induction charging are highlighted with a top-to-bottom vertical bar.

In another scenario, shown in Figure 1 (transition to the bottom row), the sphere is first contact charged positively by bringing it to contact with the rod electrode. In the bottom row sequence of the figure, additional positive charge is subsequently transferred to the sphere by induction charging. A nearby

ground electrode induces charge separation in the sphere and the connected rod, with negative charge flowing from the sphere via the rod electrode circuit to the ground. After separating the sphere from the rod, the sphere is left with a net positive charge greater than that gained earlier from merely contacting the rod.

Many electrostatics devices and measurement instruments, such as Faraday cages, Faraday cups, electrometers and electric field meters, are based on induced charge separation [49–51]. A simple coaxial induction probe is capable of simultaneously measuring the charge, size and distance of a passing object [52]. Under suitable conditions, charged droplets can be extracted from a body of a sufficiently conducting liquid by induction charging the liquid surface. This phenomenon is discussed in Chapter 2.2 (Electrostatic Atomization).

2.1.4.3. Corona Discharging

The maximum charge density of an object is limited by several phenomena. For practical purposes, the most common limiting factor is the air *breakdown strength* – the electric field strength required for air *ionization*, which is approximately $E_{max} = 3 \times 10^6$ V/m for air at normal pressure, with lowest values observed for dry as compared to humid air [53–55]. Above this limit, electrons accelerated in the electric field can gain enough energy between collisions to detach another electron from atoms they collide with. Thus, avalanches of ionizing electrons (Townsend avalanches) are formed in the breakdown region [56]. If the electric field above the surface of a charged object exceeds the breakdown limit, the surface is discharged via the ionized air. This limits the attainable charge density of any surface exposed to an air atmosphere to a maximum of $\sigma = 2.6 \times 10^{-5}$ C/m^2, as obtained from Gauss's law.

A *corona discharge* is a low-energy type *point discharge* that occurs in a limited region of air or another ionizing gas next to an electrode of a high positive curvature, if its associated non-uniform electric field locally exceeds the breakdown strength of the gaseous medium [20,57,58]. Due to the ionization (plasma formation) process, an aerial corona discharge emits a faint blue glow and is thus traditionally dubbed St. Elmo's fire among sailors and aircraft pilots [59]. Charge is carried away from the corona discharge region and the sharp corona electrode mostly by relatively slowly moving unipolar ions which share the sign of the corona electrode. If the surrounding gas does not contain enough electronegative atoms to capture the electrons ejected from a negative corona discharge, it is also possible for slow electrons to remain a significant

charge carrier species outside the discharge region. Surfaces and particles can gain charge or be neutralized in the electric field of a corona discharge by attracting charge carriers it expels [20,60]. A corona discharge produces no sparking, unlike more energetic point discharges such as lightning [58].

2.1.4.4. Other Mechanisms of Charging and Discharging

The electrical conductivity K of a liquid depends on its ion concentration and ion mobility. For example, water is normally an excellent conductor of electricity, because even tap water contains an abundance of dissolved salts in the form of ions such as Na^+, K^+, Ca^{2+}, Mg^{2+}, F^-, and Cl^-. However, ultra-pure distilled water only contains relatively very few OH^- and H_3O^+ ions due to auto-dissociation of H_2O, and is actually a poorly conducting, albeit arduous to obtain, liquid [61]. In any dielectric liquid, dissociated ions form electric double layers at the liquid interfaces, even when the liquid body is on average electrically neutral [62]. Charging occurs in the liquid whenever any of the liquid interfaces are disrupted [20]. Poorly conducting (K of 10^{-9}–10^{-3} μS/cm) or isolated liquids can hold a net charge, provided that the liquid contains or obtains enough dissociated ions to store the charge [20]. Liquid bodies that contain dissociated ions may deform in an external electric field, in order for Coulombic forces to reach balance with other external forces and the liquid surface tension.

As discussed in Chapters 2.1.4.1 and 2.1.4.3, free charge carriers such as electrons, ions, or macroscopic charged particles can be produced by gas ionization, or by mechanical detachment of material from charged objects. In addition, such charge carriers can originate from, for example, nuclear reactions that produce alpha or beta radiation [63], electron field emission [64], electron photoemission [65], or solute and dispersed material left over from evaporated charged liquid droplets [66].

In a gas atmosphere that contains free charge carriers, highly charged objects disconnected from the ground and voltage sources tend to neutralize over time when no external electric field is present. Coulombic attraction draws nearby free carriers of oppositely signed charge into contact with the charged object, and charge is transferred via contact to achieve electrostatic equilibrium. On the other hand, particles or objects in a gas can also be charged by *diffusion charging*, due to random collisions with ions in thermal motion that have sufficient kinetic energy to overcome the Coulombic potential energy barrier of the particle or object in question. Diffusion charging can become significant for

particles of *ca*. 3 μm or smaller in size. In principle, charge can build up to the discharge limit by diffusion charging [20]. For notably larger objects, an equilibrium charge is reached when charge transfer due to the opposing mechanisms balance each other out.

In vacuum, the maximum charge density of an object is ultimately determined by the *electron field emission* limit (*cf.* Chapter 2.2.3). At the material specific electron field emission limit, the electric field strength at the surface of the object is sufficient for tunneling and subsequent emission of electrons from the object [64,67]. Electron field emission has been proposed as a method of spacecraft neutralization [68].

2.2. Electrostatic Atomization

Electrostatic atomization of a liquid, or breaking up a liquid into a jet of charged droplets by electrical forces [62,69,70], is the foundational electrostatic phenomenon for the present work. The technique is synonymously dubbed *electrospraying* [9], *electrostatic spraying* [71], *electrostatic dispersion* [72], *electrically forced jets* [73], *electroatomization* [74], *electrohydrodynamic* (*EHD*) *atomization*, or *liquid atomization by electric means* [69]. Electrospraying was discovered in as early as 1750 when Abbé Jean-Antoine Nollet, an esteemed French experimental phycisist and clergyman, experimented with electrospraying of water and various liquors, and reported his observations [75,76]. As the story goes, he noticed that if a person was to cut himself while being electrified by a high-voltage generator, he would not bleed normally. Instead, blood would spray from the wound (due to electrical forces) [62]. First modern scientific studies on electrospraying were conducted in 1915 by J. Zeleny [77,78]. In 1964, the physics of electrospraying were established by G. I. Taylor [79].

2.2.1. Principles of Electrospraying Apparatus

In Figure 2, a simple electrospraying apparatus is shown schematically. Liquid is driven at a controlled volume flow rate Q through a conducting capillary, typically of an inner diameter d_i of 0.1–1 mm. The capillary is kept at a positive or negative high potential and thus doubles as a high voltage electrode. A controlled voltage U between the electrospraying nozzle and a nearby ground electrode (extractor) generates an electric field which powers the

electrospraying process – charge is induced to the tip of the liquid column outside the nozzle. Due to electrical forces overcoming the surface tension of the liquid, a droplet detaches directly from the meniscus, or a jet elongates from the meniscus and promptly disintegrates into droplets. In sustained electrospraying, a steady liquid flow from the capillary replenishes the meniscus, and the cycle repeats at a high frequency, or a continuous jet is retained. The electrosprayed droplets are induction charged, sharing the sign of the electrospraying electrode. Thus, the electrosprayed droplets accelerate in the cylindrically symmetric external electric field. At very high droplet formation frequencies, the droplets are self-dispersing due to mutual Coulombic repulsion. In the electrospraying process, the total surface area of the liquid increases as bulk liquid is disintegrated into droplets by the electric field. Energy drawn from the electric field is therefore converted to liquid specific energy related to its surface area; kinetic energy and potential energy of the charged droplets; and heat [62,80].

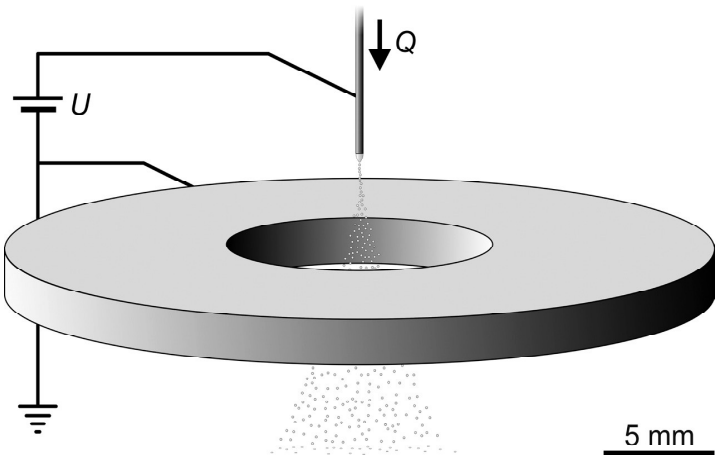

Figure 2. Schematic of a basic electrospraying device. For the shown dimensions, the liquid flow rate Q for a single nozzle is typically of the order of 0.1–1 ml/h and the electrospraying voltage U up to several kilovolts, depending on the electrosprayed liquid properties and the electrospraying mode. The droplet size $\bar{d}$ distribution greatly depends on the electrospraying parameters (Chapter 2.2.2) and varies across different spraying modes.

For the electrospraying geometry of Figure 2, an open extractor electrode centered at the symmetry axis allows for passage of the electrosprayed droplets. The electric field uniformity can be controlled by leading the capillary through

a guard plate (not shown in Figure 2), or a sleeve kept in reduced potential [81,82]. The electric field is further shaped by the extractor electrode and the electrosprayed droplets themselves. Droplet trajectories in the system are determined dynamically by the electric field, gravity, ambient gas flow and pressure p; as well as the droplet charge q, size d, and mass m. In basic applications, for example in production of micro- or nanoparticles via electrospraying, droplets are ordinarily neutralized post extraction (Chapter 2.2.6), and collected on a grounded collector electrode (not shown in Figure 2) below the extractor electrode [10,83,84]. The distance to the collector determines the air time of electrosprayed droplets, which in addition to ambient gas flow, pressure p, and temperature T is important for controlling the degree of excess solvent evaporation from the droplets en route to the collector.

The electrosprayed liquid can be deployed to an electric field in various ways. In addition to the electrostatic pressure, liquid flow to the electric field can be driven by hydrostatic pressure, gravity, capillary pressure, or a centrifugal force [85]. The shape of the interface (point, line or surface) between the liquid body and the external electric field is essential in establishing the atomization geometry. For axial electrospraying from a point source, the liquid is commonly deployed using a capillary nozzle as depicted in Figure 2 [9,13,69,70,86,87]. It is also possible to drive the liquid through a simple hole in the container holding the liquid [88,89]. The liquid can alternatively flow on the outer surface of a wettable, positively curved solid surface, where the external electric field intensifies towards the tip [90–92]. Point sources such as these can be arranged into arrays, with shared or separate liquid reservoirs, in order to increase the total electrospray yield and robustness [89,91,93–102]. Alternative ways to scale up the process include nozzle geometry modification, for instance by using an extender cap [103]; or electrospraying radially from a line source, such as the edge of a plate [104], or a rotating disc [105,106]. A porous foam cylinder (or a similar network of edges) can effectively be utilized as an array of line sources [62]. Liquid-in-liquid electrospraying systems have been deployed as well, where the dynamical effect of an insulating surrounding liquid of low viscosity η is neglectable on the electrospray [107]. In such systems, the atomized liquid can be driven through a large area membrane filter for a scaled up yield [108,109]. Finally, electrostatic atomization can take place directly from a free large area liquid surface [110].

2.2.2. Electrospraying Mode Characteristics

Electrostatic atomization can be conducted in different modes, as determined by the *electrospraying parameters* such as liquid properties (conductivity K, density ρ, viscosity η, surface tension γ); liquid flow rate Q; electric field strength E at the liquid surface, which in turn is influenced by the atomization geometry and voltage U; other external forces acting on the liquid surface, such as gravity or centrifugal forces; as well as atmospheric gas composition, humidity, flow velocity, pressure p, and temperature T [62,70,71,105,111–116]. As many as over ten different spraying modes can be identified, characterized by the shape and stability of the liquid meniscus, presence and permanence of continuous jets, rate of droplet formation, as well as electrospraying current characteristics [9,69,70,111,112,114–117]. The size and charge distributions of atomized droplets depend primarily on the spraying mode, and secondarily on the atomization parameters within that mode [70,74,111,112,116,118].

With no applied voltage ($|U| = 0$) in an electrospraying device of a fixed geometry (*e.g.* that of Figure 2), operated at constant T and p on Earth's surface with the gravity field aligned to the electrospraying axis, liquid flowing at a rate $Q > 0$ accumulates to a drop that hangs outside the capillary (Figure 3a). Assuming that evaporation rate W from the hanging drop remains lower than Q, the drop grows periodically to a critical size, above which the drop weight surpasses the surface tension that binds the drop to both the capillary and the liquid column inside the capillary. The essentially neutral drop is then detached from the capillary due to gravity, and accelerated in the gravity field.

At zero gravity and low liquid momentum, the capillary does not drip liquid if no other force to drive the liquid is present. Instead, the liquid wets the capillary exterior surface, and proceeds to gradually engulf the device up to a balance point, where total evaporation $W = Q$.

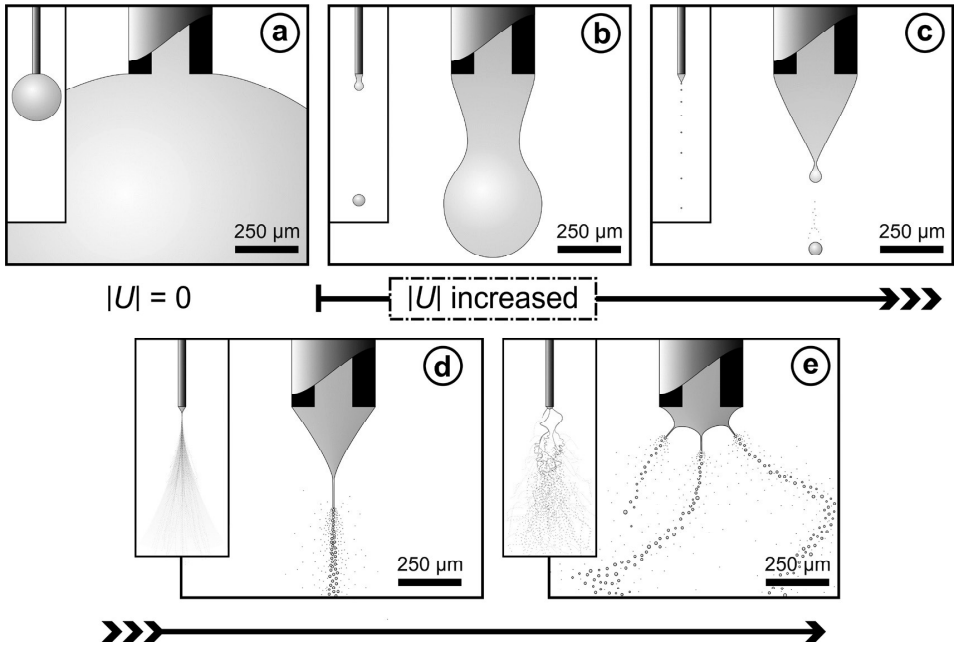

Figure 3. Characteristics of the liquid meniscus, jet, and sprayed droplets for selected electrostatic atomization modes, shown schematically: a) no electrification (reference), b) dripping mode, c) microdripping mode, d) cone-jet mode, and e) multi-jet mode. The atomization voltage $|U|$ is increased through figures a–e, with all other electrospraying parameters kept constant. These and other electrospraying modes are sketched, imaged and described extensively in literature [12,70,71,81,111,112,116,119,120].

2.2.2.1. Dripping and Microdripping Modes

With a low voltage $|U|$ applied, the surface of the liquid protruding from the capillary is charged by induced charge separation, and Coulombic forces act on the charged surface of the liquid meniscus, adding to the effect of gravitational force exerted on the liquid. As depicted in Figure 3b, with $|U| > 0$, droplets still detach one by one, but do so at an increased rate in addition to being both smaller and charged by induction, as compared to scenario of Figure 3a. The liquid meniscus contracts and is swiftly replenished by new liquid after each droplet detachment. Detached droplets are then accelerated by the electric field, which quickly becomes the dominant force acting on the droplets in between the electrodes as $|U|$ is increased. With no radial repulsive forces from neighboring droplets, each droplet follows roughly the same trajectory. This simple form of electrospraying is known as the *dripping* mode, or descriptively

as *field-enhanced dripping*. In this mode, with increasing $|U|$, the dripping frequency increases (up to hundreds of Hz), the electrosprayed droplets get smaller and the droplet specific charge q/m increases [62,69,70].

At a sufficiently high $|U|$, and low Q, it is possible, at least for droplets of liquids such that $K < 10^{-2}$ μS/cm, to become smaller than the inner diameter of the nozzle ($d < d_i$) while the electrospray remains in the pulsating regime [69,70,111]. Such small droplets can form at frequencies of up to tens of kHz, and the liquid meniscus no longer contracts between droplet detachments [69,70,111]. Below this arbitrary droplet size limit, the electrospray is said to transition into *microdripping* mode (Figure 3c) [69,70,111].

Droplets electrosprayed in dripping or microdripping mode are quite consistent in size, with median droplet size typically in the range of a few μm to about 1 mm [70,111]. Following each event of electrospraying a main droplet, several magnitudes smaller and highly charged satellite droplets are ejected from both the meniscus and the main droplet due to vibrations and surface instabilities of the liquid objects. Satellite droplets move slowly, evaporate quickly and do not contribute significantly to the volume of electrosprayed liquid. However, satellite droplets are capable of carrying a significant portion of the electrosprayed charge (see Chapter 2.2.3) [121–123].

Dripping and microdripping modes of electrospraying can be used for controlled deposition of microdroplets [124,125] – for instance microscale EHD inkjet printing in which droplet detachment frequency can be regulated by using pulsating voltage (*droplet on demand*) [126,127]. These modes have also been used in microencapsulation of biotic or other type of materials [128,129].

2.2.2.2. Cone-Jet Mode

The most important electrospraying mode is the *cone-jet mode* (CJM), as judged by the amount of research and applications associated with it [9,10,118,130–138,13,62,71,83,84,86,91,113]. The (stable) CJM is characterized by the steady axisymmetrical conical shape assumed by the liquid meniscus, which in this mode is often dubbed the *Taylor cone* [71,90,111,132,138]. The Taylor cone can be straight-sided, concave or convex depending on the polarity and magnitude of U, the electrospraying geometry, and liquid properties [111]. As depicted in Figure 3d, in CJM a fine, stable, and continuous liquid jet is ejected from the apex of the Taylor cone. Forces acting on the highly charged surface of the jet cause varicose instabilities due to which the jet quickly

disintegrates into very small (typically $d = 0.1–100$ µm) main droplets of a remarkably narrow size distribution, accompanied by a host of much finer satellite droplets; all of which are charged by induction [9,74,83,112,136,138,139]. The main droplets form at a very high frequency (from a few kHz up to several MHz) [70,118], and constitute nearly the entirety of the electrosprayed liquid volume [71,132,136,140]. The thusly dense jet disperses due to mutual Coulombic repulsion of the charged droplets [141,142]. As with dripping modes, the charge carried by satellite droplets can be relevant, however [140].

The CJM is initiated for applicable liquids in suitable conditions (details discussed in Chapter 2.2.4) when $|U|$ is increased from the (micro)dripping mode regime to the CJM onset voltage $|U_c|$ [71,86,111,112]. Transition to the CJM can be very distinct in some cases, whereas in others, an intermediate pulsating mode may emerge amidst the transition from dripping mode to a stable CJM (Chapter 2.2.2.3). As the electrospray enters CJM, the liquid meniscus assumes the stable Taylor cone form, and both the atomization current I and droplet frequency increase abruptly [83,112,143,144]. In CJM, the measured I for a single Taylor cone is typically in the order of 10–100 nA [71,144,145]. As $|U|$ is increased within the CJM regime, the Taylor cone remains stable but contracts axially. Simultaneously, the electrosprayed droplet size decreases and droplet charge increases, albeit to a comparatively insignificant degree (Chapter 2.2.4). The CJM voltage regime is affected by a weak hysteresis effect – once initiated, CJM is maintained even if $|U|$ is decreased slightly below the original onset level $|U_c|$ [71,131,136,146]. Additional control to the electrosprayed liquid volume can be gained by single-event electrospraying, utilizing very low flow rates and pulsed voltages with a stepping high enough to bypass the hysteresis effect [147].

Many applications have been found to benefit from the bottom-up miniaturization among other useful properties that accompany electrostatic atomization in CJM. The technique can be used for the production of micro- and nanoparticles as small as a few nanometers in size [10,12,136,139,148,149], including particles composed of pharmaceutical materials for the purpose of preparing or manufacturing drug delivery systems (see also Chapters 2.2.5 and 2.4) [83,84,134,150–154]. Other biomedical applications include *e.g.* a handheld electrospray gun [137]. In EHD printing applications, high resolution patterns down to tens of nanometers in size can be achieved [155,156]. Painting similarly benefits from the attainable fine and uniform

pigment coatings [10,86,157,158]. In crop spraying, the sprayed fine and charged droplets spread effectively on the surfaces of plants and pest, reducing the amount of pesticide or herbicide necessary for the desired effect [62,159,160]. CJM electrospraying is being utilized in nanotechnology for thin-film deposition with layer thickness down to the nanoscale [161,162]. By layer-by-layer deposition (*electrospray forming*), composite bulk materials can be produced [143,163–165]. The CJM is the most efficient mode for ion production [116], and therefore the CJM ionization is utilized for mass spectrometry [166], and miniaturized spacecraft propulsion technology [91,167]. Quenching of a liquid-metal Taylor cone has been proposed for regeneration of electron field emission cathode tips in spacecraft neutralizers [68]. Encapsulation by electrospraying in CJM in order to produce micro- or nanosized capsules will be discussed in Chapter 2.3 (Electroencapsulation).

2.2.2.3. Other Modes

In the transition voltage regime between dripping mode and CJM, a number of intermediate pulsating modes may be observed depending on the electrospraying parameters. These modes include the *spindle mode* (or *burst mode*), in which the meniscus ejects elongated chunks of liquid that disintegrate into comparatively large droplets of wide size distribution [69,111,116]; the *multi-spindle mode* [111]; the *intermittent* or *pulsed cone-jet mode*, which produces a non-continuously operating CJM [69,70,112,116]; the *oscillating jet mode* [111]; and the *precession mode* [168]. In the last two modes, the jet oscillates in a plane or rotates around the electrospraying axis, respectively. As a result of these instabilities, the droplets produced in oscillating or precession jet modes are not as fine or monodisperse as in CJM [111].

As $|U|$ is increased sufficiently in the CJM regime, kink instabilities and multi-jet instabilities are introduced to the apex of the Taylor cone in addition to the varicose instabilities which are always present in CJM. As a result, different series of mode transitions may be induced to the electrospray, depending on the atomization parameters. Firstly, with increasing $|U|$ the jet may become skewed and unstable (*e.g.* whipping) while remaining continuous [111], before eventually entering a *multi-jet mode* (Figure 3e) with up to 8 jets protruding from the meniscus [111,112,157,169]. From the multi-jet mode, especially in low pressure conditions, the electrospray may gradually enter *rim emission mode* – a mode similar to the multi-jet mode but without an

observable meniscus. Eventually with increasing $|U|$, the electric field strength becomes sufficient for atmospheric breakdown [69,170]. Instead of multi-jet mode and rim emission, it is possible to experience a transition from CJM to a pulsating, low frequency *droplet ejection mode* as $|U|$ is increased, especially in atmospheric pressures and for liquids of high γ [69,170]. Moreover, the occurrence of a continuous corona breakdown while within the CJM regime may lead to a transition to the space charge controlled regime of the Taylor cone, considered to be a separate *Delft aerosol generator* (DAG) sub-mode, or *corona-assisted cone-jet mode*. The poorly understood DAG mode is similar to the CJM, but requires a stabilizing corona discharge, yields an higher droplet generation frequency (on the order of 100 MHz), and thus results in extremely small droplets being generated (ca. 1 μm) [69,138,171]. As an alternate transition path, even at voltages $|U|$ below the CJM regime, the electrospray can enter the *simple-jet mode* when Q is sufficiently high [69]. The critical value of Q for this mode is decreased with increasing $|U|$ [69,112]. Eventually, as $|U|$ is increased within the simple-jet mode, it is possible to trigger a *ramified jet mode* (*cone-ramified jet mode*) [112].

As compared to the CJM, the discussed higher modes and transition modes of atomization display a larger droplet size, wider droplet size and charge distributions, and irregular jet behavior (with the exception of DAG mode). The practical uses of these modes are therefore relatively scarce, and not considered further here.

2.2.3. Droplet Charge

At electrostatic conditions, the net charge of an isolated droplet is uniformly distributed across its surface. Consequently, an electrostatic outward pressure is exerted on the droplet surface due to repulsive Coulombic forces. At the same time, the droplet is contracted and held together by an inward pressure due to the liquid surface tension. The droplet becomes unstable if its charge q is increased to the limit where these opposing forces are balanced. In 1882, Lord Rayleigh derived stability conditions for a slightly deformed, charged droplet of radius r and liquid surface tension γ [172]. He predicted that at the *Rayleigh limit* droplet charge

$$q_{\mathrm{R}} = 8\pi\sqrt{\varepsilon_0 \gamma r^3} \tag{4}$$

or above, the droplet is no longer able to recover its spherical form, *i.e.* the droplet is unstable (*cf.* Chapter 2.2.5) [172]. Division of Equation 4 by droplet mass $m = 4\pi r^3\rho/3$ yields the droplet charge to mass ratio limit

$$\frac{q_R}{m} = \frac{6}{\rho}\sqrt{\frac{\varepsilon_0\gamma}{r^3}}, \quad (5)$$

where ρ is droplet density.

In experiments by various groups since Rayleigh's work, electrosprayed or otherwise electrified microdroplets have been consistently observed to carry at most a charge close to q_R or less [71,122,173,174]. The measured maximum value of the ratio $|q|/q_R$ has frequently been reported to reside in the range of 0.7–0.8 for droplets electrosprayed particularly in CJM [74,118,121,140]. In some cases involving for example low atmospheric pressures, high temperatures or humidities, or a liquid of high γ (*e.g.* water, $\gamma = 73$ mN/m [175]), the droplet charge may be limited by the breakdown strength of air instead of droplet stability, and a corona discharge occurs before the Rayleigh limit charge is reached [62,121,176]. Furthermore, electron emission can be expected to occur when the electric field strength at the droplet surface $E_s = q/4\pi\varepsilon_0 r^2 \geq 9.9 \times 10^7$ V/m [177]. By substituting q with q_R from Equation 4, it is seen that electron emission could in principle limit the droplet charge when the condition $\gamma/r \geq 2.2 \times 10^4$ N/m^2 is fulfilled.

2.2.4. Properties of Electrospraying in Cone-jet Mode

The forces acting on the surface of the Taylor cone in stable CJM are outlined in the force diagram of Figure 4. The principal forces driving the liquid are the *electrostatic force* $\boldsymbol{F}_{en}$ and *electric tangential force* $\boldsymbol{F}_{et}$ (*normal* and *tangential electric stresses*), acting on the induced surface charge (ions); and the *polarization force* $\boldsymbol{F}_{\varepsilon}$ (*electric polarization stress*), acting on polarized charge. The resistant forces are composed of *surface tension* $\boldsymbol{F}_{\gamma}$, and *net viscous force* $\boldsymbol{F}_{\eta}$ (*viscous stresses*), which depend on the corresponding liquid properties γ and η [9,80,111,132]. The forces acting on the Taylor cone liquid are often each considered in terms of unit force per volume (force density). The role of gravity $\rho\boldsymbol{g}$ as an additional driving, resistant, or skewing force density is determined by the alignment of the Taylor cone in relation to $\boldsymbol{g}$. In Figure 4, gravity contributes to driving the liquid. The liquid acceleration $\dot{\boldsymbol{v}}$ at any point in the cone surface is obtained from $\dot{\boldsymbol{v}} = \partial \sum \boldsymbol{F}_i / \rho \partial V$, where

$\partial\Sigma \boldsymbol{F}_i/\partial V = \partial(\boldsymbol{F}_{en} + \boldsymbol{F}_{et} + \boldsymbol{F}_\varepsilon + \boldsymbol{F}_\gamma + \boldsymbol{F}_\eta)/\partial V + \rho \boldsymbol{g}$ is the sum of force densities, and V is volume. As a note, in certain derivations, the most convenient choice can be to analyze the Taylor cone in a frame of reference that accelerates with the liquid. To compensate, liquid inertia can be treated as an additional resistant *inertial force* $\boldsymbol{F}_I$, with force density $\partial \boldsymbol{F}_I/\partial V = -\rho \dot{\boldsymbol{v}}$, for the purpose of obtaining a nominal force equilibrium $\boldsymbol{F}_I + \Sigma \boldsymbol{F}_j = 0$ in accordance to the D'Alembert's principle of inertial forces [9,80].

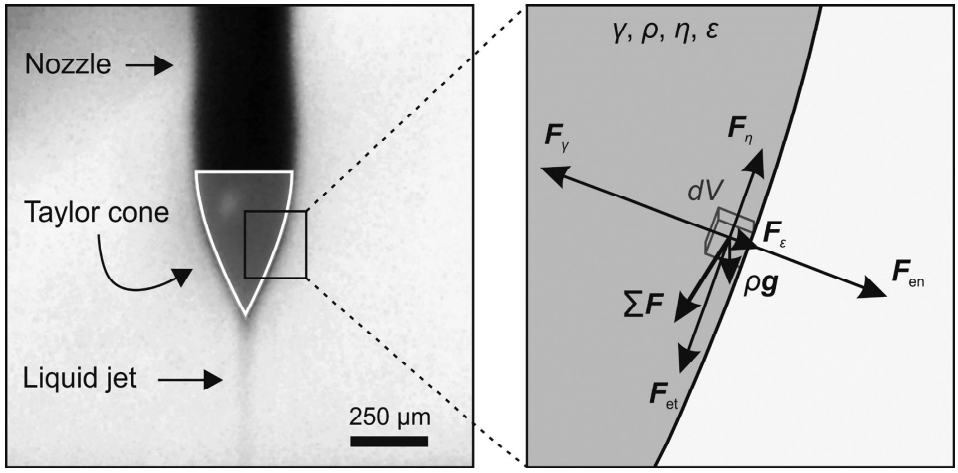

Figure 4. Left: Photograph of NaI-doped glycerol electrosprayed in CJM using a stainless steel nozzle (d_i = 0.15 mm, d_o = 0.30 mm, Q = 0.50 ml/h, U = −3.75 kV, C_{NaI} = 0.50 mg/ml, K = 0.7 µS/cm, air atmosphere, T = 23°C, p = 1.0 bar, RH = 20%). Right: Outlined force diagram of a liquid volume dV in the surface of a stable Taylor cone, with $\Sigma \boldsymbol{F}$ showing the force sum. Approximate directions are given for $\boldsymbol{F}_\varepsilon$ and $\boldsymbol{F}_\eta$. For clarity, force magnitudes are not drawn in exact proportions. The frame of reference is fixed to the Taylor cone position.

Forces $\boldsymbol{F}_{en}$ and $\boldsymbol{F}_{et}$ that act on an ion at point $\boldsymbol{r}$ in the liquid surface are consequence of the electric field $\boldsymbol{E}_s(\boldsymbol{r})$ at the liquid surface (Equation 2). $\boldsymbol{E}_s(\boldsymbol{r})$ depends on the electrospraying geometry and potential; induced charge distribution elsewhere in the Taylor cone surface; as well as the charge and image charge distributions due to electrosprayed droplets in the surrounding air [111,132]. The net force $\Sigma \boldsymbol{F}_i$ acting on the liquid surface may require the cone to assume various shapes depending on the electrospraying parameters [111]. As in the example of Figure 4, the apex usually forms an underlying angle which is close to the predicted Taylor angle of 49.3°, but for example a

high η can result in other stable values [69,86,161,178,179]. The Taylor cone is a very dynamic system – on its surface, standing waves have been observed, and can be linked to the jet varicose instabilities as well as oscillations or perturbations in electrospraying current [180].

In both theoretical and practical CJM considerations, the characteristic flow rate Q_0, characteristic current I_0, and characteristic jet diameter d_0 are useful abstract quantities in describing the properties of the Taylor cone and the electrosprayed droplets [74,145]. These characteristic quantities are defined as

$$Q_0 = \gamma\epsilon_0/\rho K \tag{6}$$

$$I_0 = \gamma(\epsilon_0/\rho)^{1/2} \tag{7}$$

$$d_0 = (\gamma\epsilon_0^2/\rho K^2)^{1/3}. \tag{8}$$

As an example for ethanol (relative permittivity $\varepsilon_r = 24.3$, $\gamma = 22.8$ mN/m, $\rho = 0.789$ g/cm^3, and 1.4×10^{-3} µS/cm ≤ K ≤ 3 µS/cm [69,168,175,181–183]), Equations 6–8 yield for the maximum K value: $Q_0 = 3.1$ µl/h, $I_0 = 2.4$ nA, and $d_0 = 0.29$ µm.

The *EHD Reynolds number* (or *viscous dimensionless parameter*) δ_η is defined as the ratio of the characteristic axial bulk liquid velocity Q_0/d_0^2 and the radial perturbation propagation velocity by viscous diffusion in the liquid jet $\eta/\rho d_0$ [74,80]:

$$\delta_\eta = \rho Q_0/\eta d_0. \tag{9}$$

For ethanol ($\eta = 1.20$ mPas [183]), using $K = 3$ µS/cm, $\delta_\eta = 1.91$ is obtained from Equation 9.

The Taylor cone *natural liquid flow rate* is the minimum liquid flow rate Q_{min} required for stable CJM operation, and depends on the nature of the restrictive force which is determined by the liquid properties. It has been estimated that if $\varepsilon_r\delta_\eta > 1$, the cone-jet becomes unstable when $Q < Q_{min} \approx \varepsilon_r Q_0$, where Q_0 and δ_η are obtained from Equations 6 and 9, respectively, due to a negative polarization force $\boldsymbol{F}_\varepsilon$ in the cone-jet region, or charge separation [80,119,184]. However, experimental data indicates that the minimum flow rate can be closer to $Q_{min} \approx 0.01 \times \varepsilon_r Q_0$ in some cases, which is a result of deviation between the assumed and measured values of the force ratio $|\boldsymbol{F}_\varepsilon|/|\boldsymbol{F}_{en}|$ [80]. For liquids of $\varepsilon_r\delta_\eta < 1$, viscous forces cause a loss of stability below $Q_{min} \approx Q_0/\delta_\eta$ [80,183]. The estimate Q_{min} is susceptible to variations of K, as reported values of K may span several orders of magnitude due to variations in solvent purity

or other measurement conditions. This is noticeable from the presented range of K literature values of ethanol, for example [69,168,181,182]. Within this K range of ethanol, the estimate $Q_{min} = \varepsilon_r Q_0 = 0.07$ ml/h (obtained for $K = 3$ μS/cm [168]) reasonably covers the reported experimentally operated Q ranges of ethanol in CJM [81,144]. Generally, K increases rapidly as solutes or impurities are introduced to a poorly conducting liquid. Therefore, the approximation method for the limit Q_{min} remains meaningful in the lower conductivity range ($K << 1$ μS/cm) only if K is carefully measured for electrospraying formulations that consist of such liquids.

2.2.4.1. Liquid prerequisites

In determining whether a liquid is electrosprayable, arguably the most important liquid properties are electrical conductivity K and surface tension γ [71,185]. Together with the density ρ, viscosity η, and relative permittivity ε_r of the liquid, these properties determine the feasibility of the liquid for electrospraying, and influence the properties of electrosprayed droplets, as discussed throughout Chapters 2.2.2–4 [9,69]. In general, explicit limits for the liquid properties cannot be determined because of mutual dependencies. Normally, the parameters cannot be adjusted independently. For example, the conductivity K of many liquids can be enhanced by increasing the solution salinity [94,130,186]. Furthermore, γ can be decreased by introducing surfactants to the liquid [187]. However, such additives usually influence other liquid properties to some degree, as well.

For a liquid to be electrosprayable in CJM, Gañán-Calvo *et. al.* propose that charge must be dynamically distributed to a thin layer at the surface of the Taylor cone [74]. As approximated by the authors, for the bulk of the Taylor cone to remain quasi-neutral, the condition

$$K \gg 4\epsilon Q / L_0 R_0^2 \tag{10}$$

must apply, where L_0 and R_0 are the characteristic length and radius of the jet, respectively; and $\varepsilon = \varepsilon_r \varepsilon_0$ is the liquid permittivity [74]. As an example, for typical electrospraying conditions of paraffin ($Q = 4$ ml/h, $L_0 = 1$ mm, and $R_0 = 30$ μm), the authors obtained the experimentally verifiable coarse condition of $K >> 1 \times 10^{-3}$ μS/cm from Equation 10 [74].

Directly observed estimates of the minimum K requirements for stable CJM mode electrospraying in the air vary between 10^{-4}–10^{-7} μS/cm for different experimental conditions [71]. On the other hand, CJM has been reported for

values of K as high as 10^3 μS/cm when electrospraying a liquid of low γ, and jet diameters are considered to be of the order of 10 nm for liquids of K in the order of 10^4 μS/cm [71,119]. The CJM regime generally shifts toward lower Q with increasing K (*cf.* Equation 6) [71]. Some authors have proposed that no upper limit of K for CJM exists *per se*, but instead the produced droplets become so small that detecting them by light scattering becomes increasingly difficult [146].

If γ is high enough, emergence of a corona discharge at the tip of the liquid meniscus becomes probable, which destabilizes or prevents CJM electrospraying in air [71,82,171]. A maximum value of as low as $\gamma \leq 50$ mN/m has been reported for stable CJM electrospraying [146]. On the other hand, accounts of successful experiments of electrospraying glycerol ($\gamma = 63$ mN/m), and even water ($\gamma = 73$ mN/m) in CJM set the maximum γ limit higher [69,78,87,111,175]. The lowest observed limit values of γ are likely consequence of unsuitable electrospraying parameter combinations, influenced decisively by the high γ. When the electric field strength E_s at the surface of the liquid meniscus apex surpasses the breakdown strength of the surrounding gas, a Corona discharge is triggered at the liquid apex. The occurrence of such an event naturally depends not only on γ, but on various parameters. The electrospraying geometry crucially affects the susceptibility of E_s to the size or shape variations of the meniscus, such as contraction, elongation, or varicose and kink perturbations. The nozzle diameters d_i and d_o together with the liquid wetting properties determine the width of the meniscus base, which affects the meniscus length. Therefore, d_i and d_o influence the distance of the liquid apex from the counter electrode, and thus E_s at the liquid apex. With increasing K, charge conducts to the liquid surface at a higher rate, and the jet is driven increasingly more by normal forces as opposed to tangential stress, which leads to more frequent and forceful surface disruptions. Consequently, local variations of E_s develop, which effectively decreases the Corona discharge threshold value of γ [10,82]. An often used methodology to circumvent Corona discharging is smoothing of sharp edges at the nozzle tip and application of a downward flow of insulating sheath gas, such as CO_2, around the sharp liquid apex to cover it [82,115,171,186,188].

Many common solvents and oils, such as ethanol, chloroform, ethylene glycol, acetone, and glycerol are readily electrosprayable in CJM over a relatively wide range of electrospraying parameters [78,111,133]. Other liquids, such as various vegetable oils, may require additives to adjust the liquid

properties, such as K or γ [74,189]. However, establishing a stable CJM on water is more demanding, because the high γ and high K (reported K values include $K_{\text{tap water}}$ = 300 μS/cm, $K_{\text{deionized water}}$ = 3.3 μS/cm, $K_{\text{distilled water}}$ = 1.1 μS/cm) can easily trigger a Corona discharge [71,82,111,146,183,186,190,191]. Due to these and other properties of water, such as its high polarity and abundance of dissociated ions (Chapter 2.1.4.4), the sign of the electrospraying potential U significantly affects the obtainable electrospraying modes and their respective stable voltage regimes. The CJM is obtainable for water at positive polarity, but the voltage regime tends to be narrow [51,82,111,190,192]. A colloidal suspension can be electrosprayable, if its medium consists of an electrosprayable liquid [9,12,193].

Density ρ is not an important limiting factor to CJM electrosprayability on its own at atmospheric pressure – superfluid liquid helium (ρ = 0.147 g/cm^3 at T = 2.2 K) and liquid metals (*e.g.* Au, ρ = 19.3 g/cm^3) alike are applicable for the technique [10,92,110,194,195]. Similarly, liquids of relative permittivity in the range of at least $1.9 \leq \varepsilon_r \leq 182$ have been found to be electrosprayable in CJM [74,107,191]. Therefore, for the majority of liquids, ε_r does not single-handedly constitute an obstacle to electrosprayability.

In suitable conditions, a jet of a considerably high η liquid protruding from the Taylor cone does not disintegrate into droplets, *i.e.* the Taylor cone no longer produces an electrospray. A sufficiently high η can be obtained for example by dissolving a long-chained polymer in a high concentration to the liquid. *Electrospinning* technique exploits this phenomenon to produce extremely thin (5–1000 nm thickness) polymer threads and fibers, in contrast to the ultrafine droplets and particles produced by the closely related technique of electrospraying [73,178,196–206].

2.2.4.2. Droplet Size and Atomization Current

As discussed in Chapter 2.2.2.2, the main droplets electrosprayed in CJM are very monodisperse, but never absolutely so. In addition, the main droplets are accompanied by satellite droplets. Therefore, the electrosprayed droplet size distribution cannot be described by a delta distribution. The droplet volume median diameter d_{med} is, however, a good measure of the most probable size of droplets electrosprayed in CJM [71]. For clarity, in this work the meaning of droplet size d in the context of CJM electrospraying is taken to be d_{med}. Consequently, these quantities will be used interchangeably where no danger of confusion exists.

Controlling the droplet size in CJM electrospraying is important, since various types of applications rely on it. In CJM, a reasonable estimate of the droplet size d can be acquired from an equation of the form

$$d = \alpha \frac{\rho^{\nu} \epsilon_0^{\xi}}{\gamma^{\nu} K^{\xi}} Q^{\chi}, \qquad (11)$$

where $\alpha = \alpha(\varepsilon_r)$ is unitless, and the values of the exponents vary by electrospraying conditions and authors as: $0 \leq \nu \leq 1/6$; $1/6 \leq \xi \leq 1/3$; and $1/3 \leq \chi \leq 1/2$ [9,74,118,145,207,208]. In Equation 11, on average the most influential electrospraying parameters are the liquid flow rate Q and conductivity K, followed by surface tension γ and density ρ. The droplet size d also increases to an extent with the capillary inner diameter d_i and with liquid viscosity η, despite these parameters being absent in Equation 11 [9,74]. Liquids of high η require more energy to disperse into droplets, as compared to liquids of low η. It follows that droplets of a higher η liquid are generated at a lower frequency, which results in larger droplets [209]. The effect of $|U|$ on droplet size (and charge) within the CJM regime remains comparatively quite insignificant, since the operational voltage regime of the stable CJM is relatively narrow, especially for liquids of high K [71,74,112,136]. Jet emission in CJM is primarily dependent on the liquid properties – the electrospraying geometry is not relevant, as long as the required CJM threshold electric field strength is achieved, and no Corona discharges are generated [80,208]. Gañán-Calvo *et. al.* have solved the scaling laws for d and atomization current I in four different electrospraying liquid parameter subspaces, some of which are introduced and discussed here as examples [74,208]. The electrospraying scaling laws have been found in separate research papers to be accurate for at least liquids of $\varepsilon_r < 31.2$ [184]; and to approach experimental results at high ($80 < \varepsilon_r \leq 180$) permittivity (*cf.* water, $\varepsilon_r = 80.2$ at $T = 20$°C [175,190]) [191].

If the liquid is of sufficiently high η and high K, so that the condition $\delta_\eta (Q/Q_0)^{-1/3} << 1$ is true (cf. Equations 6 and 9), it follows that the liquid axial momentum transmits efficiently throughout the liquid for a flat axial velocity profile, and that the electric current flows in the bulk of the cone [74]. This leads to a $I \sim Q^{1/2}$ scaling law of the atomization current:

$$I/I_0 \sim \left[Q/Q_0 (\epsilon_r - 1)^{1/2}\right]^{1/2}. \qquad (12)$$

The $I \sim Q^{1/2}$ scaling law has been obtained by other authors as well, and is applicable for many common solvents such as ethanol, acetone, and (NaI-

doped) glycerol [74,130,144,145,207,210]. According to experimental results, this scaling law is fairly accurate even for $\delta_\eta(Q/Q_0)^{-1/3} \approx 1$ [74]. For a liquid that obeys the $I \sim Q^{1/2}$ scaling law (Equation 12), the dimensionless droplet (jet) size is proportional to

$$d/d_0 \sim \left[(\epsilon_r - 1)^{1/2} Q/Q_0\right]^{1/3}. \quad (13)$$

Equations 6, 8, and 13 yield the exponents in Equation 11 as $\nu = 0$, and $\xi = \chi = 1/3$:

$$d \sim \left[\frac{(\epsilon_r - 1)^{1/2}\epsilon_0}{K} Q\right]^{1/3}. \quad (14)$$

It is notable in the previous result that the charge per unit mass obeys the proportionality of the Rayleigh limit, $I/Q \sim d^{-3/2}$, as shown equivalently in Equation 5. This assumption has been shown to be valid approximation and is frequently made in CJM electrospraying [71,74,118,133,140]. The same proportionality is valid for liquids of low η and low K, *i.e.* liquids that fulfill the condition $\delta_\eta(Q/Q_0)^{-1/3} >> 1$. The motion of such a liquid is inviscid, an axial distance significantly longer than L_0 is required for the liquid to become thoroughly accelerated. Consequently, the liquid velocity is much greater at the jet surface as compared to the bulk, and the current I consists nearly exclusively of surface charge convection [74]. For best agreement with experimental data for liquids of low η and low K, Gañán-Calvo *et. al.* have concluded that the total electrospraying current $I \sim d_j^{1/2}$, where d_j is the jet diameter [74]. Moreover, a common approximation for liquids of low η is that $d = 1.89 \times d_j$, as for uncharged jets [71,74]. These assumptions yield the $I \sim Q^{1/4}$ scaling law for liquids of low η and low K [74]:

$$I/I_0 \sim (Q/Q_0)^{1/4}. \quad (15)$$

Consequently, the dimensionless droplet (jet) size for liquids that obey the $I \sim Q^{1/4}$ scaling law (Equation 15) is obtained from [74]:

$$d/d_0 = k_d (Q/Q_0)^{1/2}, \quad (16)$$

where k_d is a proportionality constant, to be measured experimentally. Equations 6, 8, and 16 yield the exponents in Equation 11 as $\nu = \xi = 1/6$, and $\chi = 1/2$:

$$d = k_d \left(\frac{\rho\epsilon_0}{\gamma K} Q^3\right)^{1/6}. \quad (17)$$

To obtain intermediate scaling laws, Gañán-Calvo *et. al.* incorporated a dependence of Q on the liquid velocity at the surface of the jet v_s (of the form $v_s \sim Q^{\beta}$, where $0 \leq \beta \leq 1/9$) to the scaling laws derived for liquids of low η and low K (Equations 15–17),. For $\beta = 1/9$, they obtained the $I \sim Q^{1/3}$ scaling law, yielding $d \sim Q^{4/9}$ ($\chi = 4/9$ in Equation 11) with the assumption of droplet charge proportionality to the Rayleigh limit ($q \sim I/Q \sim d^{-3/2}$) [74].

More recently, Gañán-Calvo *et. al.* have specified that as the Taylor cone surface charge has been shown to be in equilibrium, then (similarly to the low η and low K case described previously) the bulk liquid can be considered quasi-neutral for all liquids of large enough electrical mobility, except for the most conductive liquids such as tap water or liquid metals. This is because for sufficiently conductive liquids, a charge double-layer forms to the liquid surface, and its thickness is small in comparison to d_0 except for liquids of very high K [184]. In addition, for most liquids, the liquid velocity profile is reasonably flat to justify the use of a one-dimensional model of the slender jet. Liquid motion in the bulk of the meniscus can be considered irrelevant to the electrospraying mechanism, except for marginally few liquids of very low η and K [184]. In practice, axial momentum has been observed to diffuse rapidly from the liquid surface to the bulk in small jets, even for liquids of very low η, such as hexane or heptane [80,211]. Charge convection can be considered the dominant charge transfer mechanism for these solvents as well, as they conduct poorly [74,181]. A significantly simplified cone-jet model, where $\boldsymbol{F}_\varepsilon$ is found negligible, can be applied for liquids that fall in between these extreme cases. The model yields an effectively universal scaling law of $I \sim Q^{1/2}$, independent of ε_r:

$$I/I_0 = k_I (Q/Q_0)^{1/2}, \quad (18)$$

where k_I is a proportionality constant that depends on the electrospraying geometry, to be measured experimentally. The scaling law was confirmed experimentally using various liquids of $\varepsilon_r \leq 80.2$ (water), with $k_I = 2.6$ measured for the authors' experimental setup [184]. The droplet size scaling law $d \sim Q^{1/2}$ was obtained equivalently to Equations 16 and 17, and confirmed with $k_d = 2.9$ as measured by the authors [184]. In this model, the droplet charge scales as $q \sim d^{-1}$.

The droplet size scaling law $d \sim Q^{1/2}$ of Equations 16 and 17 was also obtained by Hartman *et. al.* for varicose jet break-up regime using experiments and a different derivation, in which a flat liquid velocity profile and thus the $I \sim Q^{1/2}$ scaling law (similar to Equation 18) was assumed [118]. The authors observed in their experiments that as the jet entered the kink (whipping) break-up regime, d scaling transitioned to the $d \sim Q^{1/3}$ dependence, similar to Equations 13 and 14. This scaling law transition was explained by the authors as the droplet charge beginning to scale as a fixed fraction of the Rayleigh limit charge (Equation 4) in the whipping break-up regime, unlike in the varicose break-up regime [118].

In the inertia-electrostatic force regime ($Q > Q_0/\delta_\eta$, $\varepsilon_r\delta_\eta < 1$), where charge convection was assumed to be the dominant charge transfer mechanism, scaling laws $I \sim Q^{1/2}$ (Equation 18) and $d \sim Q^{1/2}$ (Equations 16 and 17) were obtained for $L_0 \leq d_i$, *e.g.* excluding nano-electrosprays [80,208]. In the derivation, volume specific force balance was considered between only the dominant driving and resistant forces – the electrostatic force $\boldsymbol{F}_{es}$ and inertia $\boldsymbol{F}_I$, respectively. The authors note, however, that the electric tangential force $\boldsymbol{F}_{et}$ is also a significant driving force, acting along the length of the jet [80]. Also, viscous forces $\boldsymbol{F}_\eta$ are may not be neglectible for all liquids, even before entering the electrospinning regime [9,74].

2.2.5. Droplet Evaporation and Coulomb Fission

After being ejected from the liquid meniscus, electrosprayed droplets are rapidly accelerated in the external electric field $\boldsymbol{E}$. The velocity $\boldsymbol{v}_i$ of droplet i relative to the surrounding gas is obtained from the force balance

$$\frac{\pi}{6} d_i^3 \rho_\mathrm{d} \dot{\boldsymbol{v}}_i = \frac{\pi}{8} C_D \rho_\mathrm{g} d_i^2 \boldsymbol{v}_i^2 + q_i \boldsymbol{E}(\boldsymbol{r}_i) + \frac{1}{4\pi\epsilon_0} \sum_{i \neq j} \frac{q_i q_j}{r_{ij}^3} \boldsymbol{r}_{ij} + \frac{\pi}{6} d_i^3 (\rho_\mathrm{d} - \rho_\mathrm{g}) \boldsymbol{g}, \quad (19)$$

where C_D is the droplet drag coefficient in the surrounding gas, ρ_g and ρ_d are the respective densities of the surrounding gas and the droplet, d_i and q_i are the droplet diameter and charge, r_i is the vector position of charge q_i, r_{ij} is the vector distance between charges q_i and q_j (*cf.* Equation 1), and $\boldsymbol{g}$ is acceleration due to gravity [141,142]. On the right hand side of Equation 19, the first term is the resistive drag force of the surrounding gas, and the second term is the Coulombic force exerted by the external electric field $\boldsymbol{E}$. The third term includes mutual Coulombic forces between the droplets and image charges induced by the droplets (image force). The last term, consisting of gravity force

and buoyancy, is neglectable for conventional CJM electrospraying conditions, due to the high charge-to-mass ratio of the droplets [62,141,142]. The droplet velocity $\boldsymbol{v}_i$ asymptotically approaches the dynamically changing terminal velocity $\boldsymbol{v}_{t,i}$, obtainable from Equation 19 for the condition $\dot{\boldsymbol{v}}_i = 0$.

For water droplets of 10–100 μm in size, terminal velocity in the absence of electrical forces is of the order of 3–300 mm/s, and is reached (to a degree of 95%) in about 1–100 ms [62,212]. Thus, uncharged water droplets of such small size adjust their velocity to that of the surrounding gas flow almost instantaneously. However, under the brief influence of the extracting electric field, charged droplets electrosprayed in CJM can be observed to reach initial velocities of tens of m/s, as measured a few millimeters away from the Taylor cone [130,213]. The droplets decelerate as the distance from the Taylor cone increases, and $|\boldsymbol{E}|$ decreases. The induced image field once again accelerates the charged droplets (or residual particles) as they approach the collection electrode [142,214]. The time required for electrosprayed droplet i to migrate from the meniscus to the surface of the collector electrode (droplet *air-time*) can be expressed as $t_i = \int \boldsymbol{v}_i \cdot d\boldsymbol{l}_i$, where the droplet trajectory length $l_i = \int d\boldsymbol{l}_i$ depends primarily on the electrospraying geometry.

For droplets composed of a volatile liquid, such as many of the common organic solvents, liquid evaporation takes place during the droplet air-time. In the evaporation process, neutral molecules cross the liquid-gas interface and escape the droplet. Therefore, evaporation does not affect droplet charge, as have been shown experimentally [62,173]. However, the charge to mass ratio q_i/m_i of an evaporating and charged droplet is increased due to its diminishing size. Thus, the droplet eventually reaches the Rayleigh limit charge (Equation 5) and consequently, as discussed in Chapter 2.2.3, becomes unstable. In a state of such instability, the droplet ejects portions of its mass and charge in events of *Coulomb fission*, or *Coulombic explosions* [86,121,140,172,207,215]. Droplets charged nearly to the Rayleigh limit have been in most cases observed to emit jets of extremely fine satellite droplets (d < 100 nm) which are highly charged [62,121–123,140,172,207,215]. In this *fine* Coulomb fission, a transient Taylor cone or liquid meniscus of similar characteristics forms in the surface of the parent droplet [71,140,207]. The ejected satellite droplets significantly deplete the parent droplet of its charge, while carrying away little of its mass [121–123,207]. It is considered possible that a part of the charge expelled in fine Coulomb fission could in certain cases be carried by ions ejected from the droplet by field emission [207]. For liquids that cannot form a Taylor cone, *e.g.*

liquids of very low K, a *rough* Coulomb fission has been observed in some scenarios. In rough fission, the droplet splits into two or several relatively large and stable fragments [173,207]. The fission mode is determined by the droplet size and liquid properties in a way which is not completely understood, although it is possible that analogy to the underlying atomization modes exist to an extent [207].

In CJM electrospraying, ordinarily used electrospraying inter-electrode distances (of the order of 1 m) generally provide sufficient droplet air-time to allow for appreciable evaporation during the droplet transport [62,142]. The evaporation rate is based on liquid selection, and can be further enhanced or controlled to an extent by varying the electrosprayed droplet size d; the liquid flow rate Q, which in part affects the equilibrium partial pressure of the liquid due to evaporation near the electrosprayed droplet jets; the temperature of the electrosprayed liquid; as well as the composition, flow, temperature, and total pressure of the surrounding gas [113,142,216]. With a solute material or dispersed (nano)particles present in droplets of a volatile electrosprayed liquid, evaporation of the liquid from the droplet will leave behind either residual ions [66], or residual solid (agglomerate) particles. The phenomenon is exploited in micro- and nanoparticle production by electrospraying [10,83,195]. Provided that the liquid evaporation is completed before deposition, and that the evaporation rate is moderate so as to not disrupt the formation of residual particles, the solvent evaporation rate does not significantly affect the final size or shape of the deposited residual particles (*relics*). The size of deposited residual particles then depends primarily on the concentration of the nonvolatile solute and/or dispersed components in the electrosprayed liquid; and the size and charge of the electrosprayed droplets [214,217,218]. Residual particles that form during the transport become spherical [214]. However, at very fast evaporation rates, porosity can be induced to the particles [113]. Accordingly, the corresponding electrospraying parameters are used to control the properties of micro- and nanosized thin films and particle powders produced by electrospraying [9,10,142,162,214].

2.2.6. Droplet Neutralization

The induced droplet charge can affect the collection or deposition efficiency of droplets or residual particles positively or negatively, depending on the electrospraying arrangement. For example, droplet or particle charge can be

beneficial for steering their flow in targeted deposition techniques [158,159]. In dry powder production, droplets are often electrically neutralized immediately after being ejected from extraction electric field [113,136,219]. The benefits of such *in situ* neutralization include, most importantly, elimination of Coulomb fission, which is necessary to achieve a consistent residual particle size [10,113,136]. Moreover, neutralization eliminates external Coulombic forces and mutual Coulombic repulsion acting on the droplets and particles. In some setups, this could improve the particle collection efficiency, as well as reduce agglomeration of the deposited particles that could occur due to local surface charge domains in an insulating collection dish or substrate, such as a Petri dish or a nylon filter [13,219–221].

The different neutralization methods utilized in electrostatic atomization include Corona ion source neutralizers (*cf.* Chapter 2.1.4.3) [10,113,138,186,219,222]; radioactive sources such as Po^{210}, Am^{241}, or Cm^{242} for neutralization of small droplets [136,191,223]; X-ray photoionization for neutralization of residual particles [221,224]; or operation of two electrosprays of opposite polarities, with the oppositely charged droplets attracting each other, merging and mutually neutralizing by charge transfer (cf. Chapter 2.3.2.1) [9,225]. The rate of spontaneous aerial discharge (Chapter 2.1.4.4) is generally too low to result in any significant neutralization of a droplet electrosprayed in CJM, with a typical droplet size of 10 nm to 100 µm and air-time of the order of 0.1–100 s.

2.3. Electroencapsulation

A material which is either vulnerable to the surrounding environment, affects its surroundings adversely, or is in a metastable or difficult to handle physical state or form, can be physically confined and chemically isolated from its surroundings by *encapsulating* it in an *envelope* or *matrix* composed of *shell material* [7,226–231]. Encapsulation can render the *payload* (*core material*) mechanically easier to process and chemically inert [7,9]. For example, successfully encapsulating droplets of a liquid dispersion of nanoparticles in solid shell capsules of diameter $D \geq 10$ µm effectively increases the size scale of the handled objects by orders of magnitudes. For purposes of handling, storing, processing, and dosing, the encapsulated payload could then be processed as a dry powder, with the surface properties of the shell material [9,232,233]. An

encapsulated solid may assume a disordered, metastable physical state (*cf.* Chapter 2.4.1) – for example in the form of a molecular, amorphous, or nanocrystalline solid solution or dispersion [7,234,235]. In the spatial confinement of a solid dispersion, the diffusion mobility of the core material molecules is remarkably diminished or suppressed. Consequently, precipitation and crystal growth are subdued or inhibited. Therefore, by encapsulation of the core material into a solid dispersion, its disordered physical state can be stabilized to endure even stressful external conditions over extended periods of time [7,235]. The core material release kinetics and trigger conditions (melting, rupture or dissolution of the shell material, diffusion) are controllable by adjustments of capsule properties such as its size, composition, and structure [7,226,229,230].

Electroencapsulation is a process of encapsulation assisted by electrical forces, *i.e.* by use of electrospraying in CJM [9,236]. Other modes of electrospraying, such as the dripping mode, can be used for electroencapsulation as well, but will not be discussed in this work [128].

2.3.1. Material prerequisites

In electroencapsulation, the core material can be solid, liquid or gaseous. Solid or gaseous payload materials must be dissolved or dispersed to a liquid or colloid formulation, prior to electrospraying. The shell material, in order to form either the capsule envelope or the matrix, and to be electrosprayable in CJM, consists of a liquid or a solid dissolved in a liquid phase [9,12,232,236,237].

The core and shell materials can be introduced to a common electrospraying liquid, or they can be formulated into separate core and shell electrospraying liquids. In correspondence, electroencapsulation can be used for fabrication of two types of micro- and nanocomposite materials: *micro-* or *nanomatrix particles* consisting of a payload (core) material as a uniformly distributed solid solution or solid dispersion in a suitable solid matrix (shell) material; and *core-shell micro-* or *nanocapsules* with a solid, liquid or gaseous core enveloped in a solid (or liquid) shell layer; [9,12,232,236,238–240].

In order for droplets of two species of liquids to successfully form core-shell capsules, the core and shell liquids must be immiscible and mutually wettable. The droplet of higher surface tension liquid is then enveloped by the droplet of lower surface tension liquid upon bringing the two into contact: $\gamma_c > \gamma_s$ [232].

The envelopment can be complete if the capsule does not contact another solid or liquid surface (except for possible gelatinizing or polymerizing baths), and if an adequate volume of shell liquid is present to cover the whole surface of the core droplet. The capsule shell can finally be solidified, either by cooling and subsequent phase transition of the shell material [227]; by chemical reactions such as gelatinization, or polymerization [9,236,239,241]; or, with a suitable polymer dissolved to the shell material, by evaporation of excess solvent [9,236,242].

In general, the highest usable concentrations of any dispersed or dissolved solids can be a limiting factor to the process yield. Excessively high concentrations of dispersed solid materials may promote agglomeration of the dispersed particles in the electrospraying liquid, while solute concentrations approaching the solubility limit in the electrospraying liquid could result in a premature solidification or crystallization of the solute at the electrospraying needle tip. Consequently, the electrospray CJM operation may become instable or intermittent, which eventually risks clogging the electrospraying nozzle [9,113,119,240]. Miscible or dispersed liquid components can be added to the formulations as needed. However, any liquid formulations or their co-extruded combinations to be electrostatically atomized during the electroencapsulation process must meet the requirements for electrospraying in CJM, discussed in Chapter 2.2.4.1 for single-phase liquids.

2.3.2. Electroencapsulation methods

To support extensive use of electroencapsulation in the production of nanostructured solid solution matrix particles as well as micro- and nanocapsules for a diversity of applications, several electroencapsulation methods have been studied [9,12,128,232,236,242]. Different material combinations and liquid formulations allow for experimenting with the creation of versatile micro- and nanocomposite matrix or capsule structures. The range of capsule sizes producible by electrospraying is wide, and capsules as small as 150 nm can be obtained, while retaining a narrow size distribution [240,243]. The electrospraying configurations of some relevant electroencapsulation methods, which utilize either a single electrospraying nozzle or a pair of parallel or coaxial electrospraying nozzles operated in CJM, are depicted schematically in Figures 5a–c and will be briefly discussed in the chapters to follow.

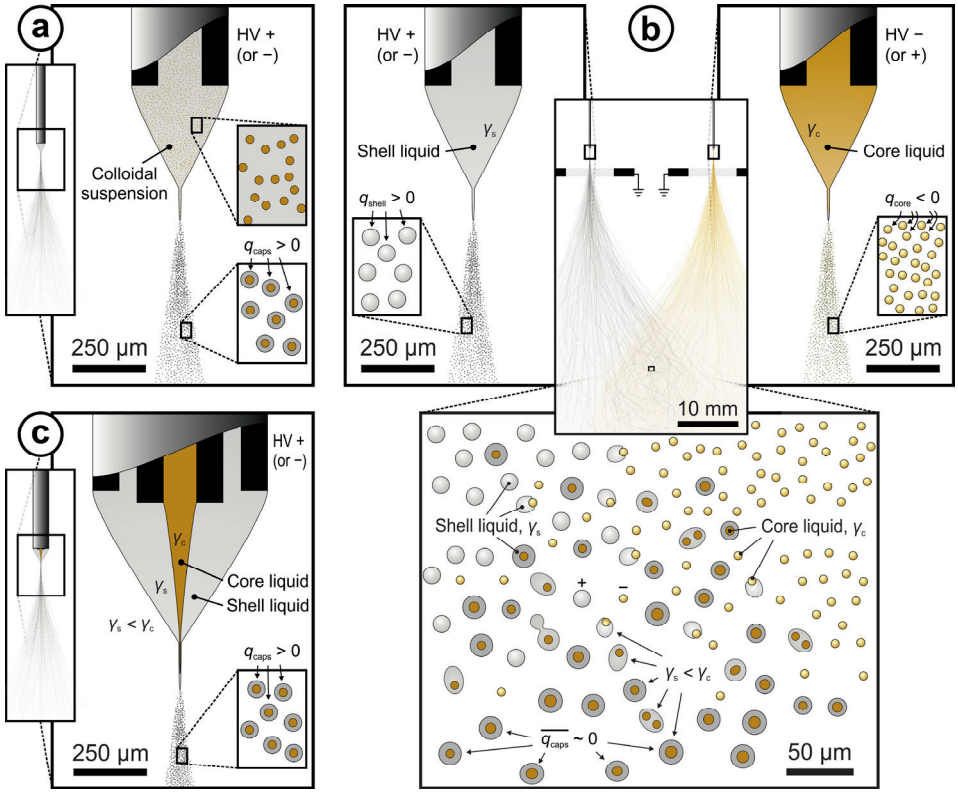

Figure 5. Schematically shown electrospraying configurations for electroencapsulation by the use of a) a single nozzle, b) parallel nozzles, and c) coaxial nozzles operated in CJM. In b), the extractor electrodes are visible.

By selection of the electrospraying configuration and adjustment of the electrospraying parameters (Chapter 2.2.2), a feasible encapsulation efficiency can potentially be achieved together with suitable payload release trigger conditions and release profiles from the produced micro- and nanostructured materials for various applications, while maintaining capsule integrity, stability, and functionality in the desired conditions [153,154,232,237,238,240,243–245]. These properties can be beneficial for instance in food processing, cosmetic industry, and textile industry applications for the addition, protection and controlled release of coloring or active ingredients (*e.g.* flavors, dyes, enzymes, vitamins, or fragrances) [9,227,236,245–247]; in pharmaceutical applications such as targeted delivery and controlled release of drugs, living cells, viruses, or genetic material [128,153,154,219,233,237,240,242,248]; or in controlling the efficiency of insecticide targeting [9,249].

2.3.2.1. Single Nozzle

Electrospraying of a colloidal suspension from a single nozzle in CJM (as shown in Figure 5a), and subsequent solidification (*cf.* Chapter 2.3.1) of the continuous phase (shell liquid) is a relatively uncomplicated electroencapsulation method that can be carried out using the simple electrospraying setup of Figure 2 [219,241,250]. The dispersed phase (suspended payload particles) can be solid, liquid or gaseous. With a sufficiently low concentration of the dispersed material, micro- or nanosized solid capsules carrying a single particle, droplet, or bubble can be produced [9]. Capsules or matrix particles containing multiple dispersed payload particles can be produced by increasing the payload concentration or droplet size.

Similarly, a solute payload material can be electroencapsulated using a single electrospraying nozzle. In such a scenario, the shell material is dissolved along with the payload material in the electrospraying liquid [153,240,244,251,252]. The electrospraying of such a single-phase liquid is comparable in complexity to the electrospraying of a pure solvent (Figure 3d). During the solidification process of the resulting matrix particles, the physical state of the payload material is determined [94,253]. It is possible for the payload material to remain molecular, constituting a solid solution in the matrix [7,94,252]. The payload can also form dispersed nanocrystals or amorphous clusters during the solidification, resulting in a solid dispersion (*cf.* Chapter 2.4.3) [7,94,240,254–256].

Using a single nozzle, the core liquid can be electrosprayed into a gelatinizing shell liquid bath, where the shell layer forms around the core droplets to complete a core-shell structure (*cf.* Chapter 2.3.1) [257].

Capsules or matrix particles produced using the single nozzle method carry a charge of the same polarity as the electrospraying nozzle. Thus, capsule neutralization (*cf.* Chapter 2.2.6) or the use of an oppositely charged collection electrode is required for best collection efficiency.

2.3.2.2. Bi-Polar Parallel Nozzles

In Figure 5b, the electroencapsulation principle using a pair of parallel nozzles kept in high potentials of opposite polarities is shown. For core-shell capsule production, the immiscible core and shell liquids are electrosprayed separately from the nozzles of opposite polarities, and as a result the core and shell droplets are charged oppositely. Ejected to a shared chamber free of significant

external electric fields (Chapter 3.2.1), the core and shell droplets are attracted to one another by Coulombic forces, proportional to r^{-2}, where r is the inter-particle distance (Equation 1). At a sufficiently close distance, image charge on the opposing particle lead to an additional attracting force, proportional to r^{-5} [232]. Upon contact, the droplets form a capsule due to the difference in surface tension (as described in Chapter 2.3.1), and neutralize each other partially or completely by charge transfer [9,12,232,236]. Any net charge q_{caps} left in the capsules continue to attract droplets of the oppositely charged species. Next, the shell layer of the capsules is solidified if necessary, and the capsules are steered to a collection surface or dish by means of gravity, air flow, or electromagnetic forces. The sequence of solidification and collection depends on the respective methods (Chapter 2.3.1) used. Both the shell and core electrospraying liquids can consist of a single phase or a colloidal suspension. The structure of the produced capsules is determined most importantly by the droplet size and charge distributions, the non-volatile material concentrations in the electrospraying liquids, evaporation rates of volatile liquids, and the external electric field in the encapsulation space.

In CJM electrospraying, the main droplet size distribution is narrow (Chapter 2.2.2.2), and droplet charge is proportional to droplet size (Chapter 2.2.5). Ideally, if at any time interval the induced charge in the electrosprayed droplets available for encapsulation was of a similar proportion of the total electrosprayed charge for both of the parallel nozzles, the mean residual capsule charge $\overline{q_{\mathrm{caps}}}$ could be deduced qualitatively based on the measurable nozzle atomization currents I_{c} and I_{s}. In the case of current imbalance ($|I_{\mathrm{c}}| \neq |I_{\mathrm{s}}|$), the mean residual capsule charge $\overline{q_{\mathrm{caps}}} \neq 0$ would lean towards the sign of the stronger atomization current in magnitude. An improved process yield could then be gained by neutralization of the formed capsules, or by adjusting the polarity of the collection electrode accordingly to be of the opposite sign as $\overline{q_{\mathrm{caps}}}$. With balanced currents ($|I_{\mathrm{c}}| \sim |I_{\mathrm{s}}|$), $\overline{q_{\mathrm{caps}}} \sim 0$. In this scenario, selective collection of negatively charged, neutral, or positively charged capsules could possibly be exploited at the expense of process yield to potentially gain a higher capsule structural uniformity (by size) among the collected, charge filtered capsules, as compared to the whole of the electrosprayed sample. However, as discussed in Chapter 2.2.2.2, the contribution of satellite droplet charge could affect the encapsulation process significantly. In practice, optimization and verification of the parallel nozzle

electroencapsulation process is highly empirical in nature due to the wealth of variables generally involved in it.

The process yield can be scaled up in principle by increasing the numbers of core and shell liquid nozzles n_c and n_s in the parallel nozzle electroencapsulation setup, although a bipolar array would be more complex than a nozzle array comprised of a single polarity [9,89,91,93,95–102,236]. With roughly similar electrospraying parameters for each nozzle of the same type of electrospray, the total atomization currents could be coarsely balanced by weighing the numbers of operational nozzles according to $n_c I_c = n_s I_s$. However, the voltages would generally need to be increased as nozzles of opposite polarities are brought closer together, and in different parts of an electrospraying array, the electrospraying parameters would need to be tweaked due to differing geometry-dependent proximity effects [12,99]. As a result, the electrospraying currents I_c and I_s would likely vary by nozzle position in an array [89,99,102]. Coarse current balancing by adjusting n_c/n_s could still be applicable, if proportional variations of I_c and I_s by position in the array can be assumed to be similar, and if the array is sufficiently large that the proportion of edge nozzles can be considered small.

The parallel nozzle configuration is feasible for the production of solid nano- or micromatrix particles, with the payload (core) material loaded in the particles as a solid solution or a solid dispersion [7,240,252,254–256]. As in the single nozzle process (Chapter 2.3.2.1), the payload material is dissolved in the electrospraying liquid together with the matrix (shell) material [153,240,244,251]. In a basic arrangement, identical liquids are electrosprayed from both nozzles, using identical electrospraying parameters (except for the polarity). Thus, droplet yield can be doubled as compared to the single nozzle configuration. The droplets electrosprayed from each nozzle exhibit the same size and charge magnitude distributions, apart from possible effects of charge polarity on either distribution. Thus, external neutralization is not necessarily needed, as the atomization currents are generally balanced, and oppositely charged droplets are mutually neutralized partially or completely through charge transfer as they are attracted to one another by Coulombic forces and come to contact [258]. Droplet contacts prior to solidification lead to merging of the droplets. Solidified matrix particles with residual charge continue to attract droplets and particles of the opposite charge, until neutralized. Atomization current bias can be rectified as necessary by tweaking a parameter in one of the nozzles, most importantly the liquid properties and the core or

shell liquid flow rates, Q_c or Q_s (Equations 12, 15, and 18). In summary, the basic matrix particle production in the bi-polar parallel nozzle configuration, as compared to the corresponding single nozzle process, is essentially a scale up that also implements particle neutralization.

The bi-polar parallel nozzle configuration can be utilized to carry out chemical reactions in aerosol form between the oppositely charged electrosprayed droplet species, *i.e.* to produce *microreactors*. Two different reactants, or a reactant and a catalyst, can be electrosprayed from oppositely charged nozzles. As the bipolar droplets are attracted to each other and coagulate, a chemical reaction initiates within the merged droplet. For instance, a Bakelite monomer suspension and a polymerizing catalyst (H_2SO_4) were electrosprayed from separate nozzles by G. Langer and G. Yamate, and the Bakelite polymerized in the aerosol droplets that combined with H_2SO_4 droplets [232]. Other chemical reactors have been later designed using the parallel nozzle electrospraying configuration [10,225]. A specific advantage of electrosprayed microreactors is that the chemical reactions can be very fast and efficient due to the small size scale [10,258]. The technique has also been used for micro-mixing ceramic compounds, *e.g.* zirconium and titanium, inside coagulated droplets [258].

H. Fu *et. al.* have produced coagulated, spherical dual drug nanoparticles using the bi-polar parallel nozzle configuration, by electrospraying the two different drug solutions from separate nozzles [259]. F. Mou *et. al.* have demonstrated that electroencapsulation by using the bi-polar parallel nozzle configuration is a feasible technique for building *Janus particles* – compartmentalized colloids with two sides of different chemistry or polarity [260,261].

By careful co-formulation of the two different electrospraying liquids, micromatrix particles of various morphologies and compositions with a mixture of several different payload and matrix materials could potentially be produced with the bi-polar parallel nozzle configuration in a single-step process, even when a single liquid that simultaneously contained all of the materials was not suitable for electrospraying [9,12,232,236,237,240].

A more comprehensive presentation of a typical simple ($n_c = n_s = 1$) parallel nozzle experimental electroencapsulation setup is provided in Chapter 3.2.1.

2.3.2.3. Co-Axial Nozzles

The electroencapsulation principle for core-shell capsule production utilizing a pair of co-axial electrospraying nozzles is depicted schematically in Figure 5c. The immiscible core and shell liquids are electrosprayed together in CJM, with the core liquid readily enveloped axially by the shell liquid. The shell and core liquids can both be comprised of a single phase or a colloidal suspension. One of the liquids can be highly dielectric, as long as the second liquid is sufficiently conductive [9,227,236]. Charged, spherical core-shell capsules form immediately after droplets are electrosprayed from the tip of the composite Taylor cone. The capsule shell layer is then solidified as necessary, and the capsules are either neutralized prior to collection or collected on an oppositely charged electrode [9,12,236,237,242,248,262,263]. Capsule size and structure are determined most importantly by the non-volatile material concentrations in the electrosprayed liquids, liquid properties, the liquid flow rates Q_c and Q_s [237,238,248,262,264–266].

The number of co-axial nozzles can be increased for more complex capsule structures. Multilayered particles have been electrosprayed using tri-axial and even tetra-axial needles [12,237,267–269]. For an increased yield, the number of co-axial nozzle units can in principal be increased, and the units can be arranged in arrays similarly to single nozzle electrosprays [89,91,93,95–102].

Further, layered ceramic-ceramic encapsulation has been achieved using the co-axial configuration, for example by electrospraying alumina and zirconia suspensions to form ceramic-ceramic composite droplets [270].

2.3.2.4. Other Methods

In addition to the electrospraying configurations discussed so far, multi-channel needle electrospraying configurations have been utilized for the production of asymmetric and multiphase particles and nanocolloids, such as Janus particles, or compartmental particles of various shapes and compartment configurations [12,271–274].

In principle, electroencapsulation could possibly be performed using an exotic electrospraying configuration that omits capillary needles (*cf.* Chapter 2.2.1). However, such techniques will not be necessary to consider for the scope of this work.

2.4. Oral administration of Solid Drug Materials

Oral drug administration is often the preferred method for delivering drug materials and other therapeutic molecules to the circulatory system due to the relative comfort, low cost, and ease of dosage control associated with the method [275,276]. For a drug to produce the desired therapeutic effect, its *bioavailability*, the fraction of the administered dose that reaches the circulatory system without chemical degradation or decomposition, has to suffice. An orally administered drug needs to be absorbed in a specific part of the gastrointestinal (GI) tract; the principal absorption site for most drugs is located in the upper and middle parts of the small intestine, the duodenum and the jejunum [277,278]. To be absorbed, the drug must first be dissolved in the part of the GI tract leading to the absorption site [4]. All the while, the molecular integrity (chemical stability) of the drug must be retained [279].

Unfortunately, as many as 95% of the promising new drug candidates suffer from poor *physicochemical* or *pharmacokinetic* properties, which greatly limits the bioavailability of the drug when administered orally. Such disadvantageous drug properties include low stability, low solubility and low dissolution rate in the intestinal lumen, poor permeation of the GI tract wall, and high intestinal or hepatic first-pass metabolism [1–4,280,281].

The discussion in the following chapters focuses on the physicochemical and pharmacokinetic properties relevant for the oral bioavailability of solid drug materials, as well as formulation methodology to improve these properties.

2.4.1. Solid State of Pharmaceutical Materials

Solid matter is structurally rigid – the atoms are bound to each other tightly and closely in a durable arrangement, unlike in liquids and gases. As observed macroscopically, solids differ from liquids and gases in that solid matter has a definite volume and shape, it does not flow, and it exhibits elastic stiffness against shear stress. The atoms in a solid are immobile, although they do oscillate around fixed points at any temperature above 0 K. The arrangement of these fixed points constitutes the atomic structure. The atomic structure of a solid can be either *crystalline* (periodically ordered) or *amorphous* (disordered) [282–285].

A *crystal* is a solid composed of atoms arranged in a pattern periodic in three dimensions. This pattern is called the crystal *lattice* [282,285,286]. A crystalline solid may consist of a single crystal, or more often a *polycrystalline* aggregate that is composed of individual crystals (*crystallites* or *grains*). Crystals and crystallites can vary greatly in size, upward from the nm-range [282,287,288]. Most inorganic solids are naturally crystalline, including metals, covalent compounds (*e.g.* minerals, some ceramics), and ionic compounds (salts) [285]. Many compounds exhibit *polymorphism* – they can exist in more than one crystal structure (polymorphic form) [282,289,290]. In some cases, polymorphic forms can be distinguished by dramatic differences in physical properties, such as morphology, stability, mechanical strength, or dissolution rate [11,14,291]. Similarly, some elements (*i.e.* C) also exist in several crystal structures. This phenomenon is known as *allotropism* [292,293]. A stable crystal structure represents a local potential energy minimum of the atom system [14,285]. An external activation energy can trigger either crystallization or *recrystallization*, a solid state transformation where the atoms rearrange into the existing or another polymorphic form [282,294–296].

In amorphous solids (or *glasses*), the atoms lack any vestige of long-range order. The topologically disordered structures of amorphous solids are stochastic in nature, although the short-range structure is not completely random – the atoms have well-defined closest distances of approach, and hence amorphous solids have definite, radially distributed structures relative to the center of an average atom [284,286]. The amorphous structures can be described well by stochastic-geometry models such as the random-close-packing model (metallic glasses), the continuous-random-network (covalently bonded glasses), and the random coil model (organic polymers) [284]. The amorphous form of a substance is generally more energetic than the crystalline form(s) [285,297]. Thus, the amorphous form is most often unstable or metastable [6,235,297,298].

Crystallinity, the extent to which a solid is crystalline, most often lies between the extremes of an ideal single crystal and a completely amorphous solid. Crystals and crystallites always bear defects, manifesting as various kinds of point, linear, and planar discontinuities or deviations from the ordered structure. As an example, polycrystalline solids are of very high crystallinity but are strictly speaking not completely crystalline, since the layers between crystallites are disordered. The crystallite boundaries represent discontinuity

surfaces of the crystal structure, and the layers in between crystallites can be viewed as planar defects, or amorphous regions [282,299].

2.4.1.1. Drug Structural Stability

Most drug materials tend to form crystals in room conditions, and are formulated in a crystalline form in drug products [14,289]. The amorphous drug form is structurally unstable, thus it tends to crystallize spontaneously (Chapter 2.4.1). Similarly, some of the polymorphic forms may tend to recrystallize into a structurally more stable polymorphic form. To stabilize the solid form of the drug completely or to a certain extent, the drug can be dispersed as crystalline or amorphous particulates across the volume of solid excipient (*e.g.* a polymer) particles, in a solid dispersion formulation (Chapter 2.4.3) [7,234,240]. At the extreme dispersity, the drug is dispersed in a molecular form, to form a solid solution with the excipient (Chapter 2.4.3) [7,300]. The rate of solid state transformation depends not only on the structural energy difference of the solid states, but also on the dispersity and mobility of the drug molecules in the formulation [14,296,301]. The drug molecular mobility depends on the excipients and spatial confinement of the drug in the formulation, as well as the storage conditions (T, p, and humidity) [6,302,303]. The storage conditions influence the stability of the drug amorphous form, and the comparative structural stability of polymorphic forms [235,289,297,304,305].

The crystallinity and polymorphic form of the drug can crucially affect its physico-chemical properties, such as the dissolution rate [14,289,306]. Therefore, a solid state transition of an unstable form of the drug, for instance crystallization of an amorphous form due to incorrect storage conditions, could lead to a diminished dissolution in oral administration, posing a bioavailability barrier that could ultimately result in an inadequate therapeutic effect of the drug (Chapter 2.4.2).

At temperature T, the Gibbs free energy difference $\Delta G = \Delta H - T\Delta S$ obtained from solubility and melting data is a quantitative measure of the stability relationship between polymorphs, where the enthalpy term ΔH results from the structural (lattice) energy difference between polymorphs, and the entropy term $T\Delta S$ results from disorder and thermal vibration difference [297].

The reduced stability of the amorphous form is due to a generally higher free energy G, as compared to the crystalline forms. The excess free energy G of amorphous solids can be obtained from solubility or vapor pressure data,

similarly to crystalline solids [297]. The excess free energy consists in part of the excess enthalpy H, measurable from heats of solution or crystallization [297,301]. Some of the excess free energy is due to the molecular mobility, which in amorphous solids is generally not zero. The mobility is related to excess entropy, obtainable indirectly from $TS = H - G$ [303].

2.4.1.2. Drug Solubility

The *true* solubility (*saturation* solubility) s of a solid substance (*solute*) in a solvent is the maximum amount of solute that can be dissolved per unit volume of the solvent before the solution becomes *saturated*. The true solubility s of a solute in a particular solvent is an intrinsic property of the solute molecule that depends on T and p [5].

The *apparent* solubility (or simply, solubility) s_{app} is distinct from true solubility s; in certain conditions, the solute concentration C can temporarily or locally exceed the saturation limit ($C > s$) [7,307,308]. This abnormal, *supersaturated* state of a solution is thermodynamically unstable [308]. Over time, the solution will spontaneously approach a uniformly saturated state where solute diffusion, dissolution and precipitation are in a dynamic equilibrium [5,308]. An *undersaturated* (or *unsaturated*) solution ($C < s$) approaches saturation only with a large enough excess of the solid submerged in the solution.

In oral drug administration, the aqueous solubility of the drug at 37°C in the pH range of the GI tract (1.2–6.8) is relevant [281]. Poor water-solubility of the drug very commonly hampers or prevents sufficient dissolution of the drug prior to its migration to the optimal absorption site in the GI tract, leaving the bioavailability of the drug lacking (Chapter 2.4.2.1) [4,5]. The apparent solubility s_{app} of the drug can be enhanced by formulation of the solid state: s_{app} generally varies by polymorphic form according to ΔH [14,297,306]; furthermore, the amorphous form can exhibit a significantly higher s_{app} as compared to the crystalline forms, due to the higher G [6,235,307–309]. The extreme s_{app} is achieved for molecules released to a liquid solution from a solid solution, where the drug is readily dispersed in a molecular form (Chapter 2.4.3) [7,300].

2.4.2. Oral Bioavailability of Drugs

An orally administered drug product is usually designed, at the very least, to stabilize the drug in a pre-formulated solid state until its release, and to target the release in a certain section of the GI tract. During or after its release, the drug material must undergo a chain of processes before the drug molecules reach the circulatory system – most importantly, drug dissolution, permeation, and exposure to first-pass metabolism. Each of these processes potentially limits the attainable oral bioavailability of the drug. In the following Chapters, enhancement of the relevant physicochemical and pharmacokinetic drug properties by formulation for oral administration is discussed.

2.4.2.1. Drug Dissolution

The dissolution rate dC/dt of a solid substance can be expressed by the modified Noyes-Whitney equation [310,311]:

$$\frac{\mathrm{d}C}{\mathrm{d}t} = \frac{AD\left(s_{\mathrm{app}} - C\right)}{h}, \tag{20}$$

where A is the total contact area of the solid substance and the solution, D is the diffusion coefficient of the solute in the solution, C is the solute concentration and h is the thickness of the diffusion boundary layer at the solid-liquid interface. The dissolution model described Equation 20 demonstrates the reasoning for various strategies to improve drug dissolution in the GI tract.

A very common strategy to improve drug dissolution rate is to increase A in Equation 20. This can be achieved by decreasing the drug particle size, by increasing the porosity of drug particles, or by improving the wetting properties of the drug particles [4,5,7,235,309,312]. Another important means to improve drug dissolution rate is enhancement of s_{app}, which is possible by formulation of the drug in an optimal polymorphic form, or for better results, amorphous or molecular form (Chapters 2.4.1.2 and 2.4.3). The molecular form of the drug also represents the highest attainable A in the formulation. In consequence to the enhanced s_{app}, the drug dissolution burst can supersaturate the luminal fluid.

Usual methods for drug amorphization and particle size reduction include freeze drying, spray drying, and milling, for example [5,6,297,313,314]. However, these methods inflict significant physical or thermal stress on the drug, which may lead to degradation of sensitive drug materials [5]. In

addition, the micronized powder may agglomerate to a degree in some cases, which negates the benefit of comminution [7].

Lately, electrospraying of a drug solution has been shown to be a valid single-step method for the production of amorphous or crystalline drug micro- and nanoparticles [10,12,315]. The size, crystallinity, or even porosity of the electrosprayed drug particles have been shown to be adjustable in many scenarios by varying the electrospraying parameters [9,13,83,113]. In several studies, various electrosprayed bio- and drug materials have been shown not to degrade in the process [9,12,113,242,316,317].

Improving sink conditions in the intestinal lumen to reduce C on the right-hand side of Equation 20 is beneficial for maintaining the dissolution rate dC/dt at a high level for further dissolving drugs [318]. Of course, the effect on drug bioavailability directly depends on the pharmacokinetic nature of the sink. Changes in hydrodynamics to influence h are difficult to implement *in vivo* [7]. Moreover, D varies between subjects and event within subjects according to the fed and fasted state [300]. The total drug dissolution can be improved to some extent by administrating the drug in a fed state, which increases the time available for dissolution, and could also improve the dissolution rate [7,319].

2.4.2.2. Intestinal Drug Permeation

The rate of intestinal drug permeation (transepithelial transport), *i.e.* the flow of the dissolved drug molecules through the intestinal wall, is proportional to the drug concentration gradient across the membrane, and the intestinal permeability of the drug [3,4,281,308]. Thus, ample drug dissolution is advantageous for reaching sufficient drug permeation. Drug permeability depends on the drug lipophilic and hydrophilic properties, and the properties of the membrane at the permeation site such as pH, mucus production, and intercellular Ca content [4,281,320].

Drug permeation acts to enforce sink conditions in the intestinal lumen, while benefiting the drug bioavailability (Chapter 2.4.2.1). Therefore in certain scenarios, enhancing the drug permeability can also significantly improve the drug dissolution rate in the GI tract. Consequently, research has been conducted to improve drug permeation *i.e.* by the use of suitable excipients [321,322]. According to the dissolution model of Equation 20, the effect of increasing the permeation rate to the drug dissolution rate remains quite limited, unless the permeation rate is initially significantly lower than the dissolution rate. Furthermore, if the intestinal fluids at the permeation sites

saturate, and if the drug bioavailability is limited by its permeation rate rather than the dissolution rate, then attempts to increase dissolution rate without also either boosting s_{app} or enhancing the intestinal permeability to improve sink conditions would yield no further benefit to bioavailability.

2.4.2.3. First-Pass Metabolism

In the course of transit towards the circulatory system, an orally administered drug material eventually comes to contact with or dissolves to the digestive fluids in the GI tract. Thus, the drug is exposed to intestinal metabolism, which can be catalyzed by various enzymes mainly in the oral cavity, stomach, and the small intestine [320,323,324]. Drugs that go on to permeate the GI tract wall are further exposed to hepatic metabolism, before allowed to the circulation for the first time [4,320,325]. These degrading and decomposing biotransformation processes constitute the most important phases of drug first-pass metabolism, which can severely limit the drug oral bioavailability [5,281,323,325].

2.4.3. Drug Carrier Formulations to Improve Oral Bioavailability

Traditionally, orally administered solid drug formulations consist of compacts (tablets) of micronized drug material and excipients. Several compacts can be packaged in a dosage form to a pH-sensitively soluble capsule for an extra layer of protection and release targeting.

These kinds of basic dosage formulations may not provide adequate oral bioavailability for drugs of unfavorable physicochemical or pharmacokinetic properties, such as poor solubility. The limiting physicochemical or pharmacokinetic properties can be improved for example by nanosizing and amorphization of the drug (Chapter 2.4.2), to approach a sufficient drug bioavailability for the oral route of administration to become feasible. In such advanced formulations, it is often subsequently necessary to stabilize the drug solid state for the duration of the drug product being stored, and furthermore during the initial stages of oral administration until the drug is released. Solid state stabilization by physical confinement of the drug material can be carried out in many ways: by utilizing excipients as drug stabilizing binders to form eutectic mixtures [7,326], solid dispersions [240,309], or amorphous solid solutions [7] (Chapter 2.4.3.1); by integrating the drug molecules into the crystal structure of the drug carrier material to form crystalline solid solutions [7] (Chapter 2.4.3.1), or co-crystals [327,328]; or by loading the drug to a

biocompatible carrier host, such as suitable porous Si micro- or nanoparticles [16,276,329,330] (Chapter 2.4.3.2).

2.4.3.1. Drug Solid Dispersions and Solid Solutions

The solid state and dispersity of a drug can in many cases be sustained or stabilized by formulating the drug as a (phase separated) solid dispersion or a solid solution [7,235,300,331–335]. Originally conceptualized by Sekiguchi and Obi in 1961 [326], a phase separated drug solid dispersion consists of amorphous or nanocrystalline drug particulates distributed uniformly across the volume of a binding and stabilizing excipient (solvent), such as a suitable hydrophilic polymer [7,240]. Some widely used solvent polymers include *e.g.* polyvinylpyrrolidone (PVP), and polyethylene glycols (PEGs) [5,300,332,333,336]. A molecularly dispersed drug (solute) forms a solid solution with the solid solvent [7,300]. In amorphous solid solutions, the solute molecules are dispersed homogenously in a disordered, rigid network formed by the solvent molecules (*cf.* Chapter 2.4.1) [7,300]. Crystalline solid solutions are substitutional or interstitial: the solute molecules substitute solvent lattice molecules or occupy interstices in the solvent lattice, depending principally on the relative size difference of the solvent and solute molecules [7,300]. A solid solution is analogous to a liquid solution in the sense that both consist of a single phase of matter [7]. The fundamental difference between solid and liquid solutions is found in the mobilities of both the solute and the solvent molecules.

In phase separated solid dispersions and solid solutions, the drug particulates are held in place mechanically to a degree by the solid structure. More importantly, the surface molecules of drug particulates and single drug molecules are bound to the excipient by chemical interactions (*e.g.* hydrogen bonding), constricting or even practically halting the long-range movement of drug molecules (Chapter 2.4.1.1) [313,337,338]. Thus, the processes of drug particle agglomeration and solid state transformation can be slowed down, or prevented altogether (Chapter 2.4.1.1) [94,300,305,339,340]. In effect, the drug is temporarily suspended in either a disordered state (molecular dispersion or amorphous particulate dispersion); or a state of reduced order (nanocrystalline particulate dispersion), as compared to the bulk or micronized powder states [7,94,335,341]. Furthermore, solid dispersion and solid solution formulations can maintain a significantly increased surface area A of the dispersed drug material available for dissolution for an extended period of time. Consequently, the dissolution rate of a poorly soluble drug from solid dispersion or solid

solution formulations can be greatly enhanced (Chapter 2.4.2.1) [333,342,343]. However, it can be challenging to formulate a sufficiently stable solid dispersion or solid solution of a specific drug in order to prevent its crystallization and retain the enhanced drug dissolution properties over extended periods of time in storage [344,345].

Drug solid dispersion and solid solution formulations can be prepared for example by spray-drying [300,334], freeze-drying [300,335,346], or by the hot-melt method [5,300,345]. Lately, electrospraying has emerged as an alternative method in the production of solid dispersion and solid solution drug formulations. By electrospraying a common solution or melt of the drug and excipients, and subsequent solvent evaporation or cooling, very small and monodisperse drug loaded matrix particles can be produced in a single-step electroencapsulation process, as further discussed in Chapter 2.3 (Electroencapsulation) [94,153,154,240,252,253,256].

Orally administered solid dispersion and solid solution formulations of a drug are designed to maintain the solid state and dispersity of the drug until it is released or directly dissolved to the fluids in the GI tract. The drug release triggering conditions and release kinetics, and thus the *in vivo* release site and drug release rate, are influenced by the composition, size, porosity and morphology of the carrier particles, the solid state and distribution of the drug material within the carrier particles, as well as biological factors [7,253,300,347]. Drug release targeting can minimize unnecessary exposure of the drug to intestinal metabolism, as well as possible drug-induced side effects to the gastric walls [323,324,348]. The dissolved drug concentration C at the absorption site can be maximized by drug release targeting to promote drug absorption [277,278,349]: the release of a poorly soluble drug from a solid solution often supersaturates the gastrointestinal fluid locally (Chapter 2.4.1.2), potentially enhancing the transepithelial transport of the drug (Chapter 2.4.2.2) [300].

2.4.3.2. Drug Loading to Porous Silicon Particles

The feasibility of *mesoporous* (pore size 2–50 nm) silicon (PSi) micro- and nanoparticles as functional drug carriers to enhance the oral bioavailability of various poorly soluble, poorly permeable, or otherwise problematic drug materials have been researched extensively, with promising results [16–18,276,302,329,350–360]. The surface chemistry, porosity, and pore size of PSi micro- and nanoparticles can be modified and controlled in the manufacturing

stage [17,276,329,354,355,361]. Thus, the PSi particles can be tailored to favor adsorption of certain molecules or cells [17,276,329]; the drug release rate can be controlled [329,362]; all the while making the PSi particles biocompatible [353,355,357]. The ratio of PSi surface area available for drug loading to the mass of the PSi particles can be as high as 100–800 m^2/g [276,361]. Temperature sensitive drugs such as proteins and peptides (*e.g.* insulin) can be loaded to the pores of PSi particles without risking thermal degradation, as loading is possible in room temperature solutions [17,276,354,363,364]. In addition, the photonic properties of PSi can potentially be harnessed for tracking the drug delivery process [329].

The drug loaded in the PSi pores is effectively dispersed as clusters separated by pore walls. At high enough drug payloads in the PSi pores, the drug partially begins to crystallize on the surface of PSi particles during the loading process, which is usually avoided by moderating the loading degree, or remedied by rinsing the particles after loading [350,365]. The total free surface area A of a drug loaded to the pores of PSi particles can be very large, although it is inevitably smaller than the PSi total surface area available for drug adsorption. In sufficiently small pores, the crystallization of the drug molecules may be prevented by spatial confinement exerted on the drug molecules by the pore walls, and the loaded drug remains at least partially in an amorphous form [302,351,365]. These qualities, together with the wetting properties of the PSi particles in certain cases [17], can result in a greatly increased dissolution rate of the loaded drug (Chapter 2.4.2.1) [17,276,302,351]. In addition, the permeation of the loaded drug across Caco-2 and Caco-2/HT29 intestinal-derived cell monolayers have been reported to improve in some scenarios [18,352,354,366].

Nanoparticles in general tend to form aggregates due to Van der Waals attraction and other interactions [367–369]. Thus, the physical handling and *in vivo* dosing of PSi nanoparticles remain a considerable challenge. Another difficulty lies in the optimal drug release targeting from PSi. In certain scenarios, the drug can be prematurely released, which could unnecessarily extend the exposure of the drug to intestinal metabolism (Chapter 2.4.2.3) [370].

3. Experimental

3.1. Materials

3.1.1. Model Drugs

Griseofulvin is an antifungal drug first isolated in 1939 [371]. Classified as a Biopharmaceutics Classification System (BCS) class II (low aqueous solubility, high permeability) drug, the low dissolution rate of griseofulvin limits its GI absorption, and therefore oral bioavailability [372]. The apparent solubility of crystalline griseofulvin in H_2O at room temperature is *ca*. 8–10 μg/ml within a wide dispersion concentration range, practically independently of the pH [17,307,373–376]. Griseofulvin has a high tendency to crystallize, even at room temperature and low humidity, and its crystallization rate is very fast [296,377,378]. Because of these properties, griseofulvin (Orion Pharma, Finland, and Sigma-Aldrich, U.S.A.) was selected as a model drug for electroencapsulation in micromatrix particles (papers I and III).

Piroxicam is non-steroidal anti-inflammatory drug of BCS class II [372,379]. Piroxicam exhibits tautomerism and polymorphism [380,381]. Previously, the crystal structures of three polymorphs have been calculated and verified experimentally: form I, form II, and form III [290,381–384]. In addition, α_1-form (previously also α-form) has been reported, but its existence has not been verified [383,385]. Finally, the structure of piroxicam monohydrate crystal has been calculated and verified experimentally [386]. Form I is the most stable form in ambient conditions, and used for electrospraying liquid formulation in paper II (Hawkins Pharmaceuticals, U.S.A.).

3.1.2. Polymers

Eudragit L 100 and Eudragit L 100-55 (Evonik Industries, Germany) are *enteric* methacrylate copolymers that dissolve in water above the threshold pH of 6.0 and 5.5, respectively. Eudragit L 100 and Eudragit L 100-55 were used as the polymer matrix material in micromatrix particles produced in papers I and III.

Eudragit E 100 (Evonik Industries, Germany) is a cationic copolymer, water-soluble below pH 5.0. In papers I and IV, Eudragit E 100 was used as the shell polymer in electrosprayed core-shell microcapsules.

3.1.3. Solvents and Additives

In papers I and IV, analytical-grade glycerol (99.9% purity, MP Biomedicals, Solon, OH) was the base solvent in microcapsule core liquid electrospraying formulations. The core liquid conductivity K_c was controlled by NaI (Merck, Germany) doping, and heating. The effects of NaI concentration C_{NaI} and temperature T on K_c were measured using a HI 8033 conductivity meter (Hanna Instruments, Romania) in paper I, and a Zetasizer Nano series zeta potential measurement instrument (Malvern, U.K.) in paper IV. Generation of submicron NaI-doped glycerol droplets by electrospraying has been previously reported [130,149]. In papers I and III, glycerol was also used as an anti-static plasticizer in micromatrix particles.

In papers I, II, and IV, analytical-grade chloroform (99.0% purity, Merck, Germany) was the base solvent in microcapsule shell liquid and drug particle electrospraying formulations. In papers I and III, ethanol (99.5% purity, Altia, Finland) was used as the base solvent in micromatrix particle electrospraying liquid formulations. Fine (< 53 μm) particles of talc (Ciba Specialty Chemicals Oy, Finland) were dispersed as an anti-tack agent in the micromatrix particle and microcapsule shell liquid electrospraying formulations (papers I, III, IV).

Dichloromethane (DCM; Merck KGaA, Germany) was used as a drug loading solution in papers I and III.

3.1.4. Mesoporous Silicon Particles

In the present work, PSi micro- and nanoparticles (*cf.* Chapter 2.4.3.2) were manufactured from Si wafers (Siegert Wafer GmbH, Germany, or Cemat Silicon, Poland), using previously reported methods, as specified per surface chemistry.

For paper I, thermally carbonized PSi (TCPSi) microparticles were manufactured, using a previously reported method [17]. For papers I and III, thermally oxidized PSi (TOPSi) nanoparticles were manufactured [356], with a hydrodynamic diameter (Z-average) of 163.0 nm, and polydispersity index (PdI) of 0.094 as measured for paper III. For paper IV, TCPSi nanoparticles with a hydrodynamic diameter of 147.0 nm, and PdI of 0.109, were manufactured [356,357,387].

In papers I and III, griseofulvin was loaded to the pores of TOPSi nanoparticles in a DCM loading solution. Griseofulvin has previously been experimentally loaded in an amorphous form into the pores of TCPSi microparticles, thermally hydrocarbonized PSi (THCPSi) microparticles, and TOPSi nanoparticles as a model drug in research of oral drug delivery and controlled release applications [17,18,302].

3.1.5. Phosphate-Buffered Saline

Phosphate-buffered saline (PBS) is a test solution used for *in vitro* dissolution experiments to simulate the small intestine conditions [219,277,357]. For paper III, PBS with a phosphate molar concentration of 0.02 M was prepared by dissolving 7.81 mmol of KH_2PO_4, 12.21 mmol of $K_2HPO_4 \cdot 3H_2O$, and 0.146 mol of NaCl in 1000 ml of deionized water, which was produced using a Direct-Q 5 UV system (Merck Millipore, U.S.A.). The final pH was adjusted to 6.80 ± 0.02 by adding HCl (Oy FF-Chemicals Ab, Finland).

3.2. Methods

3.2.1. Electrospraying Methods

3.2.1.1. Bi-Polar Parallel Nozzle Electroencapsulation

In papers I, III, and IV, core-shell microcapsules and micromatrix particles were produced using a versatile bi-polar parallel nozzle electroencapsulation setup. The electroencapsulation parameters (atomization voltages; liquid flow rates; geometry of the nozzles, electrodes, and electrospraying chamber; liquid composition and properties; ambient, nozzle, and chamber temperatures) vary in part between the papers, but the parameter ranges are outlined in this chapter. The latest variation of the setup (paper IV) is depicted in Figure 6.

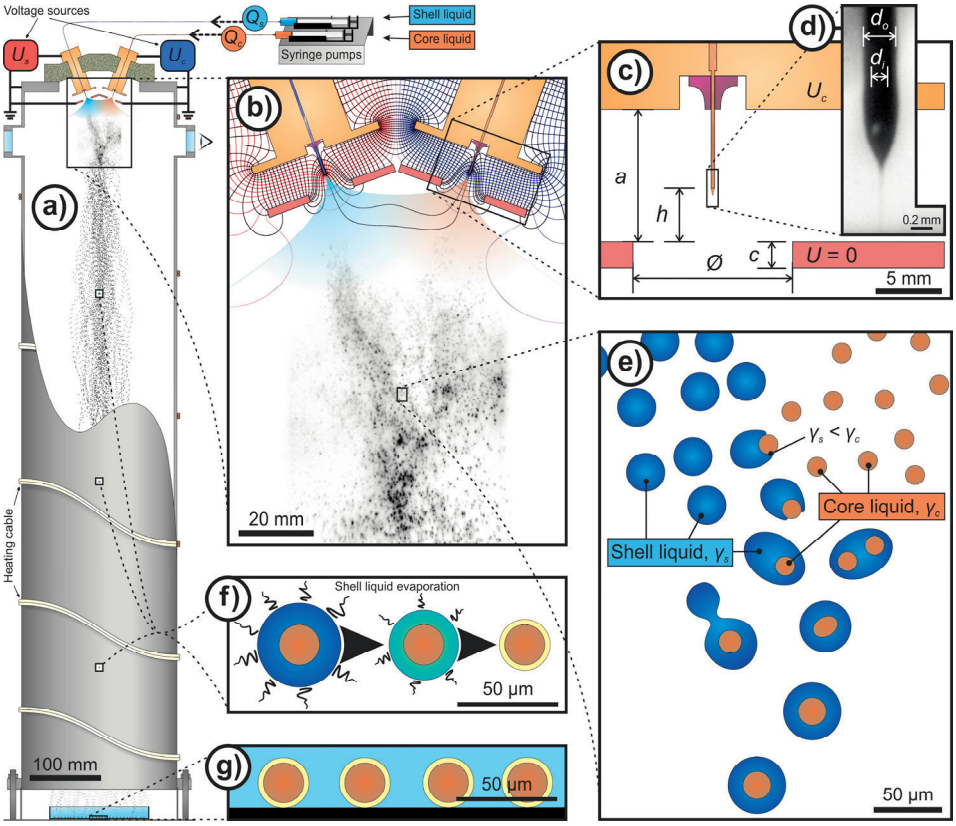

Figure 6. a) The bi-polar parallel nozzle electroencapsulation setup used for the experimental work in paper IV. b) Simulated electric field lines and equipotential curves (0.26 kV division) in the vicinity of the electrospraying nozzles, shown for nozzle voltages $U_s = +3.25$ kV and $U_c = -3.77$ kV. A photograph (1.00 ms exposure) of the combining oppositely charged electrosprayed droplets is inserted in the actual position and scale. c) Detailed cross-section of the core liquid electrospraying geometry. For both nozzles, $a = 10.0$ mm, $c = 2.0$ mm, $h = 4.0$ mm, $Ø = 12.0$ mm. d) Photograph of NaI-doped glycerol (NaI concentration $C_{NaI} = 0.50$ mg/ml) being electrosprayed from the core liquid nozzle at $U_c = -3.75$ kV, liquid flow rate of $Q_c = 0.50$ ml/h, and nozzle outer and inner diameters of $d_o = 0.30$ mm and $d_i = 0.15$ mm. e) Encapsulation of the electrosprayed droplets. f) Solvent evaporation from the capsule shell layer during capsule fall. g) Collection of the solid-shell capsules in the bottom of the chamber.

As depicted in the top of Figure 6a, the dual-capillary electrospraying device used for the electroencapsulation setup consisted of a pair of conductive and heatable capillaries angled 20° relative to the vertical, connected to guard

electrodes of diameter 36.0 mm, and kept in oppositely signed high potentials U_i using two high-voltage DC-DC converters (Spellman MM-series, U.K.). The capillaries penetrated a circular, insulating polyoxymethylene (POM) lid. Electrospraying voltages of magnitudes 2.9–5.6 kV were used (throughout papers I, III, and IV) for CJM electrospraying. Liquid flow rates Q_i were controlled using a pair of syringe pumps (New Era Pump Systems, Inc., NE-501 model, U.S.A.). Flow rates Q_i of 0.25–3.00 ml/h were used. The extractor plate electrodes (Figures 6b–c) were of thickness $c = 2.0$ mm, outer diameter of 36.0 mm, and with a round hole of diameter $Ø = 12.0$ mm in the middle. The extractor electrodes were suspended from the capillaries using insulating materials (not shown in Figures 6a–c), and grounded. The adjustable inter-electrode distance a was 9–10 mm, identically for both of the capillaries in each paper. Precision stainless steel dispensing tips (EFD, U.S.A.) of inner diameters d_i of 0.15–0.51 mm were used as spraying nozzles. Both nozzle tips were positioned identically, a distance h of 4–5 mm above the extractor (ground) electrode (Figure 6c). In Figure 6d, a close-up photograph of the Taylor cone is shown for NaI-doped glycerol, the core liquid electrosprayed in papers I and IV.

The POM lid holding the dual-capillary electrospraying device sealed the top of a steel electrospraying chamber, which was grounded (Figure 6a). Two electroencapsulation chambers of different sizes were used, each consisting of an open-ended cylinder, complete with a pair of air-tight observation windows and a ventilation channel in the upper part of the chamber. Each chamber was depressurizable and heatable. The chamber temperature T was 20–70°C, and controlled using a temperature control unit (Meyer-Vastus, Finland), and a heating cable (Horst, Germany) coiled around the chamber. Shown in Figure 6a is the large chamber (height 1040 mm, inner diameter 210 mm), used in papers III and IV. The small chamber, of height 740 mm and inner diameter 110 mm, was used for electroencapsulation in paper I.

In Figure 6b, a closer view of the electrospraying nozzles and the encapsulation region below the extractor electrodes is shown. Simulated electric field lines and equipotential lines are shown for the electroencapsulation parameters of paper IV with no droplets present, and the shell and core nozzle voltages U_s and U_c set asymmetrically. As can be observed, the electric field is strong and axisymmetric close to each of the nozzles and between the electrodes to suffice for CJM electrospraying of each liquid. However, in the encapsulation region, the external electric field is very weak, and the field

generated by electrosprayed droplets would easily become significant. Therefore, as discussed in Chapter 2.3.2.2., effective combination and neutralization of the oppositely charged electrosprayed droplets through mutual Coulombic attraction and contact charge transfer was possible in the encapsulation region (Figure 6e). This is further illustrated by the photograph in Figure 6b, where the typical momentary shapes of the electrosprayed droplet clouds are shown in the encapsulation region.

During the fall of the formed neutral capsules (or micromatrix particles) inside the electrospraying chamber (Figure 6f), excess solvent was evaporated from the capsule shell layers (particles). Where necessary, heating was applied to enhance the evaporation rate, thus ensuring complete solidification of the capsule shell layers (particles) prior to collection (Figure 6g).

3.2.1.2. Electrospraying of Drug Particles

In paper II, drug microparticles were produced by electrospraying in CJM into the depressurizable, grounded small chamber described in Chapter 3.2.1.1. A vertically aligned axisymmetric single-nozzle electrospraying device was integrated to a flat steel lid which closed the top of the electrospraying chamber. The electrospraying device consisted firstly of an electrospraying capillary, which penetrated the center of the chamber lid and was electrically isolated from it. The capillary was kept in positively signed high voltage, and penetrated an equipotential circular guard plate electrode inside the electrospraying chamber. A grounded circular extractor plate electrode with a hole in the center was suspended *ca*. 1 cm beneath the electrospraying nozzle, parallel to the guard electrode. The electrosprayed droplets were neutralized by a negative polarity Corona neutralizer (*cf*. Chapter 2.1.4.3.), which was attached off-center underneath the extractor electrode, and pointed perpendicularly to the droplet trajectory passing through the extractor electrode hole. Additional details of the electrospraying apparatus are provided in previously published work [113].

The electrospraying was conducted in room temperature. Where necessary, the solvent evaporation rate from the droplets was improved by depressurizing the electrospraying chamber. Pressures p of 0.5–1.0 bar were used. The electrospraying parameters are described in more detail in paper II, and previously published work [113].

3.2.2. Atomization Current Measurement

Atomization current I was determined using the control and measurement circuit shown in Figure 7, where U_ε is the source voltage. As detailed in paper IV, for liquid flow rate Q, the current fed by the circuit to the atomization nozzle was expressible as

$$I_{\mathrm{N}}(Q) = \frac{\frac{R_2+R_{\mathrm{V}}}{R_2 R_{\mathrm{V}}}R_1+1}{R} V_{\mathrm{A-B}}(Q) - \frac{R_2+R_{\mathrm{V}}}{R_2 R_{\mathrm{V}}} V_{\mathrm{B}}(Q), \qquad (21)$$

where $R = 500$ MΩ (thick film resistor, Ohmite, Mexico), $R_1 = 999$ MΩ and $R_2 = 1.11$ MΩ were voltage divider resistances (Emco High Voltage Corporation Model V1G, U.S.A.), $R_{\mathrm{V}} = 10.0$ MΩ was the internal resistance of the multimeters (Fluke 79 III, U.S.A.; and YFE YF-3503, Taiwan) used for monitoring voltages V_{A} and V_{B}. To obtain $I_{\mathrm{N}}(Q)$, the voltage $V_{\mathrm{A-B}}$ was measured with high precision using an electrometer (Keithley 6514, U.S.A.). Due to the high internal resistance ($R_{\mathrm{EM}} > 200$ TΩ) of the electrometer, $I_{\mathrm{EM}} << V_{\mathrm{B}}/R_{\mathrm{V}}$ and $V_{\mathrm{A-B}} \approx V_{\mathrm{A}} - V_{\mathrm{B}}$. The current $I_{\mathrm{N}}(Q)$ was measured at least eight times as averages over periods of 30 s for each investigated value of Q. The time-dependent baseline $I_{\mathrm{N}}(Q = 0)$ was determined similarly, in-between measuring the $I_{\mathrm{N}}(Q)$ data sets for each $Q > 0$. The observed current difference $I(Q) = I_{\mathrm{N}}(Q) - I_{\mathrm{N}}(0)$ consisted principally of the atomization current at liquid flow rate Q and the capacitive charging current of the liquid. The capacitive charging current was minimized by allowing the system to stabilize for 5–10 min prior to each set of current measurements, as detailed in paper IV.

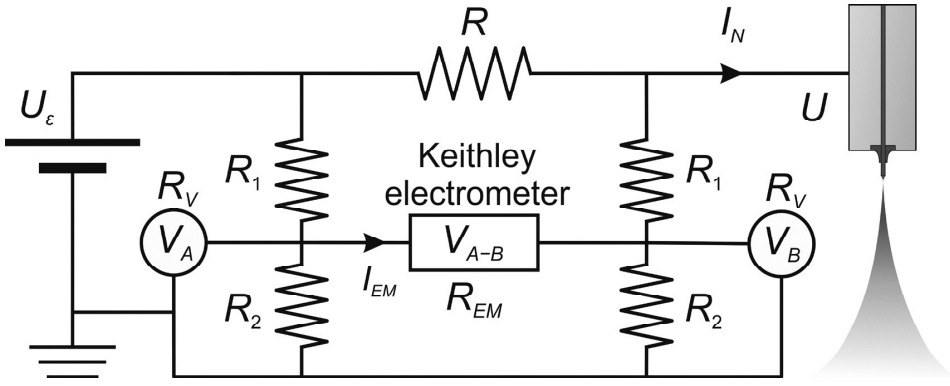

Figure 7. The electrospraying control circuit used for the measurement of atomization current $I(Q) = I_{\mathrm{N}}(Q) - I_{\mathrm{N}}(0)$.

3.2.3. Weighing

The accurate and repeatable weighing of the produced microcapsule samples was especially important in paper IV, and care was taken in the weighing procedure. An AG245 analytical balance (Mettler Toledo, U.S.A.) was electrostatically shielded and grounded, and then used for the measurements. The precision setting was 10^{-5} g. The electroencapsulated samples were weighed while in the pre-weighed Petri dishes used for sample collection. The collection dish was placed in a tight fitting Al enclosure, which was grounded *in situ* before recording its weight. A centered and repeatable weight distribution on the scale platform was ensured by a fixed metal ring on the platform. Drift was accounted for by letting the scale settle for 5 minutes in each measurement before reading the weight. The measurements were repeated. Any erroneous measurements due to unwanted contacts or improper closure of the Al sample pan were discarded and restarted immediately.

3.2.4. Optical Microscopy

The integrity of the produced microcapsules and micromatrix particles were assessed on-site during coarse electrospraying parameter adjustments using an optical microscope (Olympus BH-2, Japan). The size distributions of the produced microcapsules and micromatrix particles (papers I, III, and IV), as well as calibration droplets (paper IV), were determined from microscope images, captured using a mounted camera (Canon Powershot A630, Japan). The images were analyzed using ImageJ 1.47v software (Wayne Rasband, NIH, U.S.A.) to obtain the projection areas A_i of the imaged objects.

3.2.5. Scanning Electron Microscopy

During the experimental work for paper I, preliminary capsule batches were imaged using an S200 scanning electron microscopy (SEM) system (Cambridge Instruments, Cambridge, UK) to provide additional information on the capsule shapes and integrity (images not published).

In paper II, samples of the produced piroxicam particles were imaged using a Vega SB SEM system (Tescan U.S.A., Warrendale, PA, U.S.A.). The particle size distribution was analyzed from the images using Image-Pro Plus 1.3 software (Media Cybernetics, Inc., Rockville, MD, U.S.A.).

3.2.6. Transmission Electron Microscopy

In paper III, TOPSi nanoparticles electroencapsulated in micromatrix particles were imaged by transmission electron microscopy (TEM), using a JEM-1400Plus microscope (Jeon, Japan).

3.2.7. X-Ray Computed Tomography

In paper I, the structure of microcapsules and distribution of the PSi particle payload was analyzed by micro- and nanoscale X-ray computed tomography imaging, using a SkyScan 1172 μCT (Belgium), and an Xradia nanoCT (U.S.A.) imaging equipment.

3.2.8. X-Ray Diffraction

The crystal structures of each crystalline compound, and their polymorphic forms, are in general different. Thus, the measured X-ray diffraction (XRD) pattern of each crystal lattice is usually unique. More specifically, the crystal system and crystal parameters determine the possible diffraction angles 2θ of monochromatic X-rays (of wavelength λ), according to the Bragg law: $\lambda = 2d_{hkl}\sin\theta$, where d_{hkl} is the interplanar distance of the diffracting lattice planes *hkl*. The relative intensities of the measured diffraction peaks are influenced by the overall electron configuration in the lattice, as well as the preferred crystal orientation (texture) in the measured sample. Amorphous solids do not diffract X-rays. However, the presence of significant amorphicity can be detected in an XRD measurement: X-ray scattering from any amorphous solid produces a characteristic, very broad intensity maximum to the measured diffractogram. Its position (*d*-value) relates to the average nearest neighbor inter-atomic distance in an amorphous solid (*cf.* Chapter 2.4.1), which is a few Ångströms [282,286].

In papers II and III, the integrity and purity of the raw pharmaceutical compounds was validated by XRD measurements. Furthermore, the crystallinity, polymorphic forms, and stability of the electrosprayed pharmaceutical compounds were analyzed. The measurements were carried out mostly with an X'Pert Pro MPD diffractometer (PANalytical, Netherlands; papers II and III), and additionally with a Scintag X-1 XRD system (Scintag Inc., Cupertino, CA, U.S.A.; paper III). In both systems, Cu-*K*α radiation (λ = 1.541874 Å) was used.

In paper III, a variable temperature X-ray diffraction (VTXRD) measurement was performed at temperatures of 28–195°C to observe the recrystallization of electrosprayed piroxicam to form I. In the VTXRD measurement, the X'pert Pro MPD system was used with a TTK 450 sample heating chamber (Anton Paar, Graz, Austria).

3.2.9. Thermogravimetric Analysis

A thermogravimetric analysis (TGA) was used to determine the coarse griseofulvin loading degree in TOPSi nanoparticles (paper I) [17,388]. In paper IV, TGA was performed to investigate the average ratio of core and shell material mass in the produced microcapsule samples. The microcapsule samples were heated from 25°C to 950°C at a rate of 25.0°C/min. A TGA 7 thermogravimeter (PerkinElmer, Waltham, MA, U.S.A.) was used for the measurements.

3.2.10. Differential Scanning Calorimetry

Differential scanning calorimetry (DSC) was used to estimate the proportion of loaded griseofulvin within the pores of TOPSi nanoparticles in paper I [17,388]. Furthermore, DSC was used as a supplementary thermal analysis method to verify the crystallinity, polymorphic form and stability properties of the drug materials in electrosprayed piroxicam particles (paper II) and micromatrix particles containing griseofulvin solid dispersions (paper III). All of the DSC measurements were carried out using a Pyris Diamond differential scanning calorimeter (PerkinElmer, Waltham, MA, U.S.A.). The instrument was calibrated using In references. The samples were sealed in Al sample pans, and measured under a N_2 purge gas flow. In papers II and III, a heating rate of 10°C/min was used.

3.2.11. High Performance Liquid Chromatography

High performance liquid chromatography (HPLC) analysis was performed in paper II to detect degradation products in the electrosprayed piroxicam particles. In paper III, the griseofulvin concentrations C_{gr} in the *in vitro* permeation experiments were determined using HPLC at a detection wavelength of $\lambda = 292$ nm (Chapter 3.2.16). An Agilent 1100 Series HPLC

system (Agilent Technologies, Waldbronn, Germany) was used for all of the measurements.

3.2.12. Raman Spectroscopy

Raman spectra of the piroxicam particles produced in paper II were measured using an InVia spectrometer (Renishaw, Wotton-under-Edge, U.K.), to obtain additional structural comparison information between the electrosprayed piroxicam and form I piroxicam. A laser excitation wavelength of λ = 785 nm was used.

3.2.13. Fourier Transform Infrared Spectroscopy

In paper II, Fourier transform infrared (FTIR) spectra of the electrosprayed and form I piroxicam were measured with a Spectrum BX spectrometer (PerkinElmer, Waltham, MA, U.S.A.), using MIRacle attenuated total reflectance accessory (Pike Technologies Inc., Madison, WI, U.S.A.).

3.2.14. UV/Vis Spectroscopy

The griseofulvin loading degree in TOPSi nanoparticles was measured in paper III by ultraviolet/visible (UV/Vis) spectrophotometry. Furthermore, UV/Vis spectroscopy was used for the measurement of the degree of griseofulvin dissolution from free griseofulvin, as well as micromatrix particle samples carrying either griseofulvin dispersions or dispersions of griseofulvin loaded TOPSi nanoparticles. The UV/Vis measurements were carried out using a Labrox (Finland) UV spectrophotometer and UV-star (Greiner, Germany) microplates. The sample optical thickness was 5.7 mm. The transmitted intensity at the wavelength of the principal characteristic absorbance peak of griseofulvin in the UV/Vis spectrum (λ = 292 nm) was observed in the measured samples [375]. Subsequently, the C_{gr} in the measured solutions were calculated according to the Beer-Lambert law. Calibration curves were obtained by measuring corresponding solutions with known values of C_{gr} in the range of 0–4 μg/ml. The measured values were compensated for replenishment of the dissolution medium for each withdrawn aliquot in the dissolution experiment (Chapter 3.2.15).

3.2.15. *In Vitro* Drug Dissolution Modelling

In paper III, the dissolution rate of griseofulvin from the free griseofulvin powder, and produced micromatrix particles was investigated. Both HCl (pH 1.2) and PBS (pH 6.8) were used as dissolution media to simulate gastric and small intestine pH conditions, respectively. Each dissolution experiment was completely carried out in triplicate, at a constant temperature of $T = 37 \pm 2$°C in a magnetically stirred (100 rpm, tightly-fitted stirring bars) 25.0 ml volume of the dissolution medium. To satisfy the sink conditions, the initial griseofulvin mass m_{gr} of each dissolution sample was kept constant at 25 ± 1 μg, corresponding to C_{gr} = 1.0 μg/ml for a sample completely dissolved in the stirred medium. Aliquots of 500 μl were withdrawn from the dissolution medium at pre-determined time points, and replaced with fresh dissolution medium. The aliquots were centrifuged using a MicroCL 17 centrifuge (Thermo, Germany). From the supernatant, two 200 μl samples were obtained for C_{gr} measurements (Chapter 3.2.14).

3.2.16. *In Vitro* Drug Permeation Modelling

In paper III, intestinal drug permeation was modelled *in vitro* in Hank's balanced salt solution (HBSS, pH 7.4), using cell co-culture monolayers that consisted of the large intestine carcinoma line Caco-2 [281], and a HT29 adenocarcinoma line (ratio 90:10). Transwell cell culture inserts (Corning Inc., U.S.A.) were used. The experiments were carried out in triplicate, at $T = 37$°C. Aliquots of 200 μl were withdrawn from the basolateral compartment at pre-determined time points, and centrifuged. C_{gr} was measured from the supernatant by HPLC (Chapter 3.2.11). The withdrawn aliquots were replaced with fresh buffer to retain a constant volume. The integrity of the cellular barriers was quantitatively and non-destructively determined in before and after the experiments by monitoring the transepithelial electrical resistance (TEER) [389]. A Millicell-Electrical Resistance System (Millipore, U.S.A.) was used for TEER monitoring.

3.2.17. Taguchi Experiment Design

In paper IV, a two-level L12 orthogonal array (OA) was used to design the fractional factorial experiment (FFE) [390]. Ten control factors and a dummy factor were assigned to investigate the optimization of the bi-polar

electroencapsulation process. Microcapsule samples were prepared in triplicate ($n = 3$) in three random-order full cycles of the 12 trial conditions, and subsequently the confirmation experiment. The significance of the factor effects on the measured microcapsule properties and electroencapsulation process yield were analyzed and classified by analysis of variation (ANOVA), and complementary data analysis methods.

4. Results and Discussion on Papers

The most important results of papers I–IV are summarized and discussed briefly in Chapters 4.1–4. The complete experimental arrangements, results, and detailed discussions are presented in the original publications, which can be found reprinted at the end of this book.

4.1. Paper I

A bi-polar parallel nozzle electroencapsulation system of an adjustable geometry was designed and built for the experimental work in paper I. The electroencapsulation process using the setup was described in detail. With the relevant electrospraying liquids as starting materials, the single-step electroencapsulation process was used for production of two types of PSi carrier particles: microcapsules of a liquid glycerol core and a solid Eudragit E 100 shell composition, with TOPSi micro- or nanoparticle dispersions as payloads in the core liquid; as well as solid Eudragit L 100 micromatrix particles with embedded payloads of griseofulvin loaded TOPSi nanoparticle dispersions. The integrity and structure of the produced microcapsules and micromatrix particles were characterized by imaging methods. Limitations and efficiency of the used electroencapsulation setup were discussed, and future improvements were proposed.

For the microcapsule production, extreme values of polymer concentration C_{pol} were used in paper I in order to refine the limits fit for the continuous production of intact and durable microcapsules. It was experimentally verified that various conductivities K could be attained for glycerol in the stable CJM electrospraying region by NaI doping or heating, and a value of K close to the observed maximum was used for the core liquid. For the selected liquids electrosprayed in CJM, the most important parameters for tuning the

encapsulation and collection efficiencies *in situ* were found to be the liquid flow rates Q_i, which affect the core and shell liquid droplet size and charge distributions. Consequently, varying the Q_i also affects the structure, size, and charge distribution of microcapsules.

Spherical, intact and mechanically durable capsules were produced at the higher C_{pol} = 250 mg/ml. On the contrary, at C_{pol} = 50 mg/ml, the capsules were irregularly shaped, faulty and fragile. For both concentrations, the average capsule size was 30 µm. Furthermore, the shell layer was observed by µCT imaging to be on average 3 µm thick for both concentrations. According to the result, the shell layer delicacy when using the lower C_{pol} was likely to be at least partially caused by a lower shell layer density (higher porosity). It was concluded that in the experimented C_{pol} range, mechanically handleable and dosable microcapsules, suitable for the protection of the PSi payload until its release in the gastric conditions, can be produced. The minimum usable C_{pol} was found to reside above 50 mg/ml. In the nanoCT images of Figure 8, the distributions of the TOPSi nanoparticles inside the microcapsules can be partially observed. According to the images, the largest of the electroencapsulated TOPSi particles appear to remain dispersed.

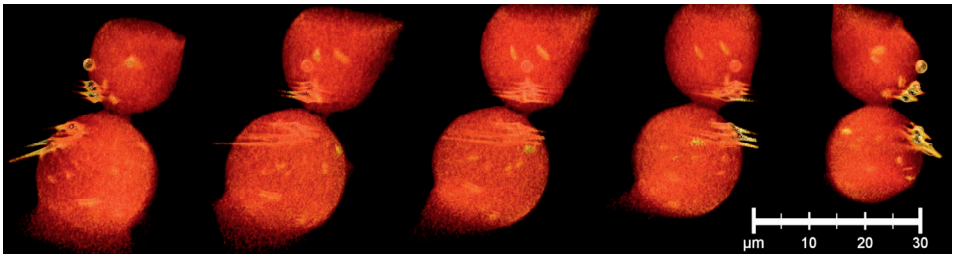

Figure 8. A nanoCT 3D-reconstruction of a pair of core-shell microcapsules produced by bi-polar parallel nozzle electroencapsulation, as viewed from five different angles in 45° increments. The microcapsules consisted of a glycerol core with dispersed TOPSi nanoparticles (C_{TOPSi} = 10.1 mg/ml), inside a solid Eudragit E 100 polymer shell. In the images, the largest of the dispersed TOPSi nanoparticles can be observed clearly as light areas inside the microcapsules. Outside the capsules, some imaging artifacts (strong lines and a bubble) are present. The imaging pixel resolution was 65 nm.

For micromatrix particles, reduction of C_{pol} from the highest continuously electrosprayable concentration was observed to result only in a decreased micromatrix particle size, and no clear minimum usable value for C_{pol} was found. Therefore, a value close to the maximum C_{pol} was used exclusively.

According to microscope imaging, the drug loaded TOPSi nanoparticles were evenly dispersed in the produced solid and durable micromatrix particles. The particles were of an irregular, wrinkled shape, and of some tens of μm in size – ideal for the mechanical handling of the embedded TOPSi nanoparticles as a dry micropowder, and for fast TOPSi release in the small intestine pH conditions, where the matrix material dissolves.

Typical electroencapsulation efficiencies in paper I were observed to be 5–10% for microcapsules, and 10–20% for micromatrix particles. This difference was probably in large part due to the symmetrical nature of the micromatrix particle production, resulting in a natural atomization current balance, and thus efficient neutralization of the colliding droplets. The two types of carriers complemented each other in the usable range of materials, such as the solvents, polymers and PSi surface chemistries. Consequently, PSi particle payload release triggered in either gastric or small intestine pH conditions was concluded to be achievable, depending on the carrier type.

4.2. Paper II

In paper II, a novel polymorphic form of piroxicam was discovered by electrospraying a chloroform solution of piroxicam. The electrosprayed form was characterized extensively, and compared to the corresponding literature data obtained for the previously known piroxicam polymorphs (forms I–III), the unconfirmed α_1-form, and piroxicam monohydrate (Chapter 3.1.1).

XRD analysis was the most important single method in the distinction of the electrosprayed crystal structure from the previously known polymorphs of piroxicam. A unique diffractogram was measured for the electrosprayed piroxicam, which did not match the diffraction patterns of any of the known piroxicam polymorphic forms or the crystal structures of any other compounds found in the available databases. The electrospraying parameters U, Q, and p did not affect the electrosprayed crystal structure. For reduced p, the amorphicity of the sample increased, as previously observed for other drug materials [113]. Furthermore, in a VTXRD analysis the electrosprayed piroxicam was observed to recrystallize completely into form I when heated (Figure 9). Anisotropic thermal expansion of the electrosprayed crystal structure was observed, indicating that the piroxicam molecules were possibly packed in parallel in the electrosprayed crystal lattice, similarly to the packing

in the known piroxicam crystal lattices [381,382,384,386,391]. In storage at ambient conditions, the amorphous phase of the electrosprayed piroxicam sample was concluded to crystallize into forms I and III during the first 43 days. After 127 days, no further significant changes in the sample had occurred, and the electrosprayed crystal structure did not exhibit signs of deterioration. The result was concluded to indicate stability of the electrosprayed crystal structure at ambient conditions.

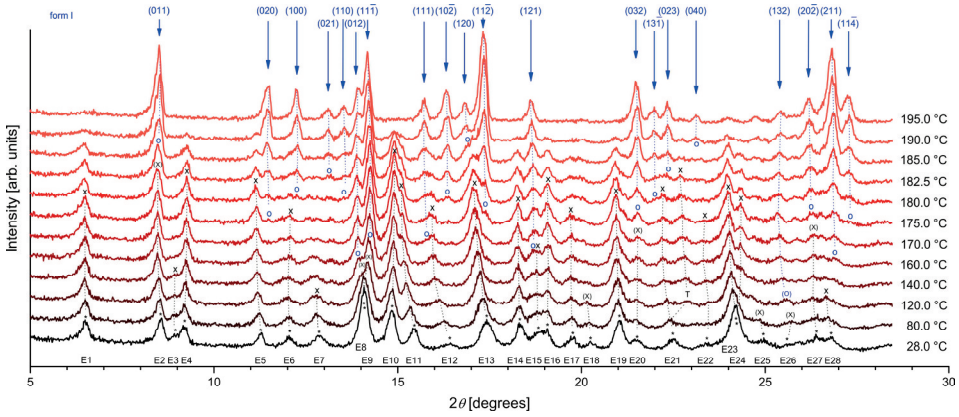

Figure 9. Recrystallization of the electrosprayed piroxicam (peaks denoted E1–E28) into form I (indexed peaks) under heating, as measured by VTXRD.

According to DSC measurements, the first endotherm onset temperature was 179.2 ± 2.3°C for the electrosprayed piroxicam samples. The result does not match reported values of any of the previously known piroxicam polymorphic forms. The onset temperature of recrystallization to form I was measured as 185.5 ± 0.8°C. These temperature results agree well with the diminishment of the electrosprayed form diffraction peaks as well as the emergence of form I diffraction peaks, both processes observed to initiate for the most part at 175.0–182.5°C, as seen in Figure 9. No impurities or degradation products were observed, as confirmed by the HPLC analysis. Raman and FTIR spectra of the electrosprayed form also differed from form I and the amorphous form of piroxicam.

In a previous study, crystallization of piroxicam from a large volume of chloroform solution yielded either form I or form II [392]. However, solvent evaporation from the electrosprayed chloroform droplets, partially taking place in a strong electric field, seem to provide unique circumstances for piroxicam crystallization. A novel polymorphic form of piroxicam was concluded to form

under these conditions. As soon as the results can be confirmed by another group, the obtained new polymorphic form of piroxicam was suggested to be referred to as form IV.

The novel polymorphic form of piroxicam characterized in paper II has already received recognition, but its classification has created some confusion [15,393,394], as another suspected piroxicam polymorphic form has been previously regarded as form IV [395]. However, the characterization of the previously named crystal structure has been limited to only DSC measurement, where a weak melting peak with the onset at 164.1°C was observed [395]. A few months after the publishing of paper II, the discovery of yet another new polymorphic form of piroxicam, designated as form V, has been reported [396].

4.3. Paper III

Two types of gastric-resistant micromatrix particles carrying griseofulvin (Chapter 3.1.1) as a model drug were produced by electroencapsulation, to obtain a controlled release and enhanced dissolution of the drug at small intestine pH conditions, after the particles pass through stomach conditions without exposing the drug material to intestinal metabolism. GE type particles consisted of a disordered griseofulvin solid dispersion in an Eudragit L 100 polymer micromatrix. For GPE type particles, griseofulvin-loaded TOPSi nanoparticles were dispersed to the Eudragit L 100 matrix.

In XRD measurements of fresh GE and GPE particles, as well as samples stored at accelerated conditions (RH 67%, $T = 30$°C) for 6 months, the griseofulvin solid state was observed to be disordered, or "X-ray amorphous": no diffraction peaks were observed. To elaborate, the griseofulvin was dispersed in the polymer matrix in a molecular form, in amorphous clusters, or in a nanocrystalline form, with a crystal size t too small to produce distinguishable diffraction peaks. Using the Scherrer formula and corresponding physical mixtures of crystalline griseofulvin and Eudragit L 100 as reference samples, it was estimated conservatively that if griseofulvin was in nanocrystalline form in the micromatrix particle samples, t could not have been larger than 8 nm [282]. No griseofulvin crystallinity was observed in any of the samples in DSC measurements, either. It has been shown in previous studies that the drug remains in an amorphous form when loaded to the pores of TOPSi nanoparticles [16,276]. It was concluded that the solid state of griseofulvin in

the samples was highly disordered, and stable. For comparison, the spray-drying method only yielded crystalline griseofulvin microparticles in a previous study [315].

Both of the solid dispersion formulations quickly released the griseofulvin payloads *in vitro* at pH 6.8, and were found to drastically improve the griseofulvin dissolution rate, as compared to free, crystalline griseofulvin powder. At pH 1.2, very little griseofulvin leakage was detected from the GE and GPE particles during a period of 120 minutes, whereas the dissolution rate of free griseofulvin remained practically independent of the pH. In Figure 10, a combined dissolution graph with a simulated transition from the stomach to the duodenum is shown for free griseofulvin, as well as the GE and GPE particles. No significant differences were observed in the dissolution behavior of GE and GPE particles.

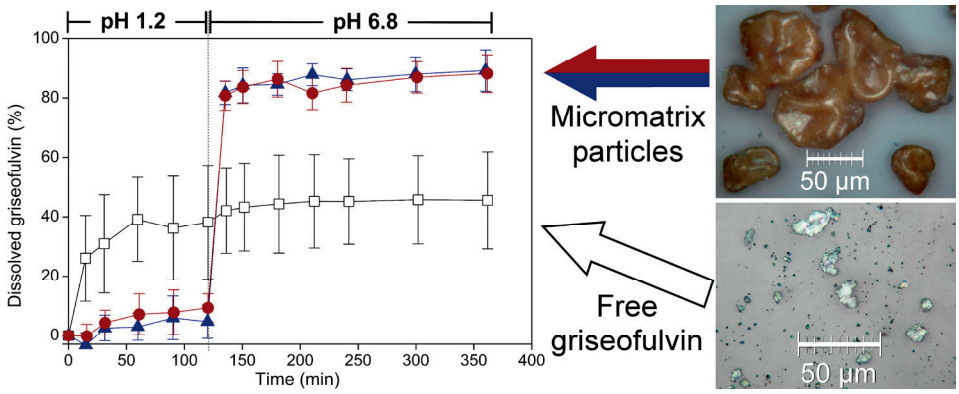

Figure 10. Left: The measured griseofulvin *in vitro* dissolution profiles for free griseofulvin (white rectangles), GE particles (blue triangles), and GPE particles (ref circles), shown with the simulated transition from the stomach to the duodenum pH conditions. Top right: A microscope image of the produced GPE particles. Bottom right: A microscope image of free, crystalline griseofulvin.

Griseofulvin permeation was measured for free griseofulvin as well as the GE and GPE particles *in vitro* across Caco-2/HT29 co-culture cell monolayers, which mimic the human intestinal *in vivo* conditions closely [397]. Significantly different results were obtained for each sample type. The permeation from both of the electroencapsulated particle types was multifold as compared to the free griseofulvin, as expected due to the easily dissoluble form of griseofulvin in the polymer matrices. Perhaps surprisingly, the performance of GPE particles was

far superior to the other sample types, and as high as a ten-fold improvement in the permeation burst during the initial 30 minutes as compared to free griseofulvin was observed. It has been hypothesized that the induced local drug supersaturation in the vicinity of the drug releasing PSi nanoparticles could lead to enhanced drug permeation, when the PSi nanoparticles attach to the mucus layer on the intestine wall. However, this phenomenon is not well understood as of yet [18,352,354,366].

4.4. Paper IV

The influence of ten electrospraying parameters on the properties and yield of core-shell microcapsules produced by electroencapsulation was investigated in a FFE utilizing a two-level L12 OA (*cf.* Chapter 3.2.17). The capsules consisted of a glycerol core with optionally dispersed PSi nanoparticles, and an Eudragit E 100 polymer shell: a composition first introduced in paper I. Based on preliminary experiments, suitable electrospraying parameter values were chosen to ensure a good coverage of the functional electroencapsulation regime, and assigned as factor levels.

To summarize the FFE results, the most significant factors in their chosen ranges for the measured microcapsule structure, yield, and collection efficiency related quantities were found to be T, C_{NaI}, Q_{c}, and Q_{s}. The experiment showed that C_{pol} could be varied within the chosen range to independently adjust the capsule shell thickness to a significant degree. The chosen levels of factors $|U_{\mathrm{s}}|$ and $|U_{\mathrm{c}}|$ did not exhibit significant effects on the electroencapsulation process, except a possible minor influence of $|U_{\mathrm{s}}|$ on the average and variation of the capsule core-shell mass ratio. Finally, the applied ranges of C_{talc}, and C_{PSi}, as well as the nozzle polarity were found to be insignificant for the measured electroencapsulation process quantities in the FFE. However, the presence of a PSi nanoparticle payload ($C_{\mathrm{PSi}} > 0.0$ mg/ml) increased the CJM threshold atomization voltage for the core liquid, which was accounted for by setting the $|U_{\mathrm{c}}|$ factor levels relative to the CJM threshold voltage. Thus, the PSi nanoparticle payload in the used concentrations was not observed to affect the electroencapsulation process significantly, as long as $|U_{\mathrm{c}}|$ was adjusted according to the payload.

T and C_{NaI} were the most influential factors on the overall capsule yield and collection efficiency, with the response and signal to noise ratio (S/N) charts of

the latter quantity shown in Figure 11 as an example. At T = 23°C and C_{NaI} = 0.50 mg/ml (factor levels 1), the electrospraying process was clearly more efficient and consistent, as compared to T = 37°C and C_{NaI} = 1.00 mg/ml (factor levels 2). Notably, at the lower T and C_{NaI} levels, a slightly larger capsule core diameter was observed as well. These effects were for the most part due to the difference in core liquid conductivity K_c between the factor levels for both T and C_{NaI}. The lower K_c at factor levels T = 23°C and C_{NaI} = 0.50 mg/ml resulted in a comparatively large electrosprayed core droplet size (Equations 11, 14, and 17), and thus a decrease in the attainable core droplet charge to mass ratio (Equation 5). Between the chosen factor levels, T was slightly more influential on K_c than C_{NaI}. Moreover, T influenced the electroencapsulation process in other manners as well, as it also significantly affected core liquid viscosity η_c, solvent evaporation rate, and possibly shell liquid conductivity K_s. On the other hand, C_{NaI} influenced K_c in a practically independent manner, and did not significantly affect other core liquid parameters, such as η_c or ρ_c, in the chosen factor range.

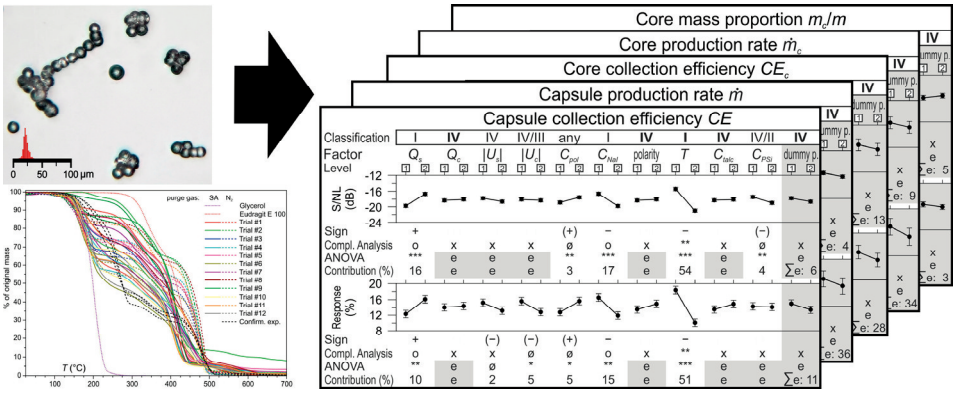

Figure 11. Based on various characterizations of the produced microcapsules, such as size distribution measurements (top left) and composition measurement using TGA (bottom left), response and S/N charts (right) were derived for quantities related to the electroencapsulation process efficiency and microcapsule properties.

During the FFE trials, electroencapsulation efficiency was on average 14 ± 3%. This efficiency improvement from paper I was concluded to be in a large part due to the larger chamber, and careful selection of the trial factor level ranges. Using the optimal combination of factor levels as determined from the FFE trial results, the response and consistency of capsule mass yield,

electroencapsulation efficiency, and core liquid (payload) mass proportion in the capsules were all simultaneously optimized. As a result, an average electroencapsulation efficiency of 48 ± 9% was observed in the FFE confirmation experiments.

In additional experiments, microcapsule samples were produced for a varied Q_c. The core and shell liquid atomization currents I_c and I_s, and electrosprayed volume mean droplet sizes $\overline{d_c}$ and $\overline{d_s}$ were measured. The results showed a good agreement of the I_c and $\overline{d_c}$ scaling laws relative to Q_c (Equations 12 and 13). Consequently, the volume mean core droplet charge $\overline{q_c}$ was observed to scale as $\overline{q_c} \propto Q_c^{0.45\pm0.71}$, whereas the exponent has been previously shown to equal ½ [74]. It was concluded from the results that the optimal factor levels of Q_s, T, and C_{NaI} minimized $|I_c + I_s|$ in the previous FFE experiment. As Q_c was adjusted to 0.60 ml/h from the optimal level of 0.50 mg/ml as determined in the FFE, an increased electroencapsulation efficiency of ~56% was achieved. Additional improvement in efficiency could possibly be gained to an extent by further increasing Q_c. For reference, the highest attainable electroencapsulation efficiency for the used setup was estimated roughly as ~70%, due to limited sample collection dish coverage of the electroencapsulation chamber bottom area. The trend of an increasing core liquid proportion in the capsules was clearly observed, as Q_c was gradually increased. The measured data suggests it is possible that the capsule composition did not change steadily, but in waves or steps as Q_c was varied. Unfortunately, the amount of data points and measurements was inadequate to conclusively determine such details. A possible explanation for an unsteady change of capsule composition as a function of Q_c could be provided by the nature of change in the average number of core and shell droplets that compose a capsule (n_c and n_s): according to the obtained data in the Q_c sweep range, n_c decreased from 6 to 2, while n_s increased from 2 to 3. In a single microcapsule, the number of droplets of each species is always whole. Furthermore, the size and charge distributions of the electrosprayed main droplets of both species were determined to be quite narrow, so it is a possibility that the capsule composition change as a function of Q_c is not perfectly smooth, but instead changes in smoothed, discernible steps for as long as the number of droplets composing a capsule is small. The possible role of highly charged satellite droplets in the formation and neutralization of capsules is important, but was not investigated in the present work.

It was concluded that to achieve an optimal efficiency of the bi-polar parallel nozzle electroencapsulation process to produce core-shell microcapsules, a feasible approach is to keep K_c relatively close to the lower end of the stable core liquid CJM regime. After T has been set, coarse adjustments to K_c should be made by changing C_{NaI}. With Q_s set to the highest continuously operational level, Q_c should be used for final adjustment of the atomization current balance. The atomization voltages $|U_s|$ and $|U_c|$ should be selected near the lower limit of CJM, with a tolerance for fluctuations. In this work, the electroencapsulation process was found to be equally efficient regardless of the presence of a PSi nanoparticle payload dispersed in the core liquid.

5. Conclusions

Using model polymers and pharmaceutical materials, bi-polar parallel nozzle electroencapsulation was shown to be a feasible single-step method for the production of drug carrier particles that potentially improve the oral bioavailability of a carried poorly soluble drug by targeting the drug release, and by enhancing the drug dissolution properties. Two types of carrier particles were produced: Eudragit L 100 polymer micromatrix particles carrying a stabilized, disordered drug solid dispersion or a stabilized dispersion of drug loaded PSi nanoparticles in the solid matrix; and glycerol core-Eudragit E 100 polymer shell microcapsules carrying a dispersed payload of functional drug carrier PSi nanoparticles in the liquid core. The release of the shielded payload was targeted at predetermined (small intestinal or gastric) pH-conditions. The produced enteric micromatrix particles were shown *in vitro* to be gastro-resistant, and to greatly enhance drug dissolution and permeation at the small intestine conditions.

Moreover, it was shown that electrospraying holds great potential as a unique method for the discovery and production of new stable polymorphic forms of pharmaceutical materials. Consequently, the oral bioavailability of certain drug materials could possibly be improved without the need for more complicated formulations to stabilize the amorphous or molecular form.

The bi-polar parallel nozzle electroencapsulation process featured in this work for core-shell microcapsule production is intriguing in its complexity. With a pair of electrosprays producing two species of mutually immiscible and oppositely charged droplets of generally different size and absolute charge distributions into a common encapsulation chamber to form microcapsules at various conditions, numerous variables could potentially affect a certain property of the capsules, or another particular aspect of process. Therefore, empirical studies are invaluable in attempts to understand and control the core-shell microcapsule production process. In comparison, the micromatrix

particle production process was simpler: as identical electrosprays could be used, the process was in part equivalent to an electrospraying process of a double yield. In this work, the necessity of external droplet neutralization was eliminated in exchange for a larger mean particle size by the use of opposite electrospray polarities.

In core-shell microcapsule production, the capsule yield and properties could be controlled quite extensively by adjusting the electroencapsulation parameters, such as the electrospraying liquid compositions and flow rates, as well as the electroencapsulation geometry and conditions. The most significant electroencapsulation parameters were identified and optimized for efficient core liquid utilization and yield. As a result, nearly ideal electroencapsulation efficiency and a high core liquid mass ratio was achieved for the capsules, while retaining a sufficient shell thickness for good durability. Importantly, the presence of a PSi nanoparticle payload in the core liquid did not disrupt the electroencapsulation process, as long as the atomization voltage was adjusted accordingly.

Compared to alternative electroencapsulation geometries, such as the co-axial nozzle electroencapsulation technique, the bi-polar parallel nozzle electroencapsulation is arguably a more complicated process. As an advantage of the parallel nozzle technique, additional neutralization may not be necessary in the production of core-shell microcapsules or micromatrix particles. In addition, the bi-polar parallel nozzle electrospraying technique can be applied for micromixing, the production of microreactors, or building of Janus particles. In the field of pharmacy, the technique could also be used for the production of spherical dual-drug nanoparticles, or for the production of complex micromatrix particles consisting of compounds that together in a single solution could not be electrosprayed due to constituent interactions.

In future research efforts on bi-polar parallel nozzle electroencapsulation, the further mapping of suitable electroencapsulation material combinations is necessary. Perhaps more importantly, the focus should be on the successful implementation of scale-up techniques in order to drastically improve the overall microcapsule or micromatrix particle yield, which in the present work remains unsuitably low for most practical drug delivery applications. The most promising scale-up approaches include various electrospraying nozzle array arrangements, as well as the use of line or surface electrospraying sources instead of point sources.

References

[1] Brayden, D. J. and Medicine, V. Controlled release technologies for drug delivery. *Drug Discov. Today* **8,** 976–978 (2003).

[2] Hörter, D. and Dressman, J. B. Influence of physicochemical properties on dissolution of drugs in the gastrointestinal tract. *Adv. Drug Deliv. Rev.* **46,** 75–87 (2001).

[3] Lipinski, C. A. Drug-like properties and the causes of poor solubility and poor permeability. *J. Pharmacol. Toxicol. Methods* **44,** 235–249 (2000).

[4] Panchagnula, R. and Thomas, N. S. Biopharmaceutics and pharmacokinetics in drug research. *Int. J. Pharm.* **201,** 131–150 (2000).

[5] Savjani, K. T., Gajjar, A. K. and Savjani, J. K. Drug solubility: importance and enhancement techniques. *ISRN Pharm.* **2012,** 195727 (2012).

[6] Yu, L. Amorphous pharmaceutical solids: preparation, characterization and stabilization. *Adv. Drug Deliv. Rev.* **48,** 27–42 (2001).

[7] Leuner, C. and Dressman, J. Improving drug solubility for oral delivery using solid dispersions. *Eur. J. Pharm. Biopharm.* **50,** 47–60 (2000).

[8] Sugihara, M., Takeuchi, S., Sugita, M., Higaki, K., Kataoka, M. and Yamashita, S. Analysis of Intra- and Intersubject Variability in Oral Drug Absorption in Human Bioequivalence Studies of 113 Generic Products. *Mol. Pharm.* **12,** 4405–4413 (2015).

[9] Jaworek, A. and Sobczyk, A. T. Electrospraying route to nanotechnology: An overview. *J. Electrostat.* **66,** 197–219 (2008).

[10] Jaworek, A. Micro- and nanoparticle production by electrospraying. *Powder Technol.* **176,** 18–35 (2007).

[11] Hancock, B. and Parks, M. What is the true solubility advantage for amorphous pharmaceuticals? *Pharm. Res.* **17,** 397–404 (2000).

[12] Xie, J., Jiang, J., Davoodi, P., Srinivasan, M. P. P. and Wang, C. H.

Electrohydrodynamic atomization: A two-decade effort to produce and process micro-/nanoparticulate materials. *Chem. Eng. Sci.* **125,** 32–57 (2015).

[13] Nyström, M., Murtomaa, M. and Salonen, J. Fabrication of amorphous pharmaceutical materials by electrospraying into reduced pressure. *J. Electrostat.* **69,** 351–356 (2011).

[14] Datta, S. and Grant, D. J. W. Crystal structures of drugs: Advances in determination, prediction and engineering. *Nature Reviews Drug Discovery* **3,** 42–57 (2004).

[15] Mehta, P. *et al.* Pharmaceutical and biomaterial engineering via electrohydrodynamic atomization technologies. *Drug Discov. Today* **22,** 157–165 (2017).

[16] Santos, H. A., Salonen, J. and Bimbo, L. M. Porous Silicon for Drug Delivery. in *Encyclopedia of Metalloproteins* (eds. Kretsinger, R. H., Uversky, V. N. & Permyakov, E. A.) 1773–1781 (Springer Science + Business Media, 2013).

[17] Salonen, J. *et al.* Mesoporous silicon microparticles for oral drug delivery: Loading and release of five model drugs. *J. Control. Release* **108,** 362–374 (2005).

[18] Bimbo, L. M., Mäkilä, E., Laaksonen, T., Lehto, V. P., Salonen, J., Hirvonen, J. and Santos, H. A. Drug permeation across intestinal epithelial cells using porous silicon nanoparticles. *Biomaterials* **32,** 2625–2633 (2011).

[19] Moon, P. and Spencer, D. E. *Foundations of Electrodynamics*. (D. Van Nostrand Company, Inc., 1960).

[20] Cross, J. A. *Electrostatics: Principles, Problems and Applications*. (IOP Publishing Ltd., 1987).

[21] Millikan, R. A. On the elementary electrical charge and the avogadro constant. *Phys. Rev.* **2,** 109–143 (1913).

[22] Bonnor, W. B. Negative mass in general relativity. *Gen. Relativ. Gravit.* **21,** 1143–1157 (1989).

[23] Müller, I. and Weiss, W. Gravity in general relativity, attractive and repulsive contributions. *Meccanica* **51,** 2933–2948 (2016).

[24] Gorkavyi, N. and Vasilkov, A. A repulsive force in the einstein theory. *Mon. Not. R. Astron. Soc.* **461,** 2929–2933 (2016).

[25] Bohr, N. On the constitution of atoms and molecules. *Philos. Mag. Ser. 6* **26,** 1–25 (1913).

[26] Pauling, L. The nature of the chemical bond. IV. The energy of single bonds and the relative electronegativity of atoms. *J. Am. Chem. Soc.* **54,** 3570–3582 (1932).

[27] Tully, R. B., Courtois, H., Hoffman, Y. and Pomarède, D. The Laniakea supercluster of galaxies. *Nature* **513,** 71–3 (2014).

[28] Thorne, K. S. *Black Holes and Time Warps – Einstein's Outrageous Legacy*. (W. W. Norton & Company, 1994).

[29] Streetman, B. G. and Banerjee, S. *Solid State Electronic Devices*. (Prentice Hall, Inc., 2000).

[30] Fabish, T. J. and Duke, C. B. Molecular charge states and contact charge exchange in polymers. *J. Appl. Phys.* **48,** 4256–4266 (1977).

[31] Bhattacharya, K. On the dependence of charge density on surface curvature of an isolated conductor. *Phys. Scr.* **91,** 035501 (2016).

[32] Shaw, D. J. *Introduction to Colloid and Surface Chemistry*. (Butterworth-Heinemann, 1992).

[33] Předota, M., Bandura, A. V., Cummings, P. T., Kubicki, J. D., Wesolowski, D. J., Chialvo, A. A. and Machesky, M. L. Electric Double Layer at the Rutile (110) Surface. 1. Structure of Surfaces and Interfacial Water from Molecular Dynamics by Use of ab Initio Potentials. *J. Phys. Chem. B* **108,** 12049–12060 (2004).

[34] Lowell, J. and Rose-Innes, A. C. Contact electrification. *Adv. Phys.* **29,** 947–1023 (1980).

[35] Matsusaka, S. and Masuda, H. Electrostatics of particles. *Adv. Powder Technol.* **14,** 143–166 (2003).

[36] Harper, W. R. The Volta Effect as a Cause of Static Electrification. *Proc. R. Soc. A Math. Phys. Eng. Sci.* **205,** 83–103 (1951).

[37] Castle, G. S., Inculet, I. I., Sines, G. S. and Schein, L. B. Contact Charging Between Metals Revisited. *IEEE Trans. Ind. Appl.* **40,** 1226–1230 (2004).

[38] Bailey, A. G. Charging of Solid and Powders. *J. Electrostat.* **30,** 167–180 (1993).

[39] Baytekin, H. T., Patashinski, A. Z., Branicki, M., Baytekin, B., Soh, S. and Grzybowski, B. A. The Mosaic of Surface Charge in Contact Electrification. *Science (80-.).* **333,** 308–312 (2011).

[40] Duke, C. B., Fabisii, T. J. and Paton, A. Influence of polarization fluctuattons on the electronic structure of molecular solids. **49,** 133–136 (1977).

[41] Lacks, D. J. and Mohan Sankaran, R. Contact electrification of insulating materials. *J. Phys. D. Appl. Phys.* **44,** 453001 (2011).

[42] Lowell, J. Charging of bulk states in semiconductors and insulators in contact with metals. *J. Electrostat.* **8,** 161–169 (1980).

[43] Shaw, P. E. Experiments on Tribo-Electricity. I. The Tribo-Electric Series. *Proc. R. Soc. A Math. Phys. Eng. Sci.* **94,** 16–33 (1917).

[44] Diaz, A. F. and Felix-Navarro, R. M. A semi-quantitative tribo-electric series for polymeric materials: the influence of chemical structure and properties. *J. Electrostat.* **62,** 277–290 (2004).

[45] Park, C. H., Park, J. K., Jeon, H. S. and Chun, B. C. Triboelectric series and charging properties of plastics using the designed vertical-reciprocation charger. *J. Electrostat.* **66,** 578–583 (2008).

[46] Wang, Z. L. Triboelectric Nanogenerators as New Energy Technology for Self-Powered Systems and as Active Mechanical and Chemical Sensors. *ACS Nano* **7,** 9533–9557 (2013).

[47] Murtomaa, M., Mellin, V., Harjunen, P., Lankinen, T., Laine, E. and Lehto, V.-P. Effect of particle morphology on the triboelectrification in dry powder inhalers. *Int. J. Pharm.* **282,** 107–114 (2004).

[48] Nordhage, F. and Bäckström, G. Sliding and rolling electrification of a NaCl-metal system. *J. Electrostat.* **3,** 371–383 (1977).

[49] Faraday, M. XXXII. On static electrical inductive action. *Philos. Mag. Ser. 3* **22,** 200–204 (1843).

[50] Bottomley, J. T. and King, F. A. Experiments with Vacuum Gold-Leaf Electroscopes on the Mechanical Temperature Effects in Rarefied Gases. *Proc. R. Soc. A Math. Phys. Eng. Sci.* **79,** 285–295 (1907).

[51] Scruton, B. and Blott, B. H. A high resolution probe for scanning electrostatic potential profiles across surfaces. *J. Phys. E.* **6,** 472–474 (1973).

[52] Peltonen, J., Murtomaa, M. and Salonen, J. A coaxial induction probe for measuring the charge, size and distance of a passing object. *J. Electrostat.* **77,** 94–100 (2015).

[53] Paschen, F. Ueber die zum Funkenübergang in Luft, Wasserstoff und Kohlensäure bei verschiedenen Drucken erforderliche Potentialdifferenz. *Ann. Phys.* **273,** 69–96 (1889).

[54] Radmilović-Radjenović, M., Radjenović, B., Nikitović, Ž., Matejčik, Š. and Klas, M. The humidity effect on the breakdown voltage characteristics and the transport parameters of air. *Nucl. Instruments*

Methods Phys. Res. Sect. B Beam Interact. with Mater. Atoms **279,** 103–105 (2012).

[55] Fujita, H., Kouno, T., Noguchi, Y. and Ueguri, S. Breakdown voltages of gaseous N2 and air from normal to cryogenic temperatures. *Cryogenics (Guildf).* **18,** 195–200 (1978).

[56] Alisoy, H. Z., Yesil, A., Koseoglu, M. and Unal, I. An approach for unipolar corona discharge in N2/O2 gas mixture by considering townsend conditions. *J. Electrostat.* **69,** 284–290 (2011).

[57] Chang, J. S. J.-S., Lawless, P. A. P. A. and Yamamoto, T. Corona Discharge Processes. *IEEE Trans. Plasma Sci.* **19,** 1152–1166 (1991).

[58] MacGorman, D. R. and Rust, W. D. *The Electrical Nature of Storms*. (Oxford University Press, Inc., 1998).

[59] Wescott, E. M., Sentman, D. D., Heavner, M. J., Hallinan, T. J., Hampton, D. L. and Osborne, D. L. The optical spectrum of aircraft St. Elmo's fire. *Geophys. Res. Lett.* **23,** 3687–3690 (1996).

[60] Kumara, S., Serdyuk, Y. and Gubanski, S. Charging of Polymeric Surfaces by Positive Impulse Corona. *IEEE Trans. Dielectr. Electr. Insul.* **16,** 726–733 (2009).

[61] Dey, A. and Thomas, G. *Electronics Grade Water Preparation*. (Tall Oaks Ventures LLC, 2003).

[62] Bailey, A. G. *Electrostatic Spraying of Liquids*. (Research Studies Press Ltd., 1988).

[63] Cooper, D. W. and Reist, P. C. Neutralizing charged aerosols with radioactive sources. *J. Colloid Interface Sci.* **45,** 17–26 (1973).

[64] Fowler, R. H. and Nordheim, L. Electron Emission in Intense Electric Fields. *Proc. R. Soc. A Math. Phys. Eng. Sci.* **119,** 173–181 (1928).

[65] Cardona, M. *et al. Photoemission in Solids I.* **26,** (Springer Berlin Heidelberg, 1978).

[66] Hirabayashi, A. Evaporation of charged fine droplets. *Int. J. Mass Spectrom. Ion Process.* **175,** 241–245 (1998).

[67] Cheng, Y. and Zhou, O. Electron field emission from carbon nanotubes. *Comptes Rendus Phys.* **4,** 1021–1033 (2003).

[68] Makela, J. M., Washeleski, R. L. and King, L. B. Regenerable Field Emission Cathode for Spacecraft Neutralization. *J. Propuls. Power* **25,** 970–975 (2009).

[69] Grace, J. M. and Marijnissen, J. C. M. A review of liquid atomization by electrical means. *J. Aerosol Sci.* **25,** 1005–1019 (1994).

[70] Cloupeau, M. and Prunet-Foch, B. Electrostatic spraying of liquids: Main functioning modes. *J. Electrostat.* **25,** 165–184 (1990).

[71] Cloupeau, M. and Prunet-Foch, B. Electrostatic spraying of liquids in cone-jet mode. *J. Electrostat.* **22,** 135–159 (1989).

[72] Poncelet, D., Babak, V. G., Neufeld, R. J. and Burgarski, B. Theory of electrostatic dispersion of polymer solutions in the production of microgel beads containing biocatalyst. 213–228 (1999).

[73] Hohman, M. M., Shin, M., Rutledge, G. and Brenner, M. P. Electrospinning and electrically forced jets. II. Applications. *Phys. Fluids* **13,** 2221–2236 (2001).

[74] Gañán-Calvo, A. M., Dávila, J. and Barrero, A. Current and droplet size in the electrospraying of liquids. Scaling laws. *J. Aerosol Sci.* **28,** 249–275 (1997).

[75] Felici, N. J. Recent developments and future trends in electrostatic generation. *Direct Curr.* **4,** 3–12 (1959).

[76] Dumont, Q. and Cole, R. B. Jean-Antoine Nollet: The father of experimental electrospray. *Mass Spectrom. Rev.* **33,** 418–423 (2014).

[77] Zeleny, J. On the conditions of instability of electrified drops, with applications to the electrical discharge from liquid points. *Proceeding Cambridge Philos. Soc.* **18,** 71–83 (1916).

[78] Zeleny, J. Instability of electrified liquid surfaces. *Phys. Rev.* **10,** 1–6 (1917).

[79] Taylor, G. Disintegration of water drops in an electric field. *Proc. R. Soc. London. Ser. A* **280,** 383–397 (1964).

[80] Gañán-Calvo, A. M., Rebollo-Muñoz, N. and Montanero, J. M. The minimum or natural rate of flow and droplet size ejected by Taylor cone-jets: Physical symmetries and scaling laws. *New J. Phys.* **15,** (2013).

[81] Park, H., Kim, K. and Kim, S. Effects of a guard plate on the characteristics of an electrospray in the cone-jet mode. *J. Aerosol Sci.* **35,** 1295–1312 (2004).

[82] Lastow, O. and Balachandran, W. Novel low voltage EHD spray nozzle for atomization of water in the cone jet mode. *J. Electrostat.* **65,** 490–499 (2007).

[83] Nyström, M., Murtomaa, M. and Salonen, J. Fabrication and characterization of drug particles produced by electrospraying into reduced pressure. *J. Electrostat.* **68,** 42–48 (2010).

[84] Reyderman, L. and Stavchansky, S. Electrostatic spraying and its use in

drug delivery — Cholesterol microspheres. *Int. J. Pharm.* **124,** 75–85 (1995).

[85] Ryan, C. N., Smith, K. L. and Stark, J. P. W. The flow rate sensitivity to voltage across four electrospray modes. *Appl. Phys. Lett.* **104,** 084101 (2014).

[86] Salata, O. V. Tools of Nanotechnology: Electrospray. *Curr. Nanosci.* **1,** 25–33 (2005).

[87] Taylor, G. Electrically Driven Jets. *Proc. R. Soc. A Math. Phys. Eng. Sci.* **313,** 453–475 (1969).

[88] Lozano, P., Martínez-Sánchez, M. and Lopez-Urdiales, J. M. Electrospray emission from nonwetting flat dielectric surfaces. *J. Colloid Interface Sci.* **276,** 392–399 (2004).

[89] Bocanegra, R., Galán, D., Márquez, M., Loscertales, I. G. and Barrero, A. Multiple electrosprays emitted from an array of holes. *J. Aerosol Sci.* **36,** 1387–1399 (2005).

[90] Castro, S. and Fernández de la Mora, J. Effect of tip curvature on ionic emissions from Taylor cones of ionic liquids from externally wetted tungsten tips. *J. Appl. Phys.* **105,** 034903 (2009).

[91] Legge, R. S. and Lozano, P. C. Electrospray Propulsion Based on Emitters Microfabricated in Porous Metals. *J. Propuls. Power* **27,** 485–495 (2011).

[92] Vieu, C. *et al.* Gold nanograins deposited from a liquid metal ion source. *Microelectron. Eng.* **35,** 349–352 (1997).

[93] Jaworek, A., Lackowski, M., Krupa, A. and Czech, T. Electrostatic interaction of free EHD jets. *Exp. Fluids* **40,** 568–576 (2006).

[94] Kawakami, K. Miscibility analysis of particulate solid dispersions prepared by electrospray deposition. *Int. J. Pharm.* **433,** 71–78 (2012).

[95] Kourmatzis, A., Allen, J. and Shrimpton, J. S. Electrical and spray characteristics of a multi-orifice charge-injection atomizer for electrically insulating liquids. *Atomization and Sprays* **20,** 269–280 (2010).

[96] Velasquez-Garcia, L. F., Akinwande, A. I. and Martinez-Sanchez, M. A Planar Array of Micro-Fabricated Electrospray Emitters for Thruster Applications. *J. Microelectromechanical Syst.* **15,** 1272–1280 (2006).

[97] Rulison, A. J. and Flagan, R. C. Scale-up of electrospray atomization using linear arrays of Taylor cones. *Rev. Sci. Instrum.* **64,** 683–686 (1993).

[98] Kumar, V., Srivastava, A., Shanbhogue, K. M., Ingersol, S. and Sen, A. K. Electrospray performance of interacting multi-capillary emitters in a linear array. *J. Micromechanics Microengineering* **28,** 035005 (2018).

[99] Regele, J. D., Papac, M. J., Rickard, M. J. A. and Dunn-Rankin, D. Effects of capillary spacing on EHD spraying from an array of cone jets. *J. Aerosol Sci.* **33,** 1471–1479 (2002).

[100] Tang, K., Lin, Y., Matson, D. W., Kim, T. and Smith, R. D. Generation of multiple electrosprays using microfabricated emitter arrays for improved mass spectrometric sensitivity. *Anal. Chem.* **73,** 1658–1663 (2001).

[101] Almekinders, J. C. and Jones, C. Multiple jet electrohydrodynamic spraying and applications. *J. Aerosol Sci.* **30,** 969–971 (1999).

[102] Deng, W., Klemic, J. F., Li, X., Reed, M. A. and Gomez, A. Increase of electrospray throughput using multiplexed microfabricated sources for the scalable generation of monodisperse droplets. *J. Aerosol Sci.* **37,** 696–714 (2006).

[103] Morad, M. R., Rajabi, A., Razavi, M. and Pejman Sereshkeh, S. R. A Very Stable High Throughput Taylor Cone-jet in Electrohydrodynamics. *Sci. Rep.* **6,** 38509 (2016).

[104] Jordahl, J. H., Ramcharan, S., Gregory, J. V. and Lahann, J. Needleless Electrohydrodynamic Cojetting of Bicompartmental Particles and Fibers from an Extended Fluid Interface. *Macromol. Rapid Commun.* **38,** 1600437 (2017).

[105] Balachandran, W. and Bailey, A. G. The influence of electrostatic fields on the centrifugal atomisation of liquids. *J. Electrostat.* **10,** 189–196 (1981).

[106] Balachandran, W. and Bailey, A. G. The Dispersion of Liquids Using Centrifugal and Electrostatic Forces. *IEEE Trans. Ind. Appl.* **IA-20,** 682–686 (1984).

[107] Barrero, A., López-Herrera, J. M., Boucard, A., Loscertales, I. G. and Márquez, M. Steady cone-jet electrosprays in liquid insulator baths. *J. Colloid Interface Sci.* **272,** 104–108 (2004).

[108] Sato, M., Okubo, N., Nakane, T., Sun, B. and Urashima, K. Nozzleless EHD Spraying for Fine Droplet Production in Liquid-in-Liquid System. *IEEE Trans. Ind. Appl.* **46,** 2190–2195 (2010).

[109] Marín, Á. G., Loscertales, I. G. and Barrero, A. Surface tension effects on submerged electrosprays. *Biomicrofluidics* **6,** 044104 (2012).

[110] Moroshkin, P., Leiderer, P., Möller, T. B. and Kono, K. Taylor cone and electrospraying at a free surface of superfluid helium charged from below. *Phys. Rev. E* **95,** 053110 (2017).

[111] Jaworek, A. and Krupa, A. Classification of the modes of EHD spraying. *J. Aerosol Sci.* **30,** 873–893 (1999).

[112] Cloupeau, M. and Prunet-Foch, B. Electrohydrodynamic spraying functioning modes: a critical review. *J. Aerosol Sci.* **25,** 1021–1036 (1994).

[113] Nyström, M., Murtomaa, M., Roine, J., Sandler, N. and Salonen, J. Processing of pharmaceutical materials by electrospraying under reduced pressure. *Drug Dev. Ind. Pharm.* **41,** 116–123 (2015).

[114] Hayati, I., Bailey, A. . and Tadros, T. . Investigations into the mechanisms of electrohydrodynamic spraying of liquids. *J. Colloid Interface Sci.* **117,** 205–221 (1987).

[115] Hayati, I., Bailey, A. I. and Tadros, T. F. Investigations into the mechanisms of electrohydrodynamic spraying of liquids. I. Effect of electric field and the environment on pendant drops and factors affecting the formation of stable jets and atomization. *J. Colloid Interface Sci.* **117,** 205–221 (1987).

[116] Nemes, P., Marginean, I. and Vertes, A. Spraying Mode Effect on Droplet Formation and Ion Chemistry in Electrosprays. *Anal. Chem.* **79,** 3105–3116 (2007).

[117] Zheng, J. *et al.* Jet behaviors and ejection mode recognition of electrohydrodynamic direct-write. *AIP Adv.* **8,** 015122 (2018).

[118] Hartman, R. P. a, Brunner, D. J., Camelot, D. M. a, Marijnissen, J. C. M. and Scarlett, B. Jet Break-Up in Electrohydrodynamic Atomization in the Cone-Jet Mode. *J. Aerosol Sci.* **31,** 65–95 (2000).

[119] Barrero, A. and Loscertales, I. G. Micro- and Nanoparticles via Capillary Flows. *Annu. Rev. Fluid Mech.* **39,** 89–106 (2007).

[120] Ha, N. S., Tran, T. T.-D., Tran, P. H.-L., Park, J.-B. and Lee, B.-J. Dissolution-enhancing mechanism of alkalizers in poloxamer-based solid dispersions and physical mixtures containing poorly water-soluble valsartan. *Chem. Pharm. Bull. (Tokyo).* **59,** 844–50 (2011).

[121] Taflin, D. C., Ward, T. L. and Davis, E. J. Electrified Droplet Fission and the Rayleigh Limit. *Langmuir* **5,** 376–384 (1989).

[122] Doyle, A., Moffett, D. R. and Vonnegut, B. Behavior of evaporating electrically charged droplets. *J. Colloid Sci.* **19,** 136–143 (1964).

[123] Roulleau, M. and Desbois, M. Study of Evaporation and Instability of Charged Water Droplets. *J. Atmos. Sci.* **29,** 565–569 (1972).

[124] Castillo-Orozco, E., Kar, A. and Kumar, R. Electrospray mode transition of microdroplets with semiconductor nanoparticle suspension. *Sci. Rep.* **7,** 5144 (2017).

[125] Zhang, J., Li, X., Zhang, D. and Xiu, Z. Theoretical and experimental investigations on the size of alginate microspheres prepared by dropping and spraying. *J. Microencapsul.* **24,** 303–22 (2007).

[126] Lee, M. W., An, S., Kim, N. Y., Seo, J. H., Huh, J.-Y., Kim, H. Y. and Yoon, S. S. Effects of pulsing frequency on characteristics of electrohydrodynamic inkjet using micro-Al and nano-Ag particles. *Exp. Therm. Fluid Sci.* **46,** 103–110 (2013).

[127] Lee, M. W., Kang, D. K., Kim, N. Y., Kim, H. Y., James, S. C. and Yoon, S. S. A study of ejection modes for pulsed-DC electrohydrodynamic inkjet printing. *J. Aerosol Sci.* **46,** 1–6 (2012).

[128] Xie, J. and Wang, C.-H. Electrospray in the dripping mode for cell microencapsulation. *J. Colloid Interface Sci.* **312,** 247–255 (2007).

[129] J, W. and L, Z. Creation of alginate capsules by electrostatic dispersion method in dripping mode. *Inz. Chem. i Proces.* **25,** 1813–1818 (2004).

[130] Ku, B. K. and Kim, S. S. Electrohydrodynamic spraying characteristics of glycerol solutions in vacuum. *J. Electrostat.* **57,** 109–128 (2003).

[131] Li, J. On the stability of electrohydrodynamic spraying in the cone-jet mode. *J. Electrostat.* **65,** 251–255 (2007).

[132] Hartman, R. P. A., Brunner, D. J., Camelot, D. M. A., Marijnissen, J. C. M. and Scarlett, B. Electrohydrodynamic Atomization in the Cone-Jet Mode Physical Modeling of the Liquid Cone and Jet. *J. Aerosol Sci.* **30,** 823–849 (1999).

[133] Hartman, R. P. A., Borra, J. P., Brunner, D. J., Marijnissen, J. C. M. and Scarlett, B. The evolution of electrohydrodynamic sprays produced in the cone-jet mode, a physical model. *J. Electrostat.* **47,** 143–170 (1999).

[134] Chakraborty, S., Liao, I.-C., Adler, A. and Leong, K. W. Electrohydrodynamics: A facile technique to fabricate drug delivery systems. *Adv. Drug Deliv. Rev.* **61,** 1043–1054 (2009).

[135] Nguyen, D. N., Clasen, C. and Van den Mooter, G. Pharmaceutical Applications of Electrospraying. *J. Pharm. Sci.* **105,** 2601–2620 (2016).

[136] Chen, D.-R., Pui, D. Y. H. and Kaufman, S. L. Electrospraying of conducting liquids for monodisperse aerosol generation in the 4 nm to

1.8 µm diameter range. *J. Aerosol Sci.* **26,** 963–977 (1995).

[137] Sofokleous, P., Stride, E., Bonfield, W. and Edirisinghe, M. Design, construction and performance of a portable handheld electrohydrodynamic multi-needle spray gun for biomedical applications. *Mater. Sci. Eng. C* **33,** 213–223 (2013).

[138] Meesters, G. M. H., Vercoulen, P. H. W., Marijnissen, J. C. M. and Scarlett, B. Generation of micron-sized droplets from the Taylor cone. *J. Aerosol Sci.* **23,** 37–49 (1992).

[139] Jayasinghe, S. N., Dorey, R. A., Edirisinghe, M. J. and Luklinska, Z. B. Preparation of lead zirconate titanate nano-powder by electrohydrodynamic atomization. *Appl. Phys. A* **80,** 723–725 (2005).

[140] Gomez, A. and Tang, K. Charge and fission of droplets in electrostatic sprays. *Phys. Fluids* **6,** 404–414 (1994).

[141] Gañán-Calvo, A. M., Lasheras, J. C., Dávila, J. and Barrero, A. The electrostatic spray emitted from an electrified conical meniscus. *J. Aerosol Sci.* **25,** 1121–1142 (1994).

[142] Wilhelm, O., Mädler, L. and Pratsinis, S. E. Electrospray evaporation and deposition. *J. Aerosol Sci.* **34,** 815–836 (2003).

[143] Lenggoro, I. W., Okuyama, K., De La Mora, J. F. and Tohge, N. Preparation of ZnS nanoparticles by electrospray pyrolysis. *J. Aerosol Sci.* **31,** 121–136 (2000).

[144] Gan, Y., Zhang, X., Li, H., Tong, Y., Shi, Y. and Yan, Y. The atomization current and droplet size of ethanol in two different small-scale electro-spraying systems. *J. Electrostat.* **87,** 228–235 (2017).

[145] De La Mora, J. F. and Loscertales, I. G. The current emitted by highly conducting Taylor cones. *J. Fluid Mech.* **260,** 155 (1994).

[146] Smith, D. P. H. The Electrohydrodynamic Atomization of Liquids. *IEEE Trans. Ind. Appl.* **IA-22,** 527–535 (1986).

[147] Stachewicz, U., Dijksman, J. F., Yurteri, C. U. and Marijnissen, J. C. M. Volume of liquid deposited per single event electrospraying controlled by nozzle front surface modification. *Microfluid. Nanofluidics* **9,** 635–644 (2010).

[148] Yao, J., Kuang Lim, L., Xie, J., Hua, J. and Wang, C.-H. Characterization of electrospraying process for polymeric particle fabrication. *J. Aerosol Sci.* **39,** 987–1002 (2008).

[149] Fernandez De La Mora, J., Navascues, J., Fernandez, F. and Rosell-Llompart, J. Generation of submicron monodisperse aerosols in

electrosprays. *J. Aerosol Sci.* **21,** S673–S676 (1990).

[150] Hong, Y., Li, Y., Yin, Y., Li, D. and Zou, G. Electrohydrodynamic atomization of quasi-monodisperse drug-loaded spherical/wrinkled microparticles. *J. Aerosol Sci.* **39,** 525–536 (2008).

[151] Jain, A. K., Sood, V., Bora, M., Vasita, R. and Katti, D. S. Electrosprayed inulin microparticles for microbiota triggered targeting of colon. *Carbohydr. Polym.* **112,** 225–234 (2014).

[152] Arya, N., Chakraborty, S., Dube, N. and Katti, D. S. Electrospraying: a facile technique for synthesis of chitosan-based micro/nanospheres for drug delivery applications. *J. Biomed. Mater. Res. B. Appl. Biomater.* **88,** 17–31 (2009).

[153] Bock, N., Dargaville, T. R. and Woodruff, M. A. Controlling microencapsulation and release of micronized proteins using poly(ethylene glycol) and electrospraying. *Eur. J. Pharm. Biopharm.* **87,** 366–377 (2014).

[154] Zamani, M., Prabhakaran, M. P., Ramakrishna, S. and Press, D. Advances in drug delivery via electrospun and electrosprayed nanomaterials. *Int. J. Nanomedicine* **8,** 2997–3017 (2013).

[155] Park, J.-U. *et al.* High-resolution electrohydrodynamic jet printing. *Nat. Mater.* **6,** 782–9 (2007).

[156] Yu, M., Ahn, K. H. and Lee, S. J. Design optimization of ink in electrohydrodynamic jet printing: Effect of viscoelasticity on the formation of Taylor cone jet. *Mater. Des.* **89,** 109–115 (2016).

[157] Hines, R. L. Electrostatic Atomization and Spray Painting. *J. Appl. Phys.* **37,** 2730 (1966).

[158] Barletta, M. and Gisario, A. Electrostatic spray painting of carbon fibre-reinforced epoxy composites. *Prog. Org. Coatings* **64,** 339–349 (2009).

[159] Law, S. E. Agricultural electrostatic spray application: a review of significant research and development during the 20th century. *J. Electrostat.* **51,** 25–42 (2001).

[160] Law, S. E. and Scherm, H. Electrostatic application of a plant-disease biocontrol agent for prevention of fungal infection through the stigmatic surfaces of blueberry flowers. *J. Electrostat.* **63,** 399–408 (2005).

[161] Khan, S., Doh, Y. H., Khan, A., Rahman, A., Choi, K. H. and Kim, D. S. Direct patterning and electrospray deposition through EHD for fabrication of printed thin film transistors. *Curr. Appl. Phys.* **11,** S271–

S279 (2011).

[162] Jaworek, A. Electrospray droplet sources for thin film deposition. *J. Mater. Sci.* **42,** 266–297 (2006).

[163] Chen, C.-A., Acquaviva, P., Chun, J.-H. and Ando, T. Effects of droplet thermal state on deposit microstructure in spray forming. *Scr. Mater.* **34,** 689–696 (1996).

[164] Diagne, E. H. A. and Lumbreras, M. Elaboration and characterization of tin oxide–lanthanum oxide mixed layers prepared by the electrostatic spray pyrolysis technique. *Sensors Actuators B Chem.* **78,** 98–105 (2001).

[165] Nguyen, T. and Djurado, E. Deposition and characterization of nanocrystalline tetragonal zirconia films using electrostatic spray deposition. *Solid State Ionics* **138,** 191–197 (2001).

[166] Fenn, J. B., Mann, M., Meng, C. K., Wong, S. F. and Whitehouse, C. M. Electrospray ionization for mass spectrometry of large biomolecules. *Science* **246,** 64–71 (1989).

[167] Henning, T., Huhn, K., Isberner, L. W. and Klar, P. J. Miniaturized Electrospray Thrusters. *IEEE Trans. Plasma Sci.* **46,** 214–218 (2018).

[168] Jaworek, A. and Krupa, A. Generation and characteristics of the precession mode of ehd spraying. *J. Aerosol Sci.* **27,** 75–82 (1996).

[169] Jaworek, A. and Krupa, A. Forms of the multijet mode of electrohydrodynamic spraying. *J. Aerosol Sci.* **27,** 979–986 (1996).

[170] Lüttgens, U., Dülcks, T. and Röllgen, F. W. Field induced disintegration of glycerol solutions under vacuum and atmospheric pressure conditions studied by optical microscopy and mass spectrometry. *Surf. Sci.* **266,** 197–203 (1992).

[171] Tang, K. and Gomez, A. Generation of Monodisperse Water Droplets from Electrosprays in a Corona-Assisted Cone-Jet Mode. *J. Colloid Interface Sci.* **175,** 326–332 (1995).

[172] Rayleigh, Lord. XX. On the equilibrium of liquid conducting masses charged with electricity. *London, Edinburgh, Dublin Philos. Mag. J. Sci.* **14,** 184–186 (1882).

[173] Abbas, M. A. and Latham, J. The instability of evaporating charged drops. *J. Fluid Mech.* **30,** 663 (1967).

[174] Hendricks, C. D. Charged droplet experiments. *J. Colloid Sci.* **17,** 249–259 (1962).

[175] Lide, D. R. *CRC Handbook of Chemistry and Physics*. (CRC Press, 1992).

[176] Elghazaly, H. M. A. and Castle, G. S. P. Analysis of the Multisibling

Instability of Charged Liquid Drops. *IEEE Trans. Ind. Appl.* **IA-23,** 108–113 (1987).

[177] Reist, P. C. *Introduction to Aerosol Science*. (MacMillan, 1984).

[178] Yarin, A. L., Koombhongse, S. and Reneker, D. H. Taylor cone and jetting from liquid droplets in electrospinning of nanofibers. *J. Appl. Phys.* **90,** 4836–4846 (2001).

[179] José, C. H.-S. and Arias-Zugasti, M. Analysis of the space charge singularity near the Taylor cone apex via simplified Eulerian model for electrospray beams in vacuum. *J. Aerosol Sci.* **118,** 82–99 (2018).

[180] Marginean, I., Parvin, L., Heffernan, L. and Vertes, A. Flexing the electrified meniscus: The birth of a jet in electrosprays. *Anal. Chem.* **76,** 4202–4207 (2004).

[181] Smallwood, I. M. *Handbook of Organic Solvent Properties*. (Arnold, 1996).

[182] Gan, Y., Zhang, X., Li, H., Tong, Y., Zhang, Y., Shi, Y. and Yang, Z. Effect of a ring electrode on the cone-jet characteristics of ethanol in small-scale electro-spraying combustors. *J. Aerosol Sci.* **98,** 15–29 (2016).

[183] Gañán-Calvo, A. M. and Montanero, J. M. Revision of capillary cone-jet physics: Electrospray and flow focusing. *Phys. Rev. E - Stat. Nonlinear, Soft Matter Phys.* **79,** 066305 (2009).

[184] Gañán-Calvo, A. M. The surface charge in electrospraying: Its nature and its universal scaling laws. *J. Aerosol Sci.* **30,** 863–872 (1999).

[185] Burayev, T. K. and Vereshchagin, I. P. Physical processes during electrostatic atomization of liquids. *Fluid Mech. - Sov. Res.; (United States)*

[186] Tang, K. and Gomez, A. Generation by electrospray of monodisperse water droplets for targeted drug delivery by inhalation. *J. Aerosol Sci.* **25,** 1237–1249 (1994).

[187] Singh, A., Van Hamme, J. D. and Ward, O. P. Surfactants in microbiology and biotechnology: Part 2. Application aspects. *Biotechnol. Adv.* **25,** 99–121 (2007).

[188] Zeleny, J. On the conditions of instability of electrified drops, with applications to the electrical discharge from liquid points. in *Proceedings of the Cambridge Philosophical Society* **18,** (1915).

[189] Aykas, D. P. and Barringer, S. The Effect of Temperature, Lecithin Content and Voltage on Droplets/cm2 during Electrostatic Spraying of

Technol. **42,** 75–85 (2008).

[219] Ding, L., Lee, T. and Wang, C.-H. Fabrication of monodispersed Taxol-loaded particles using electrohydrodynamic atomization. *J. Control. Release* **102,** 395–413 (2005).

[220] Fu, H., Patel, A. C., Holtzman, M. J. and Chen, D.-R. A New Electrospray Aerosol Generator with High Particle Transmission Efficiency. *Aerosol Sci. Technol.* **45,** 1176–1183 (2011).

[221] Liu, Q. and Chen, D.-R. An electrospray aerosol generator with X-ray photoionizer for particle charge reduction. *J. Aerosol Sci.* **76,** 148–162 (2014).

[222] Ohsawa, A. Efficient charge neutralization with an ac corona ionizer. *J. Electrostat.* **65,** 598–606 (2007).

[223] Nakaso, K., Han, B., Ahn, K. H., Choi, M. and Okuyama, K. Synthesis of non-agglomerated nanoparticles by an electrospray assisted chemical vapor deposition (ES-CVD) method. *J. Aerosol Sci.* **34,** 869–881 (2003).

[224] Modesto-Lopez, L. B., Kettleson, E. M. and Biswas, P. Soft X-ray charger (SXC) system for use with electrospray for mobility measurement of bioaerosols. *J. Electrostat.* **69,** 357–364 (2011).

[225] Borra, J.-P., Camelot, D., Marijnissen, J. C. M. and Scarlett, B. A new production process of powders with defined properties by electrohydrodynamic atomization of liquids and post-production electrical mixing. *J. Electrostat.* **40–41,** 633–638 (1997).

[226] Mishra, M. K. *Handbook of Encapsulation and Controlled Release*. (CRC Press, 2015). doi:10.1201/b19038

[227] Bocanegra, R., Gaonkar, A. G., Barrero, A., Loscertales, I. G., Pechack, D. and Marquez, M. Production of Cocoa Butter Microcapsules Using an Electrospray Process. *J. Food Sci.* **70,** e492–e497 (2005).

[228] Ravanfar, R., Comunian, T. A. and Abbaspourrad, A. Thermoresponsive, water-dispersible microcapsules with a lipid-polysaccharide shell to protect heat-sensitive colorants. *Food Hydrocoll.* **81,** 419–428 (2018).

[229] Senatore, D., Laven, J., Van Benthem, R. A. T. M., La Camera, D. and De With, G. Microencapsulation of epoxidized linseed oil liquid cross-linker in Poly(N -vinyl-pyrrolidone): Optimization by a design-of-experiments approach. *Ind. Eng. Chem. Res.* **49,** 3642–3653 (2010).

[230] Wen, Y., Gallego, M. R., Nielsen, L. F., Jorgensen, L., Møller, E. H. and Nielsen, H. M. Design and characterization of core-shell mPEG-PLGA

composite microparticles for development of cell-scaffold constructs. *Eur. J. Pharm. Biopharm.* **85,** 87–98 (2013).

[231] Herrero, E., Valle, E. and Galan, M. Development of a new technology for the production of microcapsules based in atomization processes. *Chem. Eng. J.* **117,** 137–142 (2006).

[232] Langer, G. and Yamate, G. Encapsulation of liquid and solid aerosol particles to form dry powders. *J. Colloid Interface Sci.* **29,** 450–455 (1969).

[233] Jafari, S. M., He, Y. and Bhandari, B. Role of Powder Particle Size on the Encapsulation Efficiency of Oils during Spray Drying. *Dry. Technol.* **25,** 1081–1089 (2007).

[234] Theil, F., Milsmann, J., Anantharaman, S. and van Lishaut, H. Manufacturing Amorphous Solid Dispersions with a Tailored Amount of Crystallized API for Biopharmaceutical Testing. *Mol. Pharm.* **15,** 1870–1877 (2018).

[235] Fakes, M. G. *et al.* Enhancement of oral bioavailability of an HIV-attachment inhibitor by nanosizing and amorphous formulation approaches. *Int. J. Pharm.* **370,** 167–74 (2009).

[236] Jaworek, A. Electrostatic micro- and nanoencapsulation and electroemulsification: A brief review. *J. Microencapsul.* **25,** 443–468 (2008).

[237] Enayati, M., Chang, M.-W., Bragman, F., Edirisinghe, M. and Stride, E. Electrohydrodynamic preparation of particles, capsules and bubbles for biomedical engineering applications. *Colloids Surfaces A Physicochem. Eng. Asp.* **382,** 154–164 (2011).

[238] Gao, Y., Zhao, D., Chang, M. W., Ahmad, Z. and Li, J. S. Optimising the shell thickness-to-radius ratio for the fabrication of oil-encapsulated polymeric microspheres. *Chem. Eng. J.* **284,** 963–971 (2016).

[239] Reyes, Y., Peruzzo, P. J., Fernández, M., Paulis, M. and Leiza, J. R. Encapsulation of Clay within Polymer Particles in a High-Solids Content Aqueous Dispersion. *Langmuir* **29,** 9849–9856 (2013).

[240] Smeets, A., Clasen, C. and Van den Mooter, G. Electrospraying of polymer solutions: Study of formulation and process parameters. *Eur. J. Pharm. Biopharm.* **119,** 114–124 (2017).

[241] Sato, M., Kato, S. and Saito, M. Production of oil/water type uniformly sized droplets using a convergent AC electric field. *IEEE Trans. Ind. Appl.* **32,** 138–145 (1996).

[242] Xie, J., Ng, W. J., Lee, L. Y. and Wang, C.-H. Encapsulation of protein drugs in biodegradable microparticles by co-axial electrospray. *J. Colloid Interface Sci.* **317,** 469–476 (2008).

[243] Loscertales, I. G., Barrero, A., Guerrero, I., Cortijo, R., Marquez, M. and Gañán-Calvo, A. M. Micro/nano encapsulation via electrified coaxial liquid jets. *Science (80-.).* **295,** 1695–1698 (2002).

[244] Wu, Y., MacKay, J. A., R. McDaniel, J., Chilkoti, A. and Clark, R. L. Fabrication of Elastin-Like Polypeptide Nanoparticles for Drug Delivery by Electrospraying. *Biomacromolecules* **10,** 19–24 (2009).

[245] Pérez-Masiá, R., López-Nicolás, R., Periago, M. J., Ros, G., Lagaron, J. M. and López-Rubio, A. Encapsulation of folic acid in food hydrocolloids through nanospray drying and electrospraying for nutraceutical applications. *Food Chem.* **168,** 124–33 (2015).

[246] Gomez-Estaca, J., Balaguer, M. P., Gavara, R. and Hernandez-Munoz, P. Formation of zein nanoparticles by electrohydrodynamic atomization: Effect of the main processing variables and suitability for encapsulating the food coloring and active ingredient curcumin. *Food Hydrocoll.* **28,** 82–91 (2012).

[247] Nelson, G. Application of microencapsulation in textiles. *Int. J. Pharm.* **242,** 55–62 (2002).

[248] Zhang, L., Huang, J., Si, T. and Xu, R. X. Coaxial electrospray of microparticles and nanoparticles for biomedical applications. *Expert Rev. Med. Devices* **9,** 595–612 (2012).

[249] Hirech, K., Payan, S., Carnelle, G., Brujes, L. and Legrand, J. Microencapsulation of an insecticide by interfacial polymerisation. *Powder Technol.* **130,** 324–330 (2003).

[250] Xie, J., Lim, L. K., Phua, Y., Hua, J. and Wang, C.-H. Electrohydrodynamic atomization for biodegradable polymeric particle production. *J. Colloid Interface Sci.* **302,** 103–112 (2006).

[251] Xu, Y. and Hanna, M. A. Electrosprayed bovine serum albumin-loaded tripolyphosphate cross-linked chitosan capsules: Synthesis and characterization. *J. Microencapsul.* **24,** 143–151 (2007).

[252] Bohr, A., Kristensen, J., Stride, E., Dyas, M. and Edirisinghe, M. Preparation of microspheres containing low solubility drug compound by electrohydrodynamic spraying. *Int. J. Pharm.* **412,** 59–67 (2011).

[253] Bohr, A. *et al.* Pharmaceutical microparticle engineering with electrospraying: the role of mixed solvent systems in particle formation

and characteristics. *J. Mater. Sci. Mater. Med.* **26,** 61 (2015).

[254] Schachter, D. M., Xiong, J. and Tirol, G. C. Solid state NMR perspective of drug-polymer solid solutions: A model system based on poly(ethylene oxide). *Int. J. Pharm.* **281,** 89–101 (2004).

[255] Ricarte, R. G., Lodge, T. P. and Hillmyer, M. a. Detection of Pharmaceutical Drug Crystallites in Solid Dispersions by Transmission Electron Microscopy. *Mol. Pharm.* **12,** 983–990 (2015).

[256] Jahangiri, A., Barzegar-Jalali, M., Javadzadeh, Y., Hamishehkar, H. and Adibkia, K. Physicochemical characterization of atorvastatin calcium/ezetimibe amorphous nano-solid dispersions prepared by electrospraying method. *Artif. Cells, Nanomedicine, Biotechnol.* **45,** 1138–1145 (2017).

[257] Sasaki, E., Kurayama, F., Ida, J., Matsuyama, T. and Yamamoto, H. Preparation of microcapsules by electrostatic atomization. *J. Electrostat.* **66,** 312–318 (2008).

[258] Borra, J. P., Camelot, D., Chou, K. L., Kooyman, P. J., Marijnissen, J. C. M. and Scarlett, B. Bipolar coagulation for powder production: Micro-mixing inside droplets. *J. Aerosol Sci.* **30,** 945–958 (1999).

[259] Fu, H., Liu, Q. and Chen, D. R. Performance study of a twin-head electrospray system. *J. Aerosol Sci.* **52,** 33–44 (2012).

[260] Mou, F., Chen, C., Guan, J., Chen, D.-R. and Jing, H. Oppositely charged twin-head electrospray: a general strategy for building Janus particles with controlled structures. *Nanoscale* **5,** 2055 (2013).

[261] Walther, A. and Müller, A. H. E. Janus particles. *Soft Matter* **4,** 663 (2008).

[262] Farook, U., Zhang, H. B., Edirisinghe, M. J., Stride, E. and Saffari, N. Preparation of microbubble suspensions by co-axial electrohydrodynamic atomization. *Med. Eng. Phys.* **29,** 749–754 (2007).

[263] Hwang, Y. K., Jeong, U. and Cho, E. C. Production of uniform-sized polymer core-shell microcapsules by coaxial electrospraying. *Langmuir* **24,** 2446–2451 (2008).

[264] Mei, F. and Chen, D.-R. Investigation of compound jet electrospray: Particle encapsulation. *Phys. Fluids* **19,** 103303 (2007).

[265] Chen, X., Jia, L., Yin, X., Cheng, J. and Lu, J. Spraying modes in coaxial jet electrospray with outer driving liquid. *Phys. Fluids* **17,** 032101 (2005).

[266] Li, F. and Yin, X.-Y. X.-Z. Temporal linear instability analysis of an electrified coaxial jet with inner driving liquid inside a coaxial electrode.

J. Electrostat. **64,** 690–698 (2006).

[267] Kim, W. and Kim, S. S. Multishell Encapsulation Using a Triple Coaxial Electrospray System. *Anal. Chem.* **82,** 4644–4647 (2010).

[268] Labbaf, S., Deb, S., Cama, G., Stride, E. and Edirisinghe, M. Preparation of multicompartment sub-micron particles using a triple-needle electrohydrodynamic device. *J. Colloid Interface Sci.* **409,** 245–254 (2013).

[269] Labbaf, S., Ghanbar, H., Stride, E. and Edirisinghe, M. Preparation of Multilayered Polymeric Structures Using a Novel Four-Needle Coaxial Electrohydrodynamic Device. *Macromol. Rapid Commun.* **35,** 618–623 (2014).

[270] Nangrejo, M., Ahmad, Z. and Edirisinghe, M. Generation of ceramic–ceramic layered composite microstructures using electrohydrodynamic co-axial flow. *Ceram. Int.* **36,** 1217–1223 (2010).

[271] Roh, K. H., Martin, D. C. and Lahann, J. Triphasic nanocolloids. *J. Am. Chem. Soc.* **128,** 6796–6797 (2006).

[272] Hwang, S., Roh, K.-H., Lim, D. W., Wang, G., Uher, C. and Lahann, J. Anisotropic hybrid particles based on electrohydrodynamic co-jetting of nanoparticle suspensions. *Phys. Chem. Chem. Phys.* **12,** 11894 (2010).

[273] Lahann, J. Recent Progress in Nano-biotechnology: Compartmentalized Micro- and Nanoparticles via Electrohydrodynamic Co-jetting. *Small* **7,** 1149–1156 (2011).

[274] George, M. C. and Braun, P. V. Multicompartmental Materials by Electrohydrodynamic Cojetting. *Angew. Chemie Int. Ed.* **48,** 8606–8609 (2009).

[275] Davis, S. S. and Illum, L. Drug delivery systems for challenging molecules. *Int. J. Pharm.* **176,** 1–8 (1998).

[276] Salonen, J., Kaukonen, A. M., Hirvonen, J. and Lehto, V.-P. Mesoporous silicon in drug delivery applications. *J. Pharm. Sci.* **97,** 632–653 (2008).

[277] Masaoka, Y., Tanaka, Y., Kataoka, M., Sakuma, S. and Yamashita, S. Site of drug absorption after oral administration: assessment of membrane permeability and luminal concentration of drugs in each segment of gastrointestinal tract. *Eur. J. Pharm. Sci.* **29,** 240–250 (2006).

[278] Kimura, T. and Higaki, K. Gastrointestinal Transit and Drug Absorption. *Biol. Pharm. Bull.* **25,** 149–164 (2002).

[279] Yoshioka, S. and Stella, V. J. Chemical Stability of Drug Substances. in *Stability of Drugs and Dosage Forms* 3–137 (Kluwer Academic

Publishers, 2002). doi:10.1007/0-306-46829-8_2

[280] Barich, D. H., Zell, M. T. and Munson, E. J. Physicochemical Properties, Formulation, and Drug Delivery. in *Drug Delivery: Principles and Applications: Second Edition* 35–48 (John Wiley & Sons, Inc, 2016). doi:10.1002/9781118833322.ch3

[281] Shokhin, I. E., Kulinich, Y. I., Ramenskaya, G. V. and Kukes, V. G. Essential biopharmaceutical properties of drugs at the gastrointestinal absorption stage (review). *Pharmaceutical Chemistry Journal* **45,** 415–418 (2011).

[282] Cullity, B. D. *Elements of X-Ray Diffraction*. (Addison-Wesley, 1978).

[283] Zallen, R., Mahan, G. D. and Douglas, R. W. Amorphous solid. *Encyclopædia Britannica* (2016). Available at: https://www.britannica.com/science/amorphous-solid. (Accessed: 20th July 2018)

[284] Zallen, R. *The Physics of Amorphous Solids*. (John Wiley & Sons, Inc., 1983).

[285] Buerger, M. J. *Elementary Crystallography*. (John Wiley & Sons, Inc., 1956).

[286] Warren, B. E. *X-Ray Diffraction*. (Dover Publications, Inc., 1990).

[287] Kile, D. E., Eberl, D. D., Hoch, A. R. and Reddy, M. M. An assessment of calcite crystal growth mechanisms based on crystal size distributions. *Geochim. Cosmochim. Acta* **64,** 2937–2950 (2000).

[288] Cheng, H.-M. Metre-size single-crystal graphene becomes a reality. *Sci. Bull.* **62,** 1039–1040 (2017).

[289] Vippagunta, S. R., Brittain, H. G. and Grant, D. J. W. Crystalline solids. *Adv. Drug Deliv. Rev.* **48,** 3–26 (2001).

[290] Sheth, A. R., Bates, S., Muller, F. X. and Grant, D. J. W. Polymorphism in Piroxicam. *Cryst. Growth Des.* **4,** (2004).

[291] Kuhnert-Brandstätter, M. Polymorphie bei Arzneistoffen. *Pharm. Unserer Zeit* **4,** 131–137 (1975).

[292] Hirsch, A. The era of carbon allotropes. *Nat. Mater.* **9,** 868–871 (2010).

[293] Castro Neto, A. H., Guinea, F., Peres, N. M. R., Novoselov, K. S. and Geim, A. K. The electronic properties of graphene. *Rev. Mod. Phys.* **81,** 109–162 (2009).

[294] Okude, A. and Takiyama, H. Selective recrystallization of metastable polymorph of melt acetaminophen by using tempering operation. *J. Ind. Eng. Chem.* **31,** 263–268 (2015).

[295] Marotta, A., Saiello, S., Branda, F. and Buri, A. Activation energy for the crystallization of glass from DDTA curves. *J. Mater. Sci.* **17,** 105–108 (1982).

[296] Huang, C., Ruan, S., Cai, T. and Yu, L. Fast Surface Diffusion and Crystallization of Amorphous Griseofulvin. *J. Phys. Chem. B* **121,** 9463–9468 (2017).

[297] Yu, L., Reutzel, S. M. and Stephenson, G. A. Physical characterization of polymorphic drugs: an integrated characterization strategy. *Pharm. Sci. Technolo. Today* **1,** 118–127 (1998).

[298] Hancock, B. C. and Zografi, G. Characteristics and significance of the amorphous state in pharmaceutical systems. *J. Pharm. Sci.* **86,** 1–12 (1997).

[299] Gray, T. J., Detwiler, D. P., Rase, D. E., Lawrence, W. G., West, R. R. and Jennings, T. J. *The Defect Solid State.* (Interscience Publishers, Inc., 1957).

[300] Janssens, S. and Van den Mooter, G. Review: physical chemistry of solid dispersions. *J. Pharm. Pharmacol.* **61,** 1571–1586 (2009).

[301] Pikal, M. J., Lukes, A. L., Lang, J. E. and Gaines, K. Quantitative Crystallinity Determinations for β-Lactam Antibiotics by Solution Calorimetry: Correlations with Stability. *J. Pharm. Sci.* **67,** 767–773 (1978).

[302] Mäkilä, E. *et al.* Confinement Effects on Drugs in Thermally Hydrocarbonized Porous Silicon. *Langmuir* (2014).

[303] Adam, G. and Gibbs, J. H. On the Temperature Dependence of Cooperative Relaxation Properties in Glass-Forming Liquids. *J. Chem. Phys.* **43,** 139–146 (1965).

[304] Izumi, F. and Kodama, H. Crystallization and relative stabilities of Polymorphs of Niobium(V) Oxide under hydrothermal conditions. *ZAAC - J. Inorg. Gen. Chem.* **440,** 155–167 (1978).

[305] Yoshioka, S. and Aso, Y. Correlations between molecular mobility and chemical stability during storage of amorphous pharmaceuticals. *Journal of Pharmaceutical Sciences* **96,** 960–981 (2007).

[306] Li, H., Kiang, Y.-H. and Jona, J. Multiple approaches to pharmaceutical polymorphism investigation—A case study. *Eur. J. Pharm. Sci.* **38,** 426–432 (2009).

[307] Mosharraf, M. and Nyström, C. Apparent solubility of drugs in partially crystalline systems. *Drug Dev. Ind. Pharm.* **29,** 603–622 (2003).

[308] Brouwers, J., Brewster, M. E. and Augustijns, P. Supersaturating drug delivery systems: the answer to solubility-limited oral bioavailability? *J. Pharm. Sci.* **98,** 2549–72 (2009).

[309] Verma, S. and Rudraraju, V. S. Wetting Kinetics: an Alternative Approach Towards Understanding the Enhanced Dissolution Rate for Amorphous Solid Dispersion of a Poorly Soluble Drug. *AAPS PharmSciTech* **16,** 1079–1090 (2015).

[310] Noyes, A. A. and Whitney, W. R. The rate of solution of solid substances in their own solutions. *J. Am. Chem. Soc.* **19,** 930–934 (1897).

[311] Nernst, W. Theorie der Reaktionsgeschwindigkeit in heterogenen Systemen. *Zeitschrift für Phys. Chemie* **47U,** 52–55 (1904).

[312] Liversidge, G. G. and Cundy, K. C. Particle size reduction for improvement of oral bioavailability of hydrophobic drugs: I. Absolute oral bioavailability of nanocrystalline danazol in beagle dogs. *Int. J. Pharm.* **125,** 91–97 (1995).

[313] Gupta, M. K., Vanwert, A. and Bogner, R. H. Formation of physically stable amorphous drugs by milling with Neusilin. *J. Pharm. Sci.* **92,** 536–551 (2003).

[314] Kumar, S., Shen, J. and Burgess, D. J. Nano-amorphous spray dried powder to improve oral bioavailability of itraconazole. *J. Control. Release* **192,** 95–102 (2014).

[315] Wong, S. M., Kellaway, I. W. and Murdan, S. Enhancement of the dissolution rate and oral absorption of a poorly water soluble drug by formation of surfactant-containing microparticles. *Int. J. Pharm.* **317,** 61–68 (2006).

[316] Pareta, R., Brindley, A., Edirisinghe, M. J., Jayasinghe, S. N. and Luklinska, Z. B. Electrohydrodynamic atomization of protein (bovine serum albumin). *J. Mater. Sci. Mater. Med.* **16,** 919–925 (2005).

[317] Xu, Y., Skotak, M. and Hanna, M. Electrospray encapsulation of water-soluble protein with polylactide. I. Effects of formulations and process on morphology and particle size. *J. Microencapsul.* **23,** 69–78 (2006).

[318] Gibaldi, M. and Feldman, S. Establishment of sink conditions in dissolution rate determinations. Theoretical considerations and application to nondisintegrating dosage forms. *J. Pharm. Sci.* **56,** 1238–1242 (1967).

[319] Galia, E., Nicolaides, E., Hörter, D., Löbenberg, R., Reppas, C. and Dressman, J. B. Evaluation of various dissolution media for predicting

in vivo performance of class I and II drugs. *Pharm. Res.* **15,** 698–705 (1998).

[320] Levitt, D. G. Quantitation of small intestinal permeability during normal human drug absorption. *BMC Pharmacol. Toxicol.* **14,** 34 (2013).

[321] Lee, C.-H., Bhatt, P. P. and Chien, Y. W. Effect of excipient on drug release and permeation from silicone-based barrier devices. *J. Control. Release* **43,** 283–290 (1997).

[322] Dahlgren, D. *et al.* The effects of three absorption-modifying critical excipients on the in vivo intestinal absorption of six model compounds in rats and dogs. *Int. J. Pharm.* **547,** 158–168 (2018).

[323] Gavhane, Y. N. and Yadav, A. V. Loss of orally administered drugs in GI tract. *Saudi Pharm. J.* **20,** 331–344 (2012).

[324] Yamahara, H. and Lee, V. H. L. Drug metabolism in the oral cavity. *Adv. Drug Deliv. Rev.* **12,** 25–39 (1993).

[325] Thummel, K. E., Kunze, K. L. and Shen, D. D. Enzyme-catalyzed processes of first-pass hepatic and intestinal drug extraction. *Advanced Drug Delivery Reviews* **27,** 99–127 (1997).

[326] Sekiguchi, K. and Obi, N. Studies on Absorption of Eutectic Mixture. I. A Comparison of the Behavior of Eutectic Mixture of Sulfathiazole and that of Ordinary Sulfathiazole in Man. *Chem. Pharm. Bull. (Tokyo).* **9,** 866–872 (1961).

[327] Yadav, A. V, Shete, A. S., Dabke, A. P., Kulkarni, P. V and Sakhare, S. S. Co-crystals: a novel approach to modify physicochemical properties of active pharmaceutical ingredients. *Indian J. Pharm. Sci.* **71,** 359–70 (2009).

[328] Aitipamula, S. *et al.* Polymorphs, salts, and cocrystals: What's in a name? *Crystal Growth and Design* **12,** 2147–2152 (2012).

[329] Anglin, E. J., Cheng, L., Freeman, W. R. and Sailor, M. J. Porous silicon in drug delivery devices and materials. *Adv. Drug Deliv. Rev.* **60,** 1266–77 (2008).

[330] Santos, H. A., Peltonen, L., Limnell, T. and Hirvonen, J. Mesoporous Materials and Nanocrystals for Enhancing the Dissolution Behavior of Poorly Water-soluble Drugs. *Curr. Pharm. Biotechnol.* **14,** 926–938 (2013).

[331] Chiou, W. L. and Riegelman, S. Oral absorption of griseofulvin in dogs: Increased absorption viasolid dispersion in polyethylene glycol 6000. *J.*

Pharm. Sci. **59,** 937–942 (1970).

[332] Gupta, P., Kakumanu, V. K. and Bansal, A. K. Stability and Solubility of Celecoxib-PVP Amorphous Dispersions: A Molecular Perspective. *Pharm. Res.* **21,** 1762–1769 (2004).

[333] Shuai, S., Yue, S., Huang, Q., Wang, W., Yang, J., Lan, K. and Ye, L. Preparation, characterization and in vitro/vivo evaluation of tectorigenin solid dispersion with improved dissolution and bioavailability. *Eur. J. Drug Metab. Pharmacokinet.* **41,** 413–422 (2016).

[334] Paidi, S. K., Jena, S. K., Ahuja, B. K., Devasari, N. and Suresh, S. Preparation, in-vitro and in-vivo evaluation of spray-dried ternary solid dispersion of biopharmaceutics classification system class II model drug. *J. Pharm. Pharmacol.* **67,** 616–629 (2015).

[335] He, X., Pei, L., Tong, H. H. Y. and Zheng, Y. Comparison of Spray Freeze Drying and the Solvent Evaporation Method for Preparing Solid Dispersions of Baicalein with Pluronic F68 to Improve Dissolution and Oral Bioavailability. *AAPS PharmSciTech* **12,** 104–113 (2011).

[336] Lo, W. Y. and Law, S. L. Dissolution Behavior of Griseofulvin Solid Dispersions Using Polyethylene Glycol, Talc, and Their Combination as Dispersion Carriers. *Drug Dev. Ind. Pharm.* **22,** 231–236 (1996).

[337] Watanabe, T., Hasegawa, S., Wakiyama, N., Usui, F., Kusai, A., Isobe, T. and Senna, M. Solid state radical recombination and charge transfer across the boundary between indomethacin and silica under mechanical stress. *J. Solid State Chem.* **164,** 27–33 (2002).

[338] Matsumoto, T. and Zografi, G. Physical Properties of Solid Molecular Dispersions of Indomethacin with Poly(vinylpyrrolidone) and Poly(vinylpyrrolidone-co-vinyl-acetate) in Relation to Indomethacin Crystallization. *Pharm. Res.* **16,** 1722–1728 (1999).

[339] Hikima, T., Hanaya, M. and Oguni, M. Microscopic observation of a peculiar crystallization in the glass transition region and β-process as potentially controlling the growth rate in triphenylethylene. *J. Mol. Struct.* **479,** 245–250 (1999).

[340] Bhattacharya, S. and Suryanarayanan, R. Local mobility in amorphous pharmaceuticals - Characterization and implications on stability. *Journal of Pharmaceutical Sciences* **98,** 2935–2953 (2009).

[341] Alhijjaj, M., Yassin, S., Reading, M., Zeitler, J. A., Belton, P. and Qi, S. Characterization of Heterogeneity and Spatial Distribution of Phases in Complex Solid Dispersions by Thermal Analysis by Structural

Characterization and X-ray Micro Computed Tomography. *Pharm. Res.* **34,** 971–989 (2017).

[342] Han, H.-K., Lee, B.-J. and Lee, H.-K. Enhanced dissolution and bioavailability of biochanin A via the preparation of solid dispersion: In vitro and in vivo evaluation. *Int. J. Pharm.* **415,** 89–94 (2011).

[343] Craig, D. Q. . The mechanisms of drug release from solid dispersions in water-soluble polymers. *International Journal of Pharmaceutics* **231,** 131–144 (2002).

[344] Baghel, S., Cathcart, H. and O'Reilly, N. J. Polymeric Amorphous Solid Dispersions: A Review of Amorphization, Crystallization, Stabilization, Solid-State Characterization, and Aqueous Solubilization of Biopharmaceutical Classification System Class II Drugs. *J. Pharm. Sci.* **105,** 2527–2544 (2016).

[345] Bley, H., Fussnegger, B. and Bodmeier, R. Characterization and stability of solid dispersions based on PEG/polymer blends. *Int. J. Pharm.* **390,** 165–173 (2010).

[346] Fong, S. Y. K., Ibisogly, A. and Bauer-Brandl, A. Solubility enhancement of BCS Class II drug by solid phospholipid dispersions: Spray drying versus freeze-drying. *Int. J. Pharm.* **496,** 382–391 (2015).

[347] Ozeki, T., Yuasa, H. and Kanaya, Y. Application of the solid dispersion method to the controlled release of medicine. IX. Difference in the release of flurbiprofen from solid dispersions with poly(ethylene oxide) and hydroxypropylcellulose and the interaction between medicine and polymers. *Int. J. Pharm.* **155,** 209–217 (1997).

[348] Parfitt, J. R. and Driman, D. K. Pathological effects of drugs on the gastrointestinal tract: a review. *Hum. Pathol.* **38,** 527–36 (2007).

[349] LaFountaine, J. S., Prasad, L. K., Miller, D. A., McGinity, J. W. and Williams, R. O. Mucoadhesive amorphous solid dispersions for sustained release of poorly water soluble drugs. *Eur. J. Pharm. Biopharm.* **113,** 157–167 (2017).

[350] Riikonen, J. *et al.* Systematic in vitro and in vivo study on porous silicon to improve the oral bioavailability of celecoxib. *Biomaterials* **52,** 44–55 (2015).

[351] Riikonen, J., Mäkilä, E., Salonen, J. and Lehto, V.-P. Determination of the physical state of drug molecules in mesoporous silicon with different surface chemistries. *Langmuir* **25,** 6137–42 (2009).

[352] Kaukonen, A. M. *et al.* Enhanced in vitro permeation of furosemide

loaded into thermally carbonized mesoporous silicon (TCPSi) microparticles. *Eur. J. Pharm. Biopharm.* **66,** 348–356 (2007).

[353] Canham, L. T. Bioactive silicon structure fabrication through nanoetching techniques. *Adv. Mater.* **7,** 1033–1037 (1995).

[354] Shrestha, N. *et al.* Chitosan-modified porous silicon microparticles for enhanced permeability of insulin across intestinal cell monolayers. *Biomaterials* **35,** 7172–9 (2014).

[355] Shahbazi, M.-A. *et al.* Surface chemistry dependent immunostimulative potential of porous silicon nanoplatforms. *Biomaterials* **35,** 9224–35 (2014).

[356] Kaasalainen, M. *et al.* Effect of isotonic solutions and peptide adsorption on zeta potential of porous silicon nanoparticle drug delivery formulations. *Int. J. Pharm.* **431,** 230–6 (2012).

[357] Bimbo, L. M., Sarparanta, M., Santos, A., Airaksinen, A. J. and Ma, E. Biocompatibility of Thermally Hydrocarbonized Porous Silicon Nanoparticles and their Biodistribution in Rats. **4,** 3023–3032 (2010).

[358] Wang, F., Hui, H., Barnes, T. J., Barnett, C. and Prestidge, C. A. Oxidized mesoporous silicon microparticles for improved oral delivery of poorly soluble drugs. *Mol. Pharm.* **7,** 227–236 (2010).

[359] Wang, C. F., Mäkilä, E. M., Kaasalainen, M. H., Hagström, M. V., Salonen, J. J., Hirvonen, J. T. and Santos, H. A. Dual-drug delivery by porous silicon nanoparticles for improved cellular uptake, sustained release, and combination therapy. *Acta Biomater.* **16,** 206–214 (2015).

[360] Kovalainen, M. *et al.* Development of porous silicon nanocarriers for parenteral peptide delivery. *Mol. Pharm.* **10,** 353–9 (2013).

[361] McInnes, S. J. P. *et al.* Combination of iCVD and porous silicon for the development of a controlled drug delivery system. *ACS Appl. Mater. Interfaces* **4,** 3566–3574 (2012).

[362] Liu, D. *et al.* Microfluidic templated mesoporous silicon-solid lipid microcomposites for sustained drug delivery. *ACS Appl. Mater. Interfaces* **5,** 12127–12134 (2013).

[363] Horcajada, P., Rámila, A., Pérez-Pariente, J. and Vallet-Regí, M. Influence of pore size of MCM-41 matrices on drug delivery rate. *Microporous Mesoporous Mater.* **68,** 105–109 (2004).

[364] Foraker, A. B., Walczak, R. J., Cohen, M. H., Boiarski, T. A., Grove, C. F. and Swaan, P. W. Microfabricated Porous Silicon Particles Enhance Paracellular Delivery of Insulin Across Intestinal Caco-2 Cell

Monolayers. *Pharm. Res.* **20,** 110–116 (2003).

[365] Mäkilä, E. *et al.* Influence of Surface Chemistry on Ibuprofen Adsorption and Confinement in Mesoporous Silicon Microparticles. *Langmuir* **32,** 13020–13029 (2016).

[366] Araújo, F. *et al.* The impact of nanoparticles on the mucosal translocation and transport of GLP-1 across the intestinal epithelium. *Biomaterials* **35,** 9199–207 (2014).

[367] Parsegian, V. A. *Van der Waals Forces: A Handbook for Biologists, Chemists, Engineers, and Physicists*. (Cambridge University Press, 2006).

[368] Peng, Z., Doroodchi, E. and Evans, G. DEM simulation of aggregation of suspended nanoparticles. *Powder Technol.* **204,** 91–102 (2010).

[369] Livage, J. and Roux, D. Specific features of nanoscale growth. in *Nanomaterials and Nanochemistry* (eds. Bréchignac, C., Houdy, P. & Lahmani, M.) 383–394 (Springer, 2007).

[370] Salonen, J., Lehto, V.-P., Björkqvist, M., Laine, E. and Niinistö, L. Chemical stability studies of thermally-carbonized porous silicon. *MRS Proc.* **638,** F14.19.1 (2000).

[371] Williams, D. I., Marten, R. H. and Sarkany, I. Oral Treatment of Ringworm with Griseofulvin. *Lancet* 1212–13 (1958).

[372] Amidon, G. L., Lennernäs, H., Shah, V. P. and Crison, J. R. A Theoretical Basis for a Biopharmaceutic Drug Classification: The Correlation of in Vitro Drug Product Dissolution and in Vivo Bioavailability. *Pharm. Res.* **12,** 413–420 (1995).

[373] Zecevic, D. E., Meier, R., Daniels, R. and Wagner, K.-G. Site specific solubility improvement using solid dispersions of HPMC-AS/HPC SSL - Mixtures. *Eur. J. Pharm. Biopharm.* **87,** 264–70 (2014).

[374] Alvarez-Lorenzo, C., Gonzalez-Lopez, J., Fernandez-Tarrio, M., Sandez-Macho, I. and Concheiro, A. Tetronic micellization, gelation and drug solubilization: Influence of pH and ionic strength. *Eur. J. Pharm. Biopharm.* **66,** 244–52 (2007).

[375] Knoblauch, J. and Zimmermann, I. Thermochemical analysis of the dissolution process of Griseofulvin. *Eur. J. Pharm. Biopharm.* **67,** 743–751 (2007).

[376] Bhakay, A., Azad, M., Bilgili, E. and Dave, R. Redispersible fast dissolving nanocomposite microparticles of poorly water-soluble drugs. *Int. J. Pharm.* **461,** 367–79 (2014).

[377] Ahmed, H., Buckton, G. and Rawlins, D. a. Crystallisation of partially

amorphous griseofulvin in water vapour: determination of kinetic parameters using isothermal heat conduction microcalorimetry. *Int. J. Pharm.* **167,** 139–145 (1998).

[378] Zhou, D., Zhang, G. G. Z., Law, D., Grant, D. J. W. and Schmitt, E. A. Thermodynamics, Molecular Mobility and Crystallization Kinetics of Amorphous Griseofulvin. *Mol. Pharm.* **5,** 927–936 (2008).

[379] Mirza, S., Miroshnyk, I., Habib, M. J., Brausch, J. F. and Hussain, M. D. Enhanced Dissolution and Oral Bioavailability of Piroxicam Formulations: Modulating Effect of Phospholipids. *Pharmaceutics* **2,** 339–350 (2010).

[380] Bordner, J., Hammen, P. D. and Whipple, E. B. Deuterium isotope effects on carbon-13 NMR shifts and the tautomeric equilibrium in N-substituted pyridyl derivatives of piroxicam. *J. Am. Chem. Soc.* **111,** 6572–6578 (1989).

[381] Vrečer, F. *et al.* Characterization of piroxicam crystal modifications. *Int. J. Pharm.* **256,** 3–15 (2003).

[382] Kojic-Prodic, B. and Ruzic-Toros, Z. Structure of the Anti-inflammatory Drug 4-Hydroxy-2-methyl-N-2-pyridyl-2H-λ^6,2-benzothiazine-3-carboxamide 1,1-Dioxide (Piroxicam). *Acta Cryst* **B38,** 2948–2951 (1982).

[383] Reck, G. and Laban, G. Prediction and establishment of a new crystalline piroxicam modification. *Pharmazie* **45,** 257–9 (1990).

[384] Naelapää, K., Streek, J. Van De, Rantanen, J. and Bond, A. D. Complementing High-Throughput X-ray Powder Diffraction Data with Quantum – Chemical Calculations : Application to Piroxicam Form III. *J. Pharm. Sci.* **101,** 4214–4219 (2012).

[385] Reck, G., Dietz, G., Laban, G., Günther, W., Bannier, G. and Höhne, E. X-ray studies on piroxicam modifications. *Pharmazie* **43,** 477–81 (1988).

[386] Bordner, J., Richards, J. A., Weeks, P., Whipple, E. B. and IUCr. Piroxicam monohydrate: a zwitterionic form, C15H13N3O4S.H2O. *Acta Crystallogr. Sect. C Cryst. Struct. Commun.* **40,** 989–990 (1984).

[387] Salonen, J., Björkqvist, M., Laine, E. and Niinistö, L. Stabilization of porous silicon surface by thermal decomposition of acetylene. *Appl. Surf. Sci.* **225,** 389–394 (2004).

[388] Lehto, V. P., Vähä-Heikkilä, K., Paski, J. and Salonen, J. Use of thermoanalytical methods in quantification of drug load in mesoporous

silicon microparticles. *J. Therm. Anal. Calorim.* **80,** 393–397 (2005).

[389] Srinivasan, B., Kolli, A. R., Esch, M. B., Abaci, H. E., Shuler, M. L. and Hickman, J. J. TEER measurement techniques for in vitro barrier model systems. *J. Lab. Autom.* **20,** 107–26 (2015).

[390] Ross, P. J. *Taguchi Techniques for Quality Engineering.* (McGraw-Hill, 1996).

[391] Redenti, E., Zanol, M., Ventura, P., Fronza, G., Comotti, A., Taddei, P. and Bertoluzza, A. Raman and solid state 13C-NMR investigation of the structure of the 1 : 1 amorphous piroxicam : beta-cyclodextrin inclusion compound. *Biospectroscopy* **5,** 243–251 (1999).

[392] Taddei, P., Torreggiani, A. and Simoni, R. Influence of environment on piroxicam polymorphism: Vibrational spectroscopic study. *Biopolymers* **62,** 68–78 (2001).

[393] Higashi, K., Ueda, K. and Moribe, K. Recent progress of structural study of polymorphic pharmaceutical drugs. *Adv. Drug Deliv. Rev.* **117,** 71–85 (2017).

[394] Morozov, Y. N. *et al.* Cryochemical modification of drugs: Nanosized form III piroxicam and its physical and chemical properties. *Moscow Univ. Chem. Bull.* **71,** 307–314 (2016).

[395] Vrečer, F., Srčič, S. and Šmid-Korbar, J. Investigation of piroxicam polymorphism. *Int. J. Pharm.* **68,** 35–41 (1991).

[396] Lavrič, Z., Pirnat, J., Lužnik, J., Puc, U., Trontelj, Z. and Srčič, S. 14N Nuclear Quadrupole Resonance Study of Piroxicam: Confirmation of New Polymorphic Form V. *J. Pharm. Sci.* **104,** 1909–1918 (2015).

[397] Antunes, F., Andrade, F., Araújo, F., Ferreira, D. and Sarmento, B. Establishment of a triple co-culture in vitro cell models to study intestinal absorption of peptide drugs. *Eur. J. Pharm. Biopharm.* **83,** 427–35 (2013).